Copyright

by

Taylor Bryan Harvey

2014

The Dissertation Committee for Taylor Bryan Harvey Certifies that this is the approved version of the following dissertation:

Sintering of Cu(In,Ga)Se_2 Nanocrystal Films for Photovoltaics

Committee:

Brian A. Korgel, Supervisor

Christopher J. Ellison

Arumugam Manthiram

C. Buddie Mullins

David A. Vanden Bout

Sintering of $Cu(In,Ga)Se_2$ Nanocrystal Films for Photovoltaics

by

Taylor Bryan Harvey, B.S.

Dissertation

Presented to the Faculty of the Graduate School of

The University of Texas at Austin

in Partial Fulfillment

of the Requirements

for the Degree of

Doctor of Philosophy

The University of Texas at Austin

December 2014

Dedication

For Kristi

Who Made this Adventure Possible

Acknowledgements

Sometime in the spring of 2009, I decided to come back to graduate school. It had always been one of those things I wanted to do "someday." But after four years working in industry, I wanted to make a larger impact. I really wanted to work on a problem that could help bring energy to non-powered regions of the world. It has been an amazing, and often completely unexpected experience. I cannot truly express my thanks for those who have helped me these past years. But here is my best attempt to do so.

First, I would like to thank my advisor, Dr. Brian Korgel. He is passionate about the ability of science to create a better world and always tackles the big problems. I am grateful for him allowing me to come along for the ride and be involved in solving problems that really matter. Brian has given me freedom to explore and so many unique opportunities.

I am very grateful to the other members of the Korgel group, both current and past. Jackson Stolle and I started working on the PV project at the same time, and I am very thankful for his hard work, ideas, fellowship and patience. It has been an honor to work with him. Vahid Akhavan helped me so much during my early graduate years and I am thankful for his continued mentorship and friendship. Matt Panthani, Brian Goodfellow, Vince Holmberg, Colin Hessel, and Chet Steinhagen were wonderful research mentors. Early conversations with all of them gave me great ideas and helped tremendously. I am grateful to an early friendship with Aaron Chockla that has led to a current business partnership. Doug Pernik and Jiang Du comprised the rest of the PV group for most of my time and I am thankful for their help and support. And I look forward to great advances from Vikas Reddy and Cherrelle Thomas. My friends and

frequent lunch companions Tim Bogart and Jon Peck have always improved the day and broadened my horizons, culinary and otherwise. Yixuan Yu, Xiaotang Lu, Chris Bosoy, Adrien Guillaussier, Julian Villareal, Emily Adkins, Philip Liu, and Dorothy Silbaugh were wonderful colleagues and friends. I wish great things for them all in the future.

My time in graduate school has also brought me into contact with researchers around the world. I am grateful for the many visiting scholars and undergraduates I had opportunities to work with. It was great to teach and learn from them. The hard work of Isao Mori and Franco Bonafe was particularly fruitful and I am grateful for the chance to work with them. Dr. Lydia Wong accepted me into her group for not one, but two summer stays in Singapore, an experience that has changed my life forever. Thank you to her, John C. W. Ho, Zhang Tianliang, and Hsu ZhengHua for an amazing experience.

Starting with a wild experience in the NSF Icorps program, Heath Naquin has been an invaluable mentor and friend. I appreciate his gentle (and sometimes less than gentle) suggestions, advice, and guidance.

Thank you to Dr. Damon Smith, Mark Andrews, Dr. Dwight Romanovicz, and Dr. Vince Lynch for their assistance with the depositional and characterization equipment that made my work possible. Additionally, the chemical engineering staff has been so helpful. Special thanks to Eddie Ibarra for always getting my just-barely-before-5-pm-on-Friday emergency purchases in.

I would also like to thank my committee for their time and insight: Dr. Buddie Mullins, Dr. Christopher Ellison, Dr. Arumugam Manthiram, and Dr. David Vanden Bout.

Thank you to both old and new friends. There were many conversations that kept my spirits high and helped me redirect my efforts. Thank you especially to Ryan Barlow, Ryan Gotchy Mullen, and Joe Frost for every wandering conversation.

Finally and most importantly, thank you to my family. Your continued love and support make me who I am. My brother and sisters have always been there for me. Thank you to Alan and Mae for always supporting me and my family, even when we end up far away. Mom and Dad, I could never truly express how grateful I am for everything you have done for me and for who you are. James, Matthias, Hannah, and Hyrum- you make my life so much more than it would be otherwise. Thank you for every hug and kiss you give your grumpy dad when he gets home from the lab. And my beautiful and amazing Kristi, thank you for supporting me and all my crazy ideas. You truly made this adventure possible.

Sintering of $Cu(In,Ga)Se_2$ Nanocrystal Films for Photovoltaics

Taylor Bryan Harvey, Ph.D.

The University of Texas at Austin, 2014

Supervisor: Brian A. Korgel

Low cost solar cells are needed to increase availability and reliability of electricity throughout the world. Spray deposition of $Cu(In,Ga)Se_2$ (CIGS) nanocrystal inks is a promising route to low cost photovoltaics(PVs). CIGS nanocrystal inks have been used to fabricate solar cells with 3.1% power conversion efficiency (PCE) without any heat treatment, but are limited by poor charge transport. Sintering the nanocrystals into a polycrystalline film improves charge transport and device performance. Two sintering methods are investigated here: selenization and photonic curing.

The nanocrystal films can be sintered by annealing the films in a Se environment, also known as selenization. The selenized device morphology and efficiency is influenced by the starting nanocrystal composition. A Se/Carbon layer deriving from the organic ligand decreases device efficiency, but is eliminated by annealing the nanocrystal films in Ar before the selenization treatment. In addition to eliminating the Se/Carbon layer, the pre-selenization anneal drives Na from the soda-lime glass substrate into the film and improves grain growth. Devices with efficiencies above 7.0% are fabricated using a multi-step deposition and sintering process. To simplify device fabrication, a single-step, scalable deposition is demonstrated using fully automated, ultrasonic spray coating. The ultrasonic spray deposition is highly sensitive to the nanocrystal ink organic content, and optimization of the nanocrystal synthesis wash procedure leads to highly

uniform, reflective nanocrystal films. Devices fabricated from these films achieve 6.6% efficiency after selenization.

The use of rapid pulses of broadband light, or photonic curing, is an alternative sintering method that is compatible with roll-to-roll fabrication and does not use high temperature processing. A wide range of pulse energy is used to treat nanocrystal films after spray deposition on three different back contact materials. Nanocrystal dewetting and agglomeration was observed after photonic curing of the films on a Mo contact, but is reduced significantly by using Au or $MoSe_2$/Mo back contacts. Low energy pulses remove the organic capping ligand and bring the nanocrystals into close electrical contact, leading to devices exhibiting multiple exciton generation and extraction. Higher energy pulses sinter the nanocrystal layer and sintered nanocrystal photovoltaic devices are demonstrated.

Table of Contents

List of Tables

List of Figures

Chapter 1: Introduction

One third of the world's population is currently without reliable or sufficient electricity. Additionally, 30 Terawatts (TW) of new energy will be needed by 2050 in the developed world.[1] Meeting these energy demands remain one of society's most pressing problems. Coupled with the ever growing demand for power even in areas where it is readily available, developing new sources of low cost, clean, sustainable energy is one of humanities greatest challenges. Harvesting just a portion of the *15000 TW* of solar radiation that reaches the earth could provide for global energy needs.[2]

Sunlight can be directly converted into electricity using photovoltaic (PV) devices. However, widespread use of photovoltaics is hindered due to simple economics. Solar electricity costs too much in comparison to other sources of energy. The cost of traditional fossil fuel electricity is approximately \$0.10/kWh.[3] While solar costs have been decreasing,[4,5] the cost is roughly \$0.11/kWh-\$0.25/kWh depending on location.[4] Further cost reduction is still needed

Si-based solar cells dominate the solar industry with 90% market share.[6] The price of Si solar cells has dramatically fallen in recent years, reaching a cost of approximately \$0.60-\$0.80/W_p,[7] where W_p is the power output in full sunlight conditions, or peak Watt. Although this is a remarkable reduction, a price below \$0.50/W is needed for grid parity.[3]

One potential strategy for lowering the cost of photovoltaics is direct printing of the light absorber layer. In contrast to the vacuum based deposition techniques currently used in commercial solar cell production, printable solar cells allow inexpensive, high-throughput roll-to-roll fabrication, but require an absorber layer that can be processed in a liquid form (also known as solution processable solar cells). The work in this dissertation

is focused on increasing the efficiency of $Cu(In,Ga)Se_2$ (CIGS) nanocrystal solar inks to achieve a reduction in the fabrication cost of solar cells.

1.1 PHOTOVOLTAIC BASICS

The basic structure of a photovoltaic device is shown in Figure 1.1, along with a band diagram in Figure 1.1B. Light is absorbed by the semiconductor and the p-n junction induces charge separation. The efficiency of the device depends on electron-hole generation by light absorption, followed by electron-hole separation and extraction from the light-absorbing layer. At least one of the contact layers allows light penetration into the device. The power conversion efficiency (PCE) of the device is a ratio of electrical power output compared to the power of the incident light. Typically PCE is measured under an incident flux of 100 mW/cm^2 of Air Mass (AM) 1.5 illumination that replicates the mid-latitude yearly average solar solar spectrum and intensity. Figure 1.1C shows a typical current-voltage curve of a device. The PCE is related to the open-circuit voltage (V_{oc}), the short circuit current (J_{sc}), athe fill factor (FF), and the incident light flux (P_{in}):

$$\eta\ (PCE) = \frac{V_{oc} * J_{sc} * FF}{P_{in}} \qquad (1)$$

The PCE of a single junction solar cell is fundamentally limited to ~34% due to thermal and transmission losses, known as the Shockley-Queisser limit.[8]

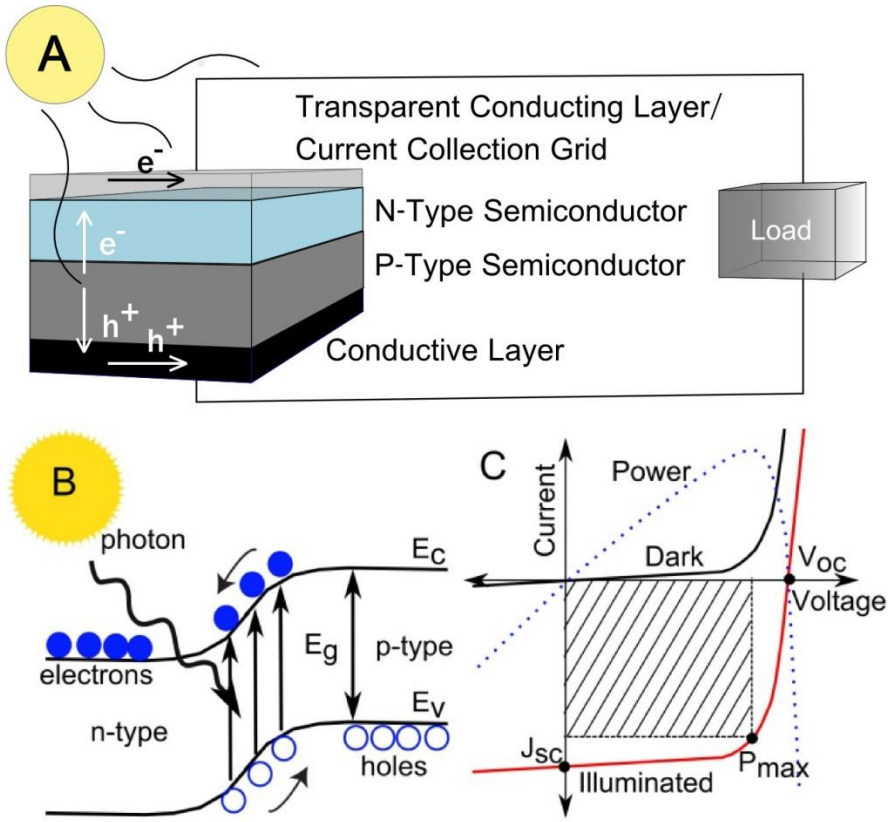

Figure 1.1 A) Basic schematic of a simple p-n junction PV device B) Energy Level Diagram of a p-n junction[9] C) Current-Voltage Output of a typical PV device.[9] B&C reprinted with permission from Elsevier.

The relative cost of power generated by various solar panels can be compared by estimating the price per peak watt ($/Wp). The price of solar power can be reduced by increasing device efficiency to improve power output or reducing the manufacturing cost. Higher device efficiency usually requires more complex fabrication.[10] Losses in efficiency are minimized by optimizing interfaces between materials, which serve as recombination centers. Materials with high crystallinity and purity also reduce charge recombination and improve efficiency.[11] Often this requires high processing temperatures, high vacuum, or toxic environments that are not compatible with roll-to-roll fabrication.

1.2 Si and Thin-Film Photovoltaics

The Si solar cell is a relatively old technology, but dominates the market due to comparatively low cost. Taking advantage of years of research in the semiconductor industry, Si solar cells have demonstrated the highest single junction efficiency of any material.[12] Yet silicon is has indirect bandgap, making it a poor absorber of light and requiring thick layers of Si to absorb the full spectrum of light.[13] Production of Si solar cells is also capital and energy intensive.[14,15]

Thin film semiconductor devices, such as a-Si, CdTe and CIGS, are commercially viable alternatives to polycrystalline and crystalline Si. The cost of these thin film devices, however, has still remained relatively high with respect to Si solar cells. CdTe devices made by First Solar are having a commercial impact, but CIGS and a-Si devices remain only useful for niche markets. For example, in the case of CIGS the highest efficiency devices are made using vacuum and high temperature processes such as co-evaporation, or selenization of sputtered metal layers.[10] Manufacturing processes that lower the cost of thin film inorganic solar cells, without sacrificing performance, are still being sought.

1.3 Solution Processed Photovoltaics

To lower fabrication costs, printed photovoltaics seek to use chemical solutions that are deposited directly on the substrate to grow the absorber film. These materials can be organic or inorganic. Figure 1.2 illustrates the three commonly used non-patterned ink-based deposition methods of doctor-blading, spray-coating and slot-die coating. Doctor-blading, or knife coating, is carried out by running the substrate coated with the material under a knife edge to create a film with uniform thickness. Slot die coating extrudes the liquid from a thin slot onto the moving substrate. Spray coating uses either pressure or ultrasonic nozzles to spray the ink directly onto the substrate.

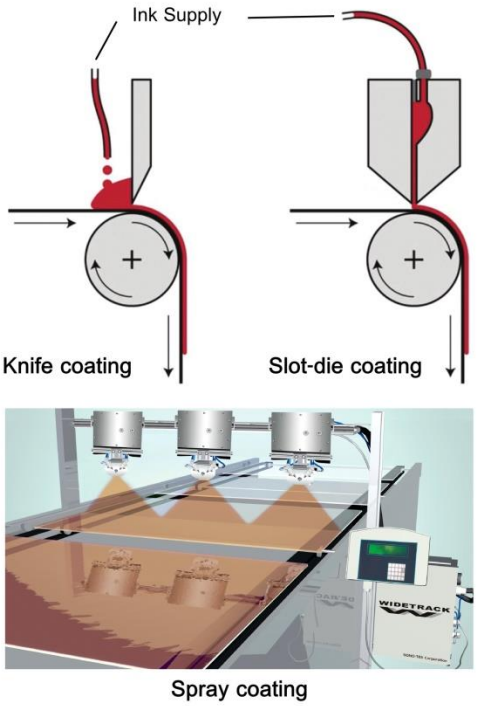

Figure 1.2 Deposition Techniques: A) doctor blading or knife coating,[16] B) slot die coating (© 2012 Wiley Periodicals, Inc.),[16] C) Spray Coating (Courtesy of Sonotek Inc.).

1.4 ORGANIC BASED PHOTOVOLTAICS

Organic semiconductors have been extensively explored to create solution processed solar cells. The active layer in organic photovoltaics (OPVs) is typically a bulk heterojunction in which an interpenetrating layer of donor and acceptor molecules is sandwiched between two electrodes. The typical donor and acceptor molecules are P3HT (poly-3-hexylthiophene) and PCBM (phenyl-C_{61}-butyric acid methyl ester) and PCEs of between 3-4% are commonly measured under inert environment,[16] with a record efficiency of 11.1%.[17] Organic semiconductors are well-suited for solution-based roll-to-roll printing methods, but laboratory-scale OPVs are typically made with batch processes like spin-coating on glass substrates. The long-term stability of OPVs continues

to be a large concern, as the incorporation of moisture and oxygen in the device layers during fabrication leads to device degradation during operation and limits device stability. [20]

Dye sensitized solar cells (DSSC) use both organic and inorganic components. A DSSC uses a mesoporous network of an electron-accepting metal oxide (MO), typically TiO_2 or ZnO. This film is infiltrated with dye (typically ruthenium-based), which serves as the light absorber layer. This structure is paired with an appropriate electrolyte and counter electrode. [18] The use of this structure has been primarily hindered due to the cost of the dyes and the use of a liquid electrolyte.

Recently, the use of Perovskite absorber materials have expanded rapidly.[19] This new research has yielded very high efficiencies in a short amount of time.[17] However, many of the perovskites are sensitive to moisture, which can complicate processing and makes proper encapsulation critical to long-term stability. The long term feasibility and cost of these materials are still under investigation.

1.5 NANOCRYSTAL PHOTOVOLTAICS

Nanocrystal photovoltaics seek to use high stability inorganic materials while retaining the processing advantages of solution processed organic photovoltaics. A variety of different nanocrystals have been incorporated into PV devices, such as PbS, PbSe, CIS, CIGS, CZTS and CdTe.[9,20,21] In general, an arrested precipitation synthesis has been used where molecular reactants are heated in a solvent and an organic molecule is used as a capping ligand to stabilize the nanocrystal growth. The ligand provides solubility in organic solvents, but forms an insulating layer around the nanocrystals that inhibits charge transport.

Two strategies have been pursued to improve charge transport in nanocrystal films with relatively good success: ligand exchange and nanocrystal sintering. The highest efficiencies reported using ligand exchange have been from PbS devices using "atomic" ligands, with the most effective being halide ions.[22] An exchange from organic to inorganic metal chalcogenides (MCC) ligands with $CuInSe_2$ has shown large decreases in device resistance.[23] The highest device efficiency achieved using ligand exchange is 7% using halide-capped PbS devices.[23]

The highest efficiency devices from nanocrystal inks have been achieved by sintering the nanocrystal films. Devices with CdTe nanocrystals sintered on a hot plate in air have reached efficiencies of 12.3%.[24] The highest reported efficiency from a sintered nanocrystal layer has been a $CuIn_{(1-x)}Ga_xSe_{(1-y)}S_y$ device with 12% efficiency using $Cu(In,Ga)S_2$ nanocrystal starting material.[25] The highest efficiency selenized $CuInGaSe_2$ nanocrystals have exhibited 7% efficiency (Chapter 3).[26]

1.6 CU(IN,GA)SE$_2$ NANOCRYSTAL PHOTOVOLTAICS

Our group has pioneered the use of $Cu(In,Ga)Se_2$ inks for photovoltaics. Figure 1.3 shows transmission electron microscopy (TEM) image of the nanoparticles. The nanocrystals are relatively polydisperse and range from 10-25 nm in diameter. After synthesis, the nanocrystals are dispersed in a solvent (generally toluene) and spray deposited directly on the back contact material in an ambient environment. A variety of device architectures are usable (Figure 1.4A). With no heat treatments, devices made in this manner have reached 3.1% PCE (Figure 1.4B). The cross sectional scanning electron microscopy (SEM) image (Figure 1.4C) shows a typical device on an Au back contact.

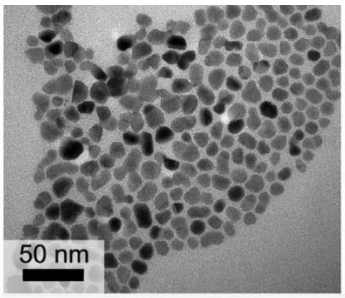

Figure 1.3 A) TEM of CIS nanocrystals[23] (adapted with permission ©2013 American Chemical Society)

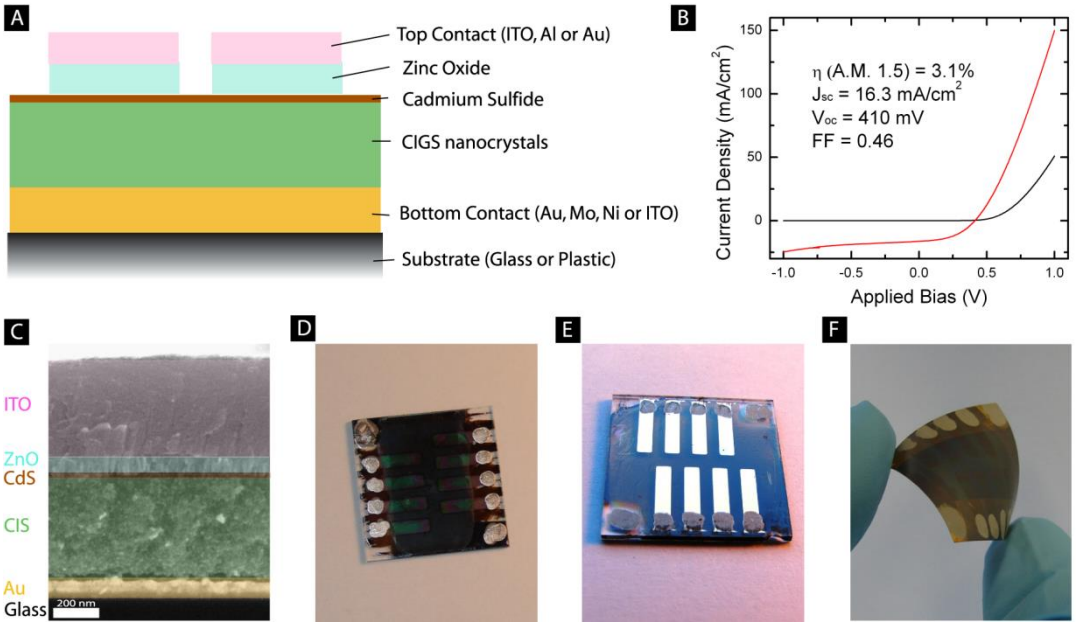

Figure 1.4 (A) Illustration of the device layers with possible deviations from the traditional architectures (B) I-V characteristics of best nanocrystal $CuInSe_2$ device efficiency with power conversion efficiency of 3.1% under AM1.5 illumination. Response under no illumination (black) and under AM1.5 irradiation (red). Reprinted with permission from Akhavan et. al.[27] Copyright 2010 Optical Society of America. (C) Cross sectional SEM image of a typical PV device fabricated on Au back contact. (D,E,F) Photographs of PVs fabricated by spray depositing CIGS nanocrystals on (D) glass, (E) glass with Al top contacts and (F) plastic (kapton). Figure reproduced with permission from *Journal of Solid State Physics*.[28]

1.7 DISSERTATION SUMMARY

This dissertation presents our work to increase the efficiency of Cu(In,Ga)Se2 nanocrystal photovoltaics by sintering the nanocrystal film. After the introduction in Chapter 1, the next three chapters focus on improving device performance by annealing the nanocrystal films under a Se atmosphere, known as selenization. The later chapters look at an alternative sintering approach where the nanocrystal film is exposed to rapid pulses of broadband light, also known as photonic curing.

Chapter 2 looks at the influence of the nanocrystal composition on the selenization process and subsequent device efficiency. While modification of the band gap due to composition change affects the PCE, the primary influence of nanocrystal composition is found to be the quality of the sintered films. Additionally, the PCE of the device is lowered due to a Se/Carbon layer that partially caps the selenized CIGS film.

As presented in Chapter 3, the Se/Carbon layer can be eliminated by annealing the nanocrystal films in Ar before selenization. This pre-selenization anneal also drives Na from the soda-lime glass substrate and improves the nanocrystal sintering process. By using repeated deposition and selenization treatments, a PCE over 7% is demonstrated.

In Chapter 4, ultrasonic spray deposition is explored as a route to scalable nanocrystal PV fabrication. The ultrasonic spray deposition is highly sensitive to the organic content of the nanocrystal ink and the nanocrystal wash procedure determines the organic content of the ink. Highly uniform, reflective nanocrystal films were deposited with 6.6% PCE after selenization.

While selenization leads to higher efficiencies, the treatment adds a high temperature processing step to the nanocrystal PV fabrication. Chapter 5 presents the results of an alternative sintering process known as photonic curing where the nanocrystal film is exposed to a rapid pulse of broadband light. Nanocrystal films are pulsed after

spray deposition on three different back contact materials. The nanocrystals dewet and agglomerate on a Mo back contact, but the agglomeration is reduced significantly when Au or $MoSe_2$/Mo back contacts are used. Increased PCE is demonstrated after photonic curing of the films at low pulse energy. Higher energy pulses sinter the nanocrystal film and the first light sintered nanocrystal PVs are demonstrated.

Chapter 6 details the use of mild photonic pulses to remove the organic capping ligand from the film and increase the nanocrystal electrical contact. Films treated in this manner exhibit very high short circuit currents due to multiple exciton generation and extraction.

Conclusions and potential future research directions are presented in chapter 7.

1.8 REFERENCES

(1) Holdren, J. P. Science and Technology for Sustainable Well-Being. *Science* **2008**, *319*, 424–434.

(2) *Handbook of Photovoltaic Science and Engineering*; Luque, A.; Hegedus, S., Eds.; John Wiley & Sons, Ltd, 2003.

(3) *SunShot Vision Study*; DOE/GO-102012-3037; U.S. Department of Energy, 2012.

(4) Bazilian, M.; Onyeji, I.; Liebreich, M.; MacGill, I.; Chase, J.; Shah, J.; Gielen, D.; Arent, D.; Landfear, D.; Zhengrong, S. Re-Considering the Economics of Photovoltaic Power. *Renew. Energy* **2013**, *53*, 329–338.

(5) Reichelstein, S.; Yorston, M. The Prospects for Cost Competitive Solar PV Power. *Energy Policy* **2013**, *55*, 117–127.

(6) Fraunhofer ISE. Fraunhofer Institiute For Solar Energy Systems ISE: Photovoltaics Report, 2014.

(7) *Footnote Place Holder*.

(8) Henry, C. H. Limiting Efficiencies of Ideal Single and Multiple Energy Gap Terrestrial Solar Cells. *J. Appl. Phys.* **1980**, *51*, 4494–4500.

(9) Stolle, C. J.; Harvey, T. B.; Korgel, B. A. Nanocrystal Photovoltaics: A Review of Recent Progress. *Curr. Opin. Chem. Eng.* **2013**, *2*, 160–167.

(10) Niki, S.; Contreras, M.; Repins, I.; Powalla, M.; Kushiya, K.; Ishizuka, S.; Matsubara, K. CIGS Absorbers and Processes. *Prog. Photovolt. Res. Appl.* **2010**, *18*, 453–466.

(11) Mertens, K. *Photovoltaics: Fundamentals, Technology and Practice*; John Wiley & Sons Ltd, 2014.

(12) Green, M. A.; Emery, K.; Hishikawa, Y.; Warta, W.; Dunlop, E. D. Solar Cell Efficiency Tables (version 44). *Prog. Photovolt. Res. Appl.* **2014**, *22*, 701–710.

(13) Miles, R. W.; Hynes, K. M.; Forbes, I. Photovoltaic Solar Cells: An Overview of State-of-the-Art Cell Development and Environmental Issues. *Prog. Cryst. Growth Charact. Mater.* **2005**, *51*, 1–42.

(14) Peng, J.; Lu, L.; Yang, H. Review on Life Cycle Assessment of Energy Payback and Greenhouse Gas Emission of Solar Photovoltaic Systems. *Renew. Sustain. Energy Rev.* **2013**, *19*, 255–274.

(15) Fthenakis, V. M.; Kim, H. C. Photovoltaics: Life-Cycle Analyses. *Sol. Energy* **2011**, *85*, 1609–1628.

(16) Søndergaard, R. R.; Hösel, M.; Krebs, F. C. Roll-to-Roll Fabrication of Large Area Functional Organic Materials. *J. Polym. Sci. Part B Polym. Phys.* **2013**, *51*, 16–34.

(17) NREL Best Research-Cell Efficienceis Chart http://www.nrel.gov/ncpv/images/efficiency_chart.jpg (accessed Mar 12, 2014).

(18) Hinsch, A.; Veurman, W.; Brandt, H.; Loayza Aguirre, R.; Bialecka, K.; Flarup Jensen, K. Worldwide First Fully up-Scaled Fabrication of 60 × 100 cm2 Dye Solar Module Prototypes. *Prog. Photovolt. Res. Appl.* **2012**, *20*, 698–710.

(19) Snaith, H. J. Perovskites: The Emergence of a New Era for Low-Cost, High-Efficiency Solar Cells. *J. Phys. Chem. Lett.* **2013**, 3623–3630.

(20) Hillhouse, H. W.; Beard, M. C. Solar Cells from Colloidal Nanocrystals: Fundamentals, Materials, Devices, and Economics. *Curr. Opin. Colloid Interface Sci.* **2009**, *14*, 245–259.

(21) Chen, G.; Seo, J.; Yang, C.; Prasad, P. N. Nanochemistry and Nanomaterials for Photovoltaics. *Chem. Soc. Rev.* **2013**.

(22) Ip, A. H.; Thon, S. M.; Hoogland, S.; Voznyy, O.; Zhitomirsky, D.; Debnath, R.; Levina, L.; Rollny, L. R.; Carey, G. H.; Fischer, A.; *et al.* Hybrid Passivated Colloidal Quantum Dot Solids. *Nat. Nanotechnol.* **2012**, *7*, 577–582.

(23) Stolle, C. J.; Panthani, M. G.; Harvey, T. B.; Akhavan, V. A.; Korgel, B. A. Comparison of the Photovoltaic Response of Oleylamine and Inorganic Ligand-Capped CuInSe2 Nanocrystals. *ACS Appl. Mater. Interfaces* **2012**, *4*, 2757–2761.

(24) Panthani, M. G.; Kurley, J. M.; Crisp, R. W.; Dietz, T. C.; Ezzyat, T.; Luther, J. M.; Talapin, D. V. High Efficiency Solution Processed Sintered CdTe Nanocrystal Solar Cells: The Role of Interfaces. *Nano Lett.* **2013**, *14*, 670–675.

(25) Guo, Q.; Ford, G. M.; Agrawal, R.; Hillhouse, H. W. Ink Formulation and Low-Temperature Incorporation of Sodium to Yield 12% Efficient Cu(In,Ga)(S,Se)2 Solar Cells from Sulfide Nanocrystal Inks. *Prog. Photovolt. Res. Appl.* **2013**, *21*, 64–71.

(26) Harvey, T. B.; Mori, I.; Stolle, C. J.; Bogart, T. D.; Ostrowski, D. P.; Glaz, M. S.; Du, J.; Pernik, D. R.; Akhavan, V. A.; Kesrouani, H.; *et al.* Copper Indium Gallium Selenide (CIGS) Photovoltaic Devices Made Using Multistep Selenization of Nanocrystal Films. *ACS Appl. Mater. Interfaces* **2013**, *5*, 9134–9140.

(27) Akhavan, V. A.; Panthani, M. G.; Goodfellow, B. W.; Reid, D. K.; Korgel, B. A. Thickness-Limited Performance of CuInSe2 Nanocrystal Photovoltaic Devices. *Opt. Express* **2010**, *18*, A411–A420.

(28) Akhavan, V. A.; Goodfellow, B. W.; Panthani, M. G.; Steinhagen, C.; Harvey, T. B.; Stolle, C. J.; Korgel, B. A. Colloidal CIGS and CZTS Nanocrystals: A Precursor Route to Printed Photovoltaics. *J. Solid State Chem.* **2012**, *189*, 2–12.

Chapter 2: Influence of Composition on the Performance of Sintered $Cu(In,Ga)Se_2$ (CIGS) Nanocrystal Thin Film Photovoltaic Devices[1]

2.1 INTRODUCTION

One of the most promising thin film photovoltaic (PV) materials is $Cu(In,Ga)Se_2$ (CIGS), as it has exhibited some of the highest efficiencies of any thin film material, of 20%.[1,2] CIGS films are typically processed using high temperature (>500^{o}C) under Se vapor to obtain the appropriate crystal composition and phase, and the highest efficiency devices utilize a series of processing steps,[3] leading to relatively high manufacturing cost. A processing strategy for large-area CIGS thin film processing with significantly lower cost and high throughput, while still enabling high efficiency, is being sought.

In a single processing step, CIGS films can be deposited with a desired composition and crystal phase directly from solution using inks of CIGS nanocrystals. Without high temperature processing, however, devices using these materials have achieved only up to 3% power conversion efficiency (PCE).[4,5] Hillhouse and Agrawal recently demonstrated 12% PCE by converting $Cu(In,Ga)S_2$ nanocrystals to CIGS with high temperature selenization.[6,7] They have also explored selenization of $Cu(In,Ga)Se_2$ nanocrystal films, but have not been able to obtain efficiencies greater than only a few percent, claiming that selenized nanocrystal devices perform very poorly unless sulfide nanocrystals are used as starting material and proposed that Se addition leads to a volume expansion needed to eliminated voids in the selenized film.[6] Here we show that $Cu(In,Ga)Se_2$ nanocrystals can be used as the starting material for high temperature

---

[1] Reproduced in part with permission from Akhavan, V. A.; Harvey, T. B.; Stolle, C. J.; Ostrowski, D. P.; Glaz, M. S.; Goodfellow, B. W.; Panthani, M. G.; Reid, D. K.; Vanden Bout, D. A.; Korgel, B. A. Influence of Composition on the Performance of Sintered Cu(In,Ga)Se2 Nanocrystal Thin-Film Photovoltaic Devices. *ChemSusChem* **2013**, 6, 481-486.
V. Akhavan contributed to all aspects of this publication; C. Stolle, B. Goodfellow, M. Panthani, and D. Reid assisted with nanocrystal synthesis and device fabrication; D. Ostrowski, M. Glaz, and D. Vanden Bout performed LBIC measurements.

selenization to obtain CIGS device efficiencies of over 5%, but that the efficiency is very sensitive to [Ga]/[In+Ga] composition in the nanocrystals as a result of both changing bandgap and a connection with the [Cu]/[Ga+In] content that significantly influences the quality of the selenized films.

2.2 EXPERIMENTAL SECTION

2.2.1 Materials

Oleylamine (OLA) was purchased from TCI America or Corsitech; copper (I) chloride (CuCl; 99.99+%), gallium (III) chloride ($GaCl_3$; 99.999+%), selenium powder (Se; 99.99%), and cadmium sulfate ($CdSO_4$; 99.999%) from Aldrich Chemical Co.; indium (III) chloride ($InCl_3$; 99.999%) from Strem Chemicals; ammonium hydroxide (18M NH_3; ACS certified), toluene (99.99%), ethanol (absolute), and nitric acid (trace metal grade) from Fischer Scientific; and thiourea (> 99.0%) from Sigma-Aldrich. Prior to use, oleylamine was degassed overnight under vacuum at 110^{o}C. All other chemicals were used as received without further purification. Copper (I) chloride, indium (III) chloride, gallium (III) chloride, and degassed oleylamine were stored under nitrogen.

2.2.2 $CuIn_{1-x}Ga_xSe_2$ (CIGS) Nanocrystal Synthesis

CIGS nanocrystals were synthesized using published procedures.[8] In a nitrogen-filled glove box, 5 mmol of CuCl, 10 mmol of Se, 50 mL of degassed oleylamine, and a total of 5 mmol of $InCl_3$ and $GaCl_3$, were combined in a three neck flask. The flask was sealed with septa, removed from the glovebox, and attached to a Schlenk line equipped with a stir plate and a heating mantle. The reaction mixture was stirred and heated to 110^{o}C under vacuum for a 30 minute period. It was then blanketed with nitrogen and heated to 200°C to dissolve all the constituent solids. After 30 minutes of stirring, the reaction mixture was heated to 260°C for an additional 10 minutes. The heating mantle

was removed to allow the reaction to cool to room temperature. The nanocrystals were precipitated with excess ethanol and centrifuged at 4000 rpm for 2 min. The supernatant was discarded and the precipitate was redispersed with a minimal amount of toluene, usually about 5 mL. The dispersion was centrifuged at 4000 rpm for 1 min to precipitate poorly-capped nanocrystals. The supernatant was transferred to a centrifuge tube. Ethanol was added dropwise until the mixture became slightly turbid. After centrifugation at 4000 rpm for 1 min, the supernatant was discarded and the precipitate was dispersed in toluene to a concentration of 200 mg/mL. The nanocrystal dispersion was stored under nitrogen prior to use.

2.2.3 Device Fabrication

Sodalime glass substrates (Delta Techology) were cleaned by sonication in an acetone/isoproponol mixture, followed by rinse with DI water, and drying under nitrogen. Back contact layers of 1 μm Mo (99.95% Lesker, UHP Ar sputtering gas) was deposited by sputter coating in a two-step process. 400 nm of Mo was deposited at 5 mtorr to create a highly adhesive layer to the sodalime glass, and an additional 600 nm of Mo was deposited at 1.5 mtorr for a highly conductive layer. The final sheet resistance was ~1.25 Ω/□.

Nanocrystal dispersions were deposited on the Mo back contacts by spray deposition of 20 mg/ml dispersion of nanocrystals in toluene using a commercial spray gun (Iwata Eclipse HP-CS) operated at 50 psig head pressure. Films were sprayed in one step to a targeted thickness of 1.5 μm. The films were annealed in a hollow graphite cylinder with excess elemental selenium. The cylinder was firmly capped but not gastight. A two-step annealing process was used: 10 minutes at 350°C to remove organic

ligands followed by an increase in temperature to 500°C for 1 hour. Excess Se provides a partial pressure to ensure limited loss of selenium content from the particles.

Following nanocrystal selenization, CdS layer was deposited by chemical bath deposition (CBD). 160 mL of 18.2 MΩ DI water was placed in a crystallization dish with a stir bar, and heated to 70°C. 25 ml of 15 mM $CdSO_4$, 12.5 ml of 1.5 M thiourea and 32 ml of ammonium hydroxide were added and the substrate with the selenized film was immersed in the bath for 20 minutes. The films were rinsed with DI water and dried before depositing the top layers of ZnO and ITO: 50 nm of AC sputtered ZnO (99.9% Lesker, 5 ppm O_2 in Ar sputtering gas) and 600 nm layer of sputtered ITO (99.99% Lesker, UHP Ar sputtering gas). The conductors were deposited through physical shadow masks, so that the active area of the device was 25 mm^2, a 10 mm by 2.5 mm rectangle. After depositing the top contact, a grid of silver paint was added to the device, which reduces the illuminated area to 14 mm^2. Completed devices were placed in a vacuum oven at 200°C for up to 60 hrs to improve the performance.

2.2.4 Materials and Device Characterization

Current-potential (IV) characteristics were collected using a Keithley 2400 general purpose source meter and a Xenon lamp solar simulator (Newport) equipped with an AM1.5G optical filter. The light source intensity was calibrated using a NIST calibrated Si photodiode (Hamamatsu, S1787-08). External quantum efficiency (EQE) was measured as was previously described[8,9] using monochromatic light generated using a commercial monochromator (Newport Cornerstone 260 1/4M) chopped at 213 Hz and focused to a spot size of 1 mm diameter on the active region. EQE measurements were made with the device at zero bias at wavelengths ranging from 300 and 1300 nm in 10 nm increments using a lock-in-amplifier (Stanford Research Systems, model SR830).

Light intensity was calibrated using calibrated photodiodes of silicon (Hamamatsu) and germanium (Judson).

Inductive coupled plasma mass spectroscopy (ICP-MS) data was acquired with an Agilent 7500ce Quadrupole ICP-MS. CIGS nanocrystals (3 mg) were digested in 200 μL of 70 wt% nitric acid (Aldrich, > 99.999%). The resulting lime green solution was diluted 35,000x with 2 wt% nitric acid. The measurement is accurate to parts per trillion (PPT) concentrations, which is five orders of magnitude smaller than the measured concentrations.

XRD was collected on a Bruker-Nonius D8 advance θ−2θ powder diffractometer equipped with a Bruker Sol-X Si(Li) solid state detector and 1.54 Å radiation (Cu K_α). Data were collected at 0.01 increments of 2θ at a scan rate of 6°/min. Scanning electron microscope (SEM) images were collected with a Zeiss microscope equipped with an InLens detector operating at 5 kV accelerating voltage.

X-ray photoelectron spectroscopy (XPS) was performed on a Kratos Photoelectron Spectophotometer equipped with a tungsten coil charge neutralizer, high intensity monochromatic Al-kα X-ray source, and a 180 hemispherical electron energy analyzer. The charge neutralizer was operated at constant 4.8 V during data collection. Collected spectra were analyzed using CasaXPS software. Charging on the samples was corrected by shifting the C 1s peaks to value expected of hydrocarbons at 284.5 eV. Shirley background was used to subtract out the baseline before integrating the area under the peak for compositional analysis. Each peak area was divided by the corresponding relative sensitivity factor (RSF) value and then normalized to yield the measured composition in the sample.

Light beam induced current (LBIC) microscopy was performed as previously described[10] using a 473 nm diode-pumped laser from CrystaLaser at a power of around

600 nW, focused through a 50x, 0.8 numerical aperture Olympus objective mounted in a Nikon Diaphot 300 inverted microscope. The device was scanned over the focused light beam with a piezoelectric stage from Physik Instrumente (model E-501.00) and photocurrent was measured at each step to generate an image map of the local photocurrent generation. The photocurrent was measured through a transimpedance amplifier built in house with a gain of 10^4. For further noise filtering the incident light was chopped at 373 Hz and the oscillating photocurrent signal from the transimpedance amplifier was measured with an EG&G DSP lock-in amplifier (model 7220).

2.3 Results and Discussion

CIGS nanocrystals with varying [Ga]/[In+Ga] content were synthesized by changing [$InCl_3$] and [$GaCl_3$] added to the reaction, as reported previously.[8] The reactions yield nanocrystals that are relatively polydisperse with diameters ranging from 10 nm up to 35 nm and there was not any noticeable difference in size with change in composition. The nanocrystal composition was studied using XPS and ICP-MS, as shown in Figure 2.1. ICP-MS provides a measure of the overall bulk composition of nanocrystals, whereas XPS is a surface-sensitive technique. The [Ga]/[In+Ga] composition in the nanocrystals followed approximately the composition of reactant added to the nanocrystal synthesis—i.e., the targeted composition—with just slightly less Ga incorporated than expected. Generally, however, the nanocrystals were found to be deficient in Cu with [Cu]/[In+Ga] typically less than 1, and the highest Cu deficiency was observed in the nanocrystals without Ga. The Cu composition measured by XPS was especially low compared to the ICP-MS measurements, indicating that the surfaces of the nanocrystals were particularly Cu-poor and that most of Cu deficiency was located at the

nanocrystal surfaces. This is consistent with the fact that no phase impurities were detected by XRD.

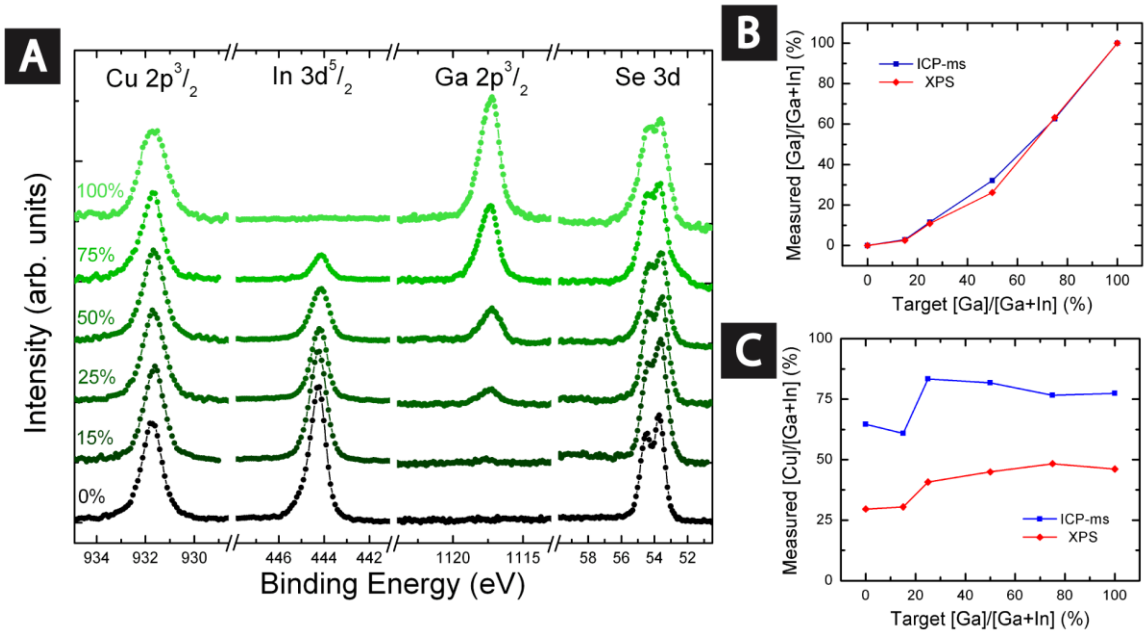

Figure 2.1 (A) XPS of CIGS nanocrystals synthesized with the varying [Ga]/[In+Ga] precursor ratios noted next to each spectrum. Data are normalized to the height of the Cu $2p^3/_2$ peak. (B) [Ga]/[Ga+In] and (C) [Cu]/[Ga+In] content measured by XPS and ICP-MS compared to the [Ga]/[Ga+In] reactant ratio (i.e., target).

Nanocrystal films were deposited on Mo-coated soda lime glass substrates and sintered under Se vapor at 500°C. PV devices were fabricated using these films. Table 1 summarizes the device performance of PVs with CIGS nanocrystals of different [Ga]/[In+Ga]. Without selenization, the highest efficiency devices had very little Ga content, [Ga]/[In+Ga]=2.9%. The highest efficiency selenized devices (PCE=5.1%) on the other hand had significant Ga content, with [Ga]/[In+Ga]=32%. The device response of the champion selenized CIGS nanocrystal PV from Table 1 with PCE of 5.1% is shown in Figure 2.2. The external quantum efficiency (EQE) was close to 50% for most

wavelengths. The champion device had [Ga]/[In+Ga] content close to that of the record efficiency vapor-deposited CIGS device.[1,11]

Table 2.1 PV performance of CIGS nanocrystal devices without sintering (Nanocrystal Absorber). The Ga and Cu content (x=[Ga]/[In+Ga] and y=[Cu]/[Ga+In]) was determined by ICP-MS.

Target	Measured		Nanocrystal Absorber			
x (%)	*x* (%)	*y* (%)	V_{oc} (mV)	J_{sc} (mA/cm^2)	FF	PCE (%)
0	0	64.5	510	7.53	0.38	1.44
15	2.9	61.0	540	7.43	0.42	1.69
25	11.6	83.3	374	6.55	0.35	0.86
50	32.1	82.0	463	4.31	0.42	0.85
75	62.6	76.9	450	4.01	0.40	0.72
100	100	77.5	435	3.15	0.44	0.61

Table 2.2 PV performance of CIGS nanocrystal devices with (Selenized Absorber) sintering. The Ga and Cu content (x=[Ga]/[In+Ga] and y=[Cu]/[Ga+In]) was determined by ICP-MS.

Target	Measured		Selenized Absorber			
x (%)	*x* (%)	*y* (%)	V_{oc} (mV)	J_{sc} (mA/cm^2)	FF	PCE (%)
0	0	64.5	227	2.77	0.29	0.18
15	2.9	61.0	240	8.50	0.34	0.69
25	11.6	83.3	320	13.59	0.36	1.56
50	32.1	82.0	526	20.10	0.48	5.10
75	62.6	76.9	478	9.08	0.35	1.51
100	100	77.5	205	1.81	0.28	0.10

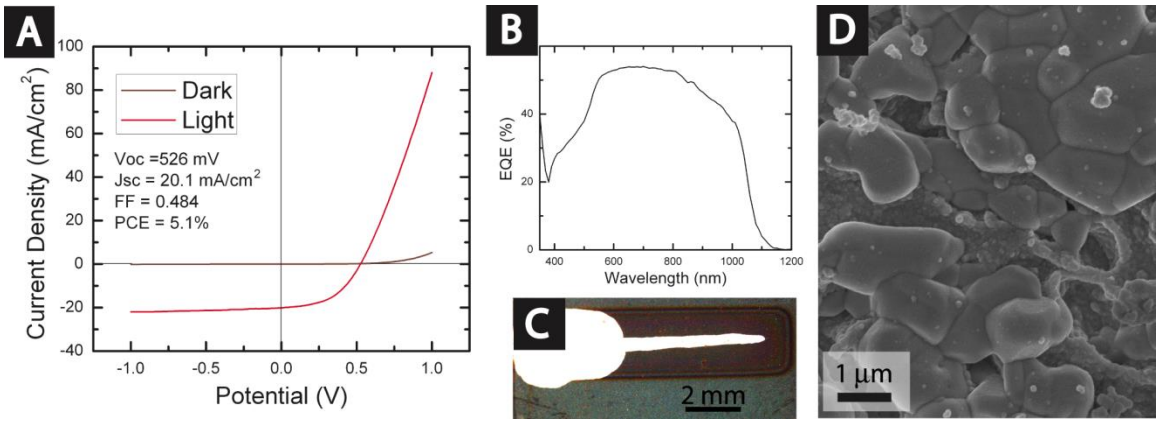

Figure 2.2 Selenized CIGS nanocrystal PV device with 5.1% PCE. [Ga]/[In+Ga]=0.32, as determined by ICP-MS. (A) IV response under AM1.5 illumination, (B) EQE, (C) optical image of the device with painted silver contacts, and (D) SEM of the selenized CIGS nanocrystal absorber layer. The J_{sc} estimated from the EQE measurements of 20.3 mA/cm^2 is consistent with the measured device J_{sc} of 20.1 mA/cm^2.

The band gap of CIGS depends on the [Ga]/[In+Ga] composition. Figure 2.3 shows XRD of the nanocrystal films before and after selenization and the absorption edge determined from the EQE measurements. The absorption edge shifted and the (112) diffraction peak shifted as expected to higher 2θ with changing [Ga]/[Ga+In] content in the film, and narrowed significantly after selenization due to crystal grain growth. The (112) peaks do not shift upon sintering, indicating that the [Ga]/[Ga+In] in the film does not change with sintering. The bandgap of the selenized nanocrystal layers determined from EQE measurements are only slightly lower than the expected bandgap based on reported values for vapor-deposited CIGS films (Figure 2.3D).

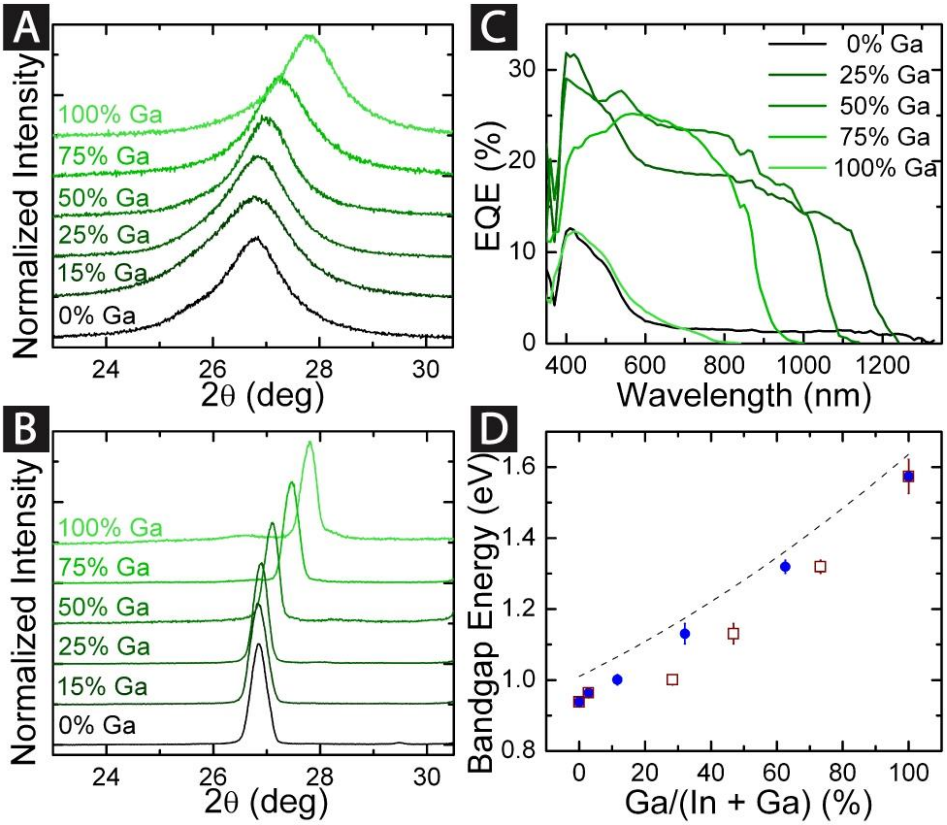

Figure 2.3 XRD showing the (112) chalcopyrite reflection of CIGS nanocrystal films (A) before and (B) after selenization. The targeted [Ga]/[In+Ga] content is noted. (C) EQE of PVs of selenized CIGS nanocrystal films with the noted target [Ga]/[In+Ga] composition. (D) Bandgap determined from the absorption edge in the EQE measurements of PVs with selenized nanocrystal films with varying [Ga]/[In+Ga] as determined by ICP:MS analysis (blue circles) or calculated by Vegard's Law (brown boxes) compared to the vapor deposited CIGS bandgap reported from fluorescence measurements (dashed line).[11]

The device efficiencies in Table 1 varied significantly with nanocrystal composition from as low as 0.1% to just over 5%. This large variation in efficiency was primarily due to differences in film morphology after selenization. Figure 2.4 shows SEM images of selenized films of nanocrystals with different composition. Three distinct types of features were observed: large sintered crystals, exposed back contact and

amorphous coating. The films with the least amorphous coating and most exposed sintered CIGS grains led to the highest efficiency. LBIC maps of active device areas showed that regions coated with amorphous material were mostly inactive (Figure 2.6) and only the regions of the film with exposed sintered crystal contributed strongly to the current output of the device. The active regions of the absorber layer had photocurrents roughly five times higher than the least active regions of the absorber layer. XPS showed that the amorphous layer was C and Se. Figure 2.5A shows a cross-section SEM of a selenized CIGS nanocrystal film with a targeted Ga content of 25% (actual, 12%). The CIGS film is coated by a thin layer of the amorphous by-product. Ar^+ etching exposes the underlying crystalline layer to reveal Cu, In, and Ga. As the SEM images in Figure 2.4 show, the most uniform films with exposed grains had both In and Ga.

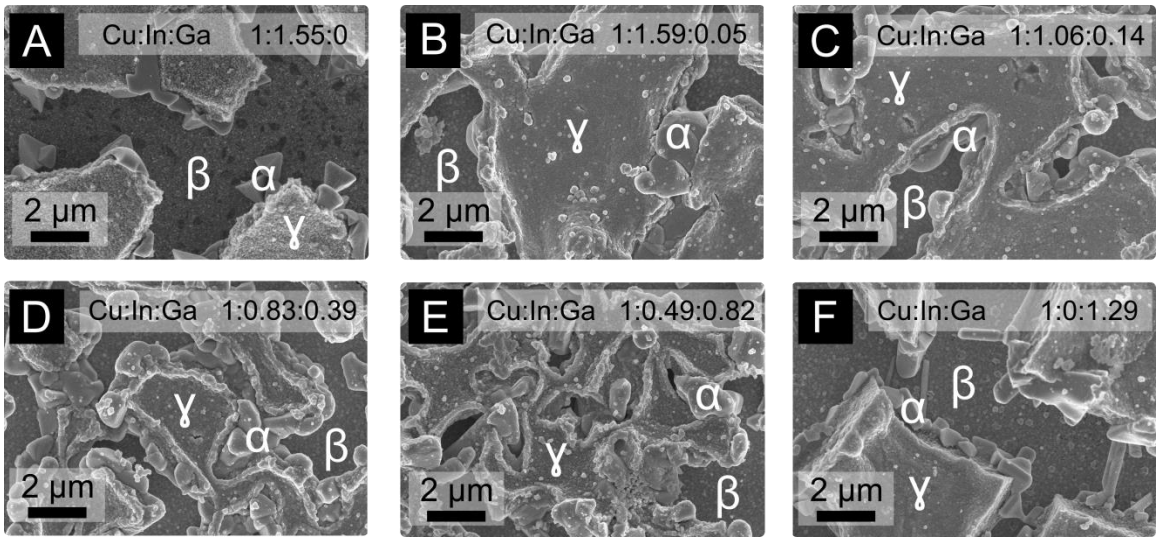

Figure 2.4 SEM images of selenized CIGS nanocrystal films with targeted [Ga]/[Ga+In] of (A) 0%, (B) 15%, (C) 25%, (D) 50%, (E) 75% and (F) 100%. The Cu, In and Ga composition measured by ICP:MS is noted on each image (and listed in Table 1). On each image, sample areas containing large sintered crystals, exposed back contact and amorphous coating are labeled with Greek letters α, β and γ, respectively.

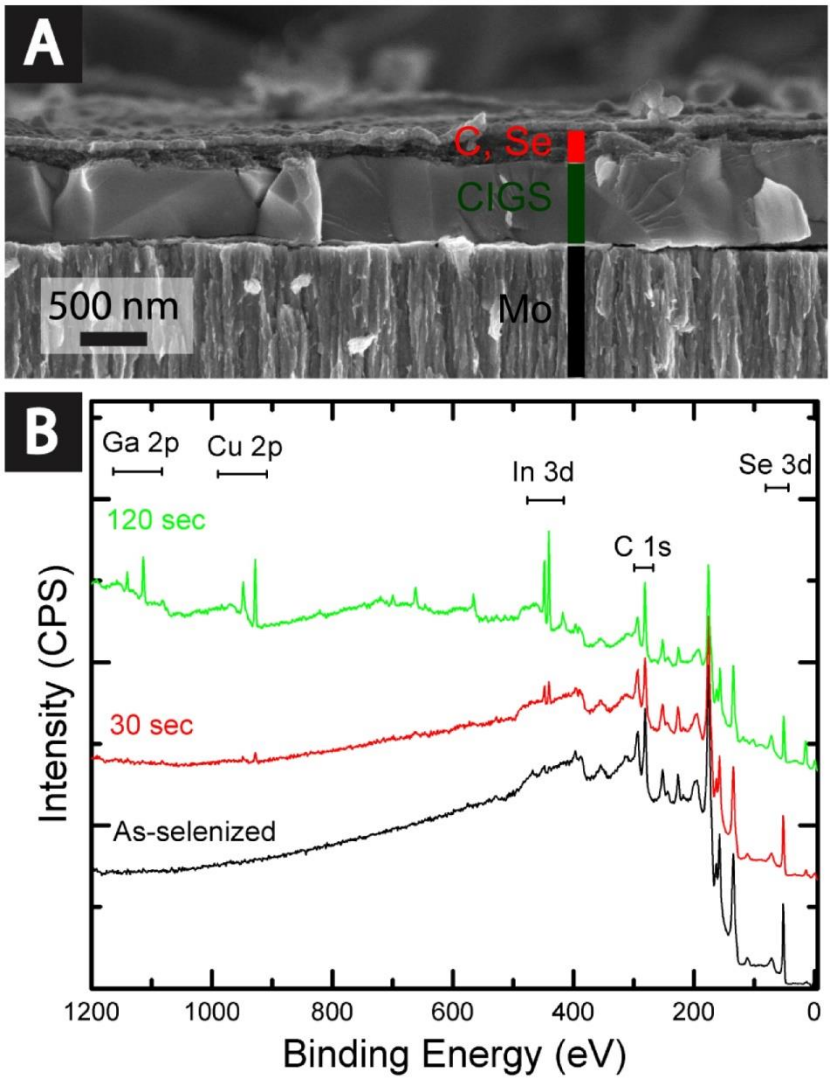

Figure 2.5 (A) SEM image of a cross sectioned selenized CIGS (target Ga was 25%; actual was 12%) nanocrystal film with tree layers of Mo substrate (black), CIGS (green) and an amorphous coating (red). (B) XPS profiles of the selenized layer before and after sputtering.

Figure 2.6 compares LBIC maps of a $CuInSe_2$ selenized nanocrystal device to the highest efficiency CIGS selenized nanocrystal device from Table 1. The $CuInSe_2$ nanocrystals were very Cu-poor [Cu]/[In]=0.65 and the film sintered with large islands of amorphous material as shown in Figure 2.6A. This amorphous C/Se coating blocked

incident photons from reaching the CIGS crystals underneath, limiting photogenerated current (Figure 2.6C). The exposed grains surrounding the larger amorphous islands yield a significantly higher photocurrent than the rest of the device and are the main source of power on this device. The higher efficiency CIGS device had significantly less amorphous coating and higher density of exposed grains, Figure 2.6D. These films were much less copper deficient, with [Cu]/[In+Ga]=0.82—similar to that of record efficiency CIGS devices.[1] The LBIC map of this device, Figure 2.6F, reveals a high spatial density of photoactive regions across the film as compared to the LBIC map of the $CuInSe_2$ device shown in Figure 2.6C.

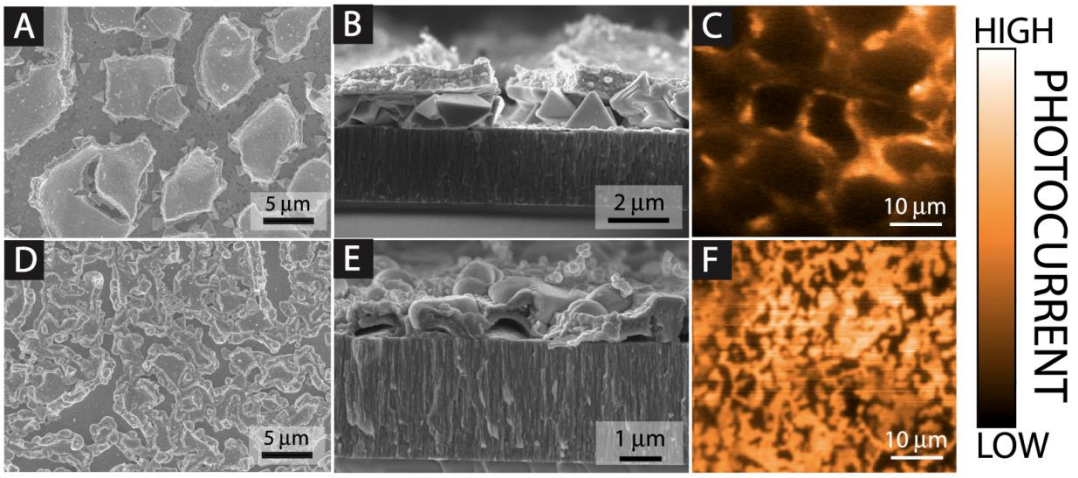

Figure 2.6 SEM images (top view A and D, cross sectional view B and E) and LBIC (C and F) maps of two different devices with selenized layers: A–C are of a $CuInSe_2$ device and C–F are of the highest efficiency CIGS device from Table 1 with actual compositions of $Cu_{0.65}InSe_2$ and $Cu_{0.82}In_{0.68}Ga_{0.32}Se_2$, respectively. The high photocurrent regions of the absorber layer had approximately 5x the output density of the low photocurrent regions.

2.4 CONCLUSIONS

CIGS nanocrystals can be synthesized with targeted [Ga]/[In+Ga] and spray-deposited to create films with a specific band gap for optimal absorption and V_{oc}. The as-deposited nanocrystal films contain a significant amount of organic capping ligand that limits charge transport in the film and in turn, efficiency. Through sintering the nanocrystal films with a high temperature selenization process, device efficiencies of at least 5% can be attained. The nanocrystal composition was shown to significantly influence the quality of the sintered film. In some cases, an amorphous coating of C/Se forms and inhibits performance. Of the nanocrystal-based devices studied here, those with significant Ga far outperformed sintered $CuInSe_2$ nanocrystals. Selenized CIGS nanocrystal films with 30% Ga had short circuit current densities greater than 20 mA/cm^2, which is beginning to approach those of vapor-deposited CIGS devices. The poor performance of the sintered $CuInSe_2$ nanocrystal films derived from their non-uniform morphology, which probably relates to the fact that the nanocrystals were very Cu-deficient. Both band gap and film quality underlie device efficiency. The band gap can be rationally tuned by changing [Ga]/[In+Ga] in the nanocrystals. The sintering morphology, however, is also influenced by nanocrystal composition, mostly related to the Cu content in the film. LBIC mapping of the absorber layers revealed the photo-active regions and how sintering morphology relates to power output of the PV device.

2.5 ACKNOWLEDGEMENTS

We thank Nate Miller and Hugo Celio for help with ICP-MS and XPS measurements. Financial support of this work was provided by the Robert A. Welch Foundation (F-1464), the Air Force Research Laboratory (FA-8650-07-2-5061) and the NSF Industry/University Cooperative Research Center on Next Generation Photovoltaics (IIP-1134849).

2.6 REFERENCES

(1) Repins, I.; Contreras, M. A.; Egaas, B.; DeHart, C.; Scharf, J.; Perkins, C. L.; To, B.; Noufi, R. 19·9%-Efficient ZnO/CdS/CuInGaSe2 Solar Cell with 81·2% Fill Factor. *Prog. Photovolt. Res. Appl.* **2008**, *16*, 235–239.

(2) Green, M. A.; Emery, K.; Hishikawa, Y.; Warta, W.; Dunlop, E. D. Solar Cell Efficiency Tables (version 39). *Prog. Photovolt. Res. Appl.* **2012**, *20*, 12–20.

(3) Contreras, M. A.; Tuttle, J.; Gabor, A.; Tennant, A.; Ramanathan, K.; Asher, S.; Franz, A.; Keane, J.; Wang, L.; Scofield, J.; *et al.* High Efficiency Cu(In,Ga)Se2-Based Solar Cells: Processing of Novel Absorber Structures. In *IEEE Photovoltaic Specialists Conference - 1994, 1994 IEEE First World Conference on Photovoltaic Energy Conversion, 1994., Conference Record of the Twenty Fourth*; Dec; Vol. 1, pp. 68–75 vol.1.

(4) Akhavan, V. A.; Panthani, M. G.; Goodfellow, B. W.; Reid, D. K.; Korgel, B. A. Thickness-Limited Performance of CuInSe2 Nanocrystal Photovoltaic Devices. *Opt. Express* **2010**, *18*, A411–A420.

(5) Akhavan, V. A.; Goodfellow, B. W.; Panthani, M. G.; Steinhagen, C.; Harvey, T. B.; Stolle, C. J.; Korgel, B. A. Colloidal CIGS and CZTS Nanocrystals: A Precursor Route to Printed Photovoltaics. *J. Solid State Chem.* **2012**, *189*, 2–12.

(6) Guo, Q.; Ford, G. M.; Hillhouse, H. W.; Agrawal, R. Sulfide Nanocrystal Inks for Dense Cu(In1−xGax)(S1−ySey)2 Absorber Films and Their Photovoltaic Performance. *Nano Lett.* **2009**, *9*, 3060–3065.

(7) Guo, Q.; Ford, G. M.; Agrawal, R.; Hillhouse, H. W. Ink Formulation and Low-Temperature Incorporation of Sodium to Yield 12% Efficient Cu(In,Ga)(S,Se)2 Solar Cells from Sulfide Nanocrystal Inks. *Prog. Photovolt. Res. Appl.* **2013**, *21*, 64–71.

(8) Panthani, M. G.; Akhavan, V.; Goodfellow, B.; Schmidtke, J. P.; Dunn, L.; Dodabalapur, A.; Barbara, P. F.; Korgel, B. A. Synthesis of CuInS2, CuInSe2, and Cu(InxGa1-x)Se2 (CIGS) Nanocrystal "Inks" for Printable Photovoltaics. *J. Am. Chem. Soc.* **2008**, *130*, 16770–16777.

(9) Akhavan, V. A.; Panthani, M. G.; Goodfellow, B. W.; Reid, D. K.; Korgel, B. A. Thickness-Limited Performance of CuInSe2 Nanocrystal Photovoltaic Devices. *Opt. Express* **2010**, *18*, A411–A420.

(10) Ostrowski, D. P.; Glaz, M. S.; Goodfellow, B. W.; Akhavan, V. A.; Panthani, M. G.; Korgel, B. A.; Vanden Bout, D. A. Mapping Spatial Heterogeneity in Cu(In1−xGax)Se2 Nanocrystal-Based Photovoltaics with Scanning Photocurrent and Fluorescence Microscopy. *Small* **2010**, *6*, 2832–2836.

(11) Repins, I.; Contreras, M.; Romero, M.; Yan, Y.; Metzger, W.; Li, J.; Johnston, S.; Egaas, B.; DeHart, C.; Scharf, J.; *et al.* Characterization of 19.9%-Efficient CIGS Absorbers. In *33rd IEEE Photovoltaic Specialists Conference, 2008. PVSC '08*; 2008; pp. 1–6.

Chapter 3: Copper Indium Gallium Selenide (CIGS) Photovoltaic Devices Made Using Multistep Selenization of Nanocrystal Films[2]

3.1 INTRODUCTION

$Cu(In_xGa_{1-x})Se_2$ (CIGS) has strong optical absorption and a favorable band gap for thin film photovoltaics, with the highest reported polycrystalline thin film efficiency of any material of just over 20%.[1] High efficiency devices can be made by co-evaporation[2–4] or high temperature annealing of vacuum-sputtered metals under selenium vapor (i.e. selenization).[5] Commercialization of CIGS PVs using these processes has been challenging due to high process complexity,[5–7] relatively large capital requirements,[8] inefficient materials usage,[9,10] and spatial composition and thickness non-uniformity in large-area devices.[6,11,12] Non-vacuum, solvent-based CIGS layer deposition provides an alternative strategy with potentially higher throughput at significantly lower cost.[13]

PV devices with power conversion efficiency (PCE) of just over 3% have been made by room temperature, ambient spray deposition of $CuInSe_2$ nanocrystals.[14] The electrically insulating organic capping ligands used to stabilize and disperse the nanocrystals in solvents are largely responsible for the limited device efficiency.[15] Replacing the capping ligands with small molecules like metal chalcogenide complexes (MCCs) has improved charge extraction and led to slightly higher device internal quantum efficiency but not yet significant enhancements in PCE.[16] Significantly higher PCE has been achieved by sintering nanocrystals into polycrystalline films.[17,18] For

---

[2] Reproduced in part with permission from Harvey, T. B.; Mori, I.; Stolle, C. J.; Bogart, T. D.; Ostrowski, D. P.; Glaz, M. S.; Du, J.; Pernik, D. R.; Akhavan, V. A.; Kesrouani, H.; Vanden Bout, D. A.; Korgel, B. A. Copper Indium Gallium Selenide (CIGS) Photovoltaic Devices Made Using Multistep Selenization of Nanocrystal Films. *ACS Appl. Mater. Interfaces* **2013**, 5, 9134–9140.
I. Mori, C. Stolle, J. Du, D. Pernik, V. Akhavan, and H. Kesrouani assisted with nanocrystal synthesis and device fabrication; T. Bogart performed XPS measurements; D. Ostrowski, M. Glaz, and D. Vanden Bout performed LBIC measurements.

instance, the highest reported efficiency of 12.0% for a solvent-deposited nanocrystal device has been achieved by selenizing a $Cu(In_xGa_{1-x})S_2$ nanocrystal layer.[18,19] Solvent-deposited sub-micrometer diameter metal oxide particles[20,21] and metal nitrate salt solutions[22] have also been selenized to fabricate CIGS devices with reasonable efficiencies, but composition has been difficult to control over larger areas using these approaches, often with significant oxygen, chloride and nitrate contamination. Selenization of single-phase chalcopyrite $Cu(In_xGa_{1-x})Se_2$ nanocrystals should provide more precise control over layer composition. Significant carbon in these nanocrystal films from the capping ligands, however, has limited device efficiency. The highest reported PCE for selenized $Cu(In_xGa_{1-x})Se_2$ nanocrystals is 5.1%, limited in large part by the formation of a carbon-containing impurity layer.[23] Similar impurity layers have been observed in selenized films of ink-deposited nitrate-containing salts,[22] $CuIn_xGa_{1-x}S_2$ nanocrystals,[17] multiphase $CuInSe_2$ nanoparticles,[24] and $Cu_{2-x}S$ nanoparticle/In acetate mixtures.[25]

Various strategies exist for reducing carbon contamination in solution-processed CIGS films. For instance, the highest device efficiency of a solution-processed CIGS PV of 15.2% was achieved by selenizing carbon-free hydrazine-derived molecular reactants.[26-28] This approach, however, requires highly toxic and potentially explosive hydrazine and would be very costly to use in a manufacturing setting. Nitrate-derived metal salt solutions have been annealed to remove carbon before sulfurization and selenization,[29] but without significant improvement in device efficiency.[22] "Carbon-free" $CuInSe_2$ films have been made by selenizing $Cu_{11}In_9$ nanocrystals capped with disodium citrate, but the formation of significant copper selenide during the process required toxic cyanide (KCN) etching to make functioning PVs.[30] Mixtures of Cu Oxide, In hydroxide, and Ga acetylacetonate dissolved butyldithiocarbamic acid[31] and aqueous dispersions of

CuS and In_2S_3 nanocrystals mixed with Cu and In chlorides[32] have also been selenized to yield devices that are largely carbon-free with 8.8% and 6% efficiency, respectively.

Here, we report that the typical carbon contamination layer in selenized CIGS nanocrystal films can be alleviated by employing a brief heating of a $Cu(In_xGa_{1-x})Se_2$ nanocrystal layer in Ar at 525°C prior to selenization. This process also drives sodium into the Mo back contact from the underlying soda-lime glass substrate that significantly enhances sintering of the CIGS nanocrystals during selenization and provides better processing control. Shortened selenization time helps retain device integrity by limiting conversion of the Mo back contact to $MoSe_2$. Some $MoSe_2$ is needed because it improves electrical contact with the CIGS layer, but excessive $MoSe_2$ formation leads to film delamination. With increased selenization rates, multiple processing steps of nanocrystal deposition and selenization were employed to create selenized CIGS films that were thicker and more uniform than possible with a single nanocrystal deposition and selenization step. By adding a NaCl salt bath treatment after the initial pre-selenization anneal, devices with over 7% efficiency could be fabricated from selenized (sulfur-free) $Cu(In_xGa_{1-x})Se_2$ nanocrystals. Light beam induced current (LBIC) mapping showed that the active device regions of devices have significantly enhanced photocurrent when the pre-selenization anneal is employed.

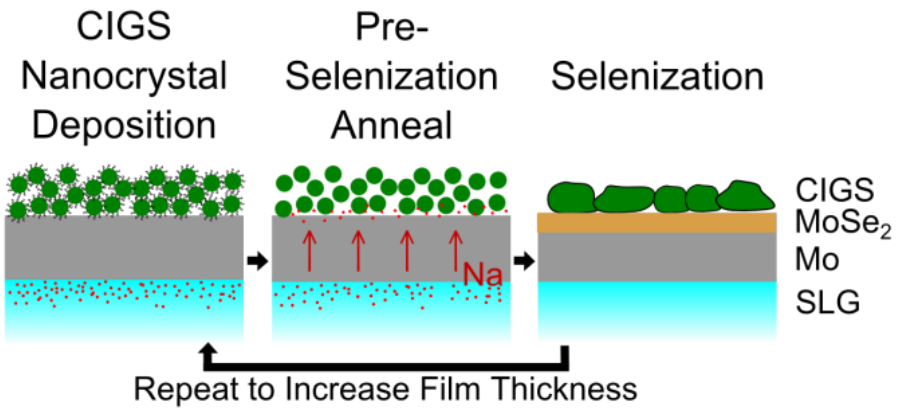

Figure 3.1 Schematic of optimal selenization process

3.2 Experimental Details

3.2.1 Materials

Se powder (99.99%), CuCl (99.99+%), $GaCl_3$ (99.999+%), and $CdSO_4$ (99.999%) was received from Aldrich Chemical Co.; InCl3 (99.999%) from Strem Chemicals; Oleylamine (OLA) from TCI America; Ethanol (absolute), toluene (99.99%), and ammonium hydroxide (18M NH3; ACS certified) from Fischer Scientific; and thiourea (> 99.0%) from Sigma-Aldrich. Oleylamine was degassed overnight at 110°C under vacuum. All other chemicals were used without additional purification.

3.2.2 $CuIn_xGa_{1-x}Se_2$ (CIGS) nanocrystal synthesis

Published procedures[13,23] were used to synthesize CIGS nanocrystals with a targeted composition of $Cu_{0.8}In_{0.7}Ga_{0.3}Se_2$. In a N_2 filled glovebox, 50 mL of degassed OLA, 5 mmol of CuCl, 2.5 mmol of $InCl_3$, 2.5 mmol of $GaCl_3$, and 10 mmol of Se were added to a three-neck flask. After degassing the mixture at 110°C for 30 minutes on a Schlenk line, the flask was filled with nitrogen and the temperature elevated to 200°C for 30 minutes, followed by further heating to 260°C for 10 minutes. After cooling to room temperature, centrifugation was used to wash the particles using ethanol and toluene as

anti-solvent and solvent. Toluene was added to the reach a final nanocrystal concentration of 20 mg/mL.

Sodalime glass (Delta Techology) was sonicated in an acetone/isoproponol mixture, then in DI water, and dried with nitrogen. 1 μm thick Mo (Lesker 99.95%) layers were sputter-coated in two steps; a 400 nm adhesive layer of Mo at 5 mtorr followed by a 600 nm of highly conductive Mo at 1.5 mtorr to give a total sheet resistance of ~1.0 Ω/□.

CIGS nanocrystals were spray-deposited using an Iwata Eclipse HP-CS spray gun operated at 25 psig head pressure. Films (400–1500 nm thick) were annealed under Ar at temperatures between 425°C and 525°C. Selenization was carried out by placing the substrates into a hollow graphite cylinder in a nitrogen-filled glovebox with a boat of elemental selenium. The chamber was tightly capped and removed from the glovebox and annealed for 10 minutes at 500°C.

3.2.3 PV device fabrication

Following selenization, 50 nm of CdS was deposited by chemical bath deposition (CBD). In a crystallization dish, 160 mL of 18.2 MΩ DI water was heated to 80°C. 25 ml of 15 mM $CdSO_4$, 12.5 ml of 1.5 M thiourea and 32 ml of ammonium hydroxide were added and the selenized films were immersed for 15 minutes. 50 nm of ZnO (99.9% Lesker) was sputtered in a 5 ppm O_2/Ar atmosphere, followed by sputtering of a 600 nm ITO (99.99% Lesker) layer in an Ar atmosphere through physical shadow masks to create a 10 mm by 2.5 mm active area. Silver paint grids were added to increase lateral conductivity, reducing the active area to 10 mm^2. Performance was improved by baking completed devices up to 24 hrs at 200°C.

3.2.4 Materials and Device Characterization

Current-potential (IV) characteristics were collected using a Keithley 2400 source meter under AM1.5G illumination (100 mW/cm^2).A NIST calibrated Si photodiode (Hamamatsu, S1787-08) was used to tune light intensity. External quantum efficiency (EQE) was measured as previously described.[14, 23] Monochromatic light (Newport Cornerstone 260 1/4M) at wavelengths ranging from 300 to 1300 nm in 10 nm steps was chopped at 213 Hz and focused to a 1 mm diameter spot size on the device at zero bias. EQE was measured using a lock-in-amplifier (Stanford Research Systems, model SR830) after calibrating light intensity with silicon (Hamamatsu) and germanium (Judson) photodiodes.

Scanning electron microscope (SEM) images were collected after CdS deposition with the InLens detector of a Zeiss microscope operating at 5 kV.. Thermogravimetric analysis (TGA) was collected using a Mettler-Toledo DCS/TGA instrument with a temperature ramp of 20^{o}C/min followed by a temperature hold at 425, 475, or 525 °C for 1 hour. Nanocrystal composition was verified via energy-dispersive X-ray spectroscopy (EDS) carried out on a Quanta 650 FEG SEM equipped with a Bruker XFlash EDS Detector 5010. EDS spectra of nanocrystals drop-cast on a Si wafer were generated at 20 kV accelerating voltage and a working distance of 10 mm with a spot size of 5. EDS spectra were integrated to determine nanocrystal composition with Bruker ESPRIT software.

XPS data were taken using a Kratos (Axis Ultra) instrument, utilizing a monochromated 1486.5 eV Al-K_α X-ray source. Spectra were collected using a pass energy of 20 eV at 0.1 eV intervals and 1500 ms integration time with a 300 μm x 700 μm aperture. A Shirley baseline was used for background subtraction and sample charging was corrected by shifting the Mo^0 $3d_{5/2}$ to a binding energy of 228.0 eV. The

Mo 3d region was fit using Voigt profiles (30% Gaussian character) with peak centers at 228.0, 228.7, 232.2, and 232.8 eV corresponding to Mo^0, $MoSe_2$, Na_xMoO_y, and MoO_3, respectively, for the $3d_{5/2}$ spin. The $3d_{3/2}$ peaks were centered at +3.13 eV from their $3d_{5/2}$ counterparts with the intensity ratio held at 3:2 in congruence with the spin-orbit splitting for Mo d-orbitals. Casa XPS was used with Kratos sensitivity factors to determine the elemental composition of the samples.

Light beam induced current (LBIC) microscopy was collected in the same manner as previously described.[23,35] Image maps were created by scanning a 473 nm laser (CrystaLaser) at a power of 38 ± 4 nW over devices and measuring the photocurrent at each step.

3.3 Results and Discussion

PV devices were fabricated by spray-depositing a 800 nm layer of oleylamine-capped $Cu_{0.8}(In_{0.7}Ga_{0.3})Se_2$ nanocrystals approximately 15 nm in diameter on Mo-coated soda-lime glass followed by selenization in a tightly capped graphite cylinder. We have shown previously that sintering the CIGS nanocrystals in this closed chamber traps carbon eliminated from the nanocrystal film and leads to a residual coating carbon and selenium, which LBIC maps revealed to diminish device performance.[23] This motivated us to explore a pre-selenization anneal to remove most of the organic ligand from the nanocrystal film prior to being placed in the selenization chamber. TGA of CIGS nanocrystals (Figure 3.2a) showed that complete removal of organics occurs at about 425°C. Still, there was a noticeable difference in the quality of the selenized films depending on the pre-anneal temperature. Figure 3.2 shows SEM images of selenized nanocrystal films that were annealed at 425°C, 475°C and 525°C prior to selenization at 500°C. The nanocrystal films heated to the highest pre-selenization temperature of 525°C

exhibited the most sintering and crystal grain growth during selenization (the sintered domains have a triangular morphology).

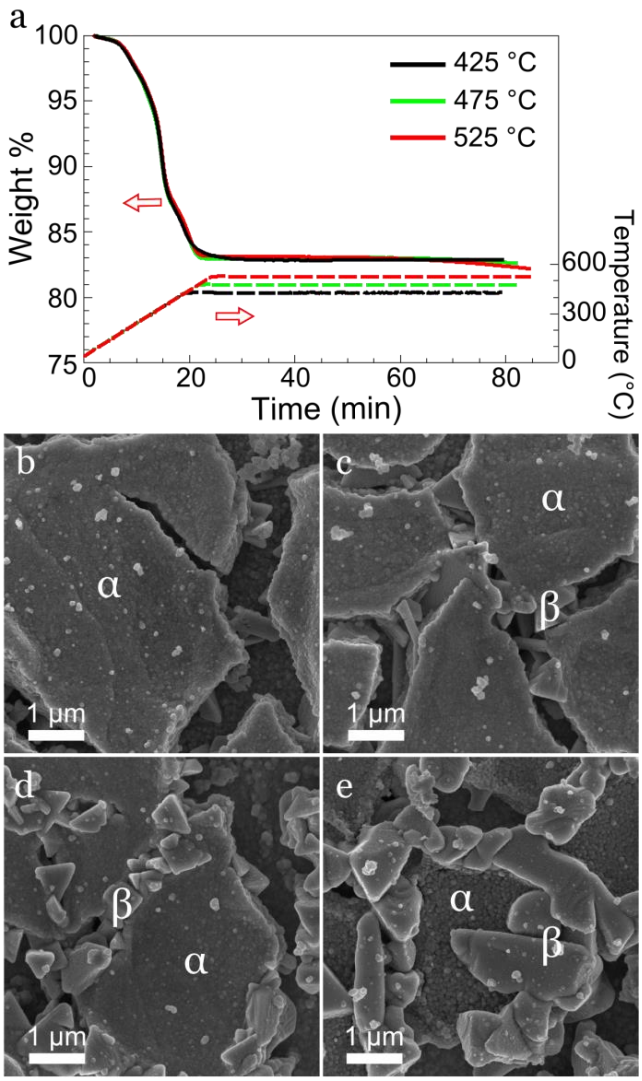

Figure 3.2 (a) Residual mass determined by TGA and the corresponding sample temperature profile. Samples were heated under nitrogen to final temperatures of 425°C, 475°C or 525°C. The TGA analysis was carried out under conditions similar to those used in the pre-selenization anneal. (b-e) SEM of the selenized nanocrystal layers (b) without a pre-selenization anneal and with pre-selenization anneals at (c) 425°C (d) 475°C (e) 525°C under Ar for one hour. The labels α and β indicate unsintered and sintered regions of the film, respectively.

Table 1 shows the performance of selenized CIGS nanocrystal PV devices—the pre-selenization temperature was found to significantly affect the device PCE. Films without a pre-selenization anneal did not exhibit any measurable short circuit current, whereas the pre-selenization at 525^{o}C led to devices with efficiency as high as 4.17%. The very poor device performance of the layers without the pre-selenization anneal resulted in part from the very short selenization time of only 10 min. For comparison, recently reported selenized $Cu_{0.82}In_{0.32}Ga_{0.68}Se_2$ nanocrystal devices with 5.1% efficiency were selenized for *one hour* at 500^{o}C.[23]

Table 3.1 Performance of PV devices fabricated using different pre-selenization anneal temperatures (1 hour heating under Ar) followed by a 10 min selenization at 500°C. Measurements were made with 100 mW/cm^2 AM1.5 illumination.

Pre-Selenization Anneal Temperature (°C)	**V_{oc} (V)**	**J_{sc} (mA/cm^2)**	**FF**	**PCE (%)**
No Anneal	0.00	0.00	0.00	0.00
425	0.14	3.33	0.27	0.08
475	0.36	7.19	0.33	0.82
525	0.53	17.88	0.44	4.17

Since TGA showed that the organic weight loss is similar for all three pre-selenization annealing temperatures in Table 1, the difference in device efficiency is not due to ligand removal. XPS (Figure 3.3) analysis of the Mo back contact after Mo-coated soda lime glass substrates were heated under Ar for 1 hr showed a considerable Na signal, which increased with increasing annealing temperature. Sodium is known to enhance CIGS crystal grain growth during selenization.[18,33,34] The most important

contribution of the pre-selenization anneal to achieving more effective selenization of CIGS nanocrystal films appears to be sodium addition from the underlying substrate. XPS of the nanocrystal layers on Mo after pre-selenization anneal, however, did not show any Na even after 5 minutes of Ar sputtering, implying that Na does not diffuse into the nanocrystal layer to a significant extent during the pre-selenization anneal (Figure 3.4). These data suggest that Na diffuses from the soda-lime glass to the Mo/CIS interface during the pre-selenization anneal. Figure 3.5 shows LBIC maps of PV devices made from selenized CIGS nanocrystal films with pre-selenization anneals at 525°C and 475 °C. There is significant inhomogeneity in both device layers, but the photoresponse of the active regions in the CIGS layer with the 525^{o}C pre-selenization anneal is significantly higher than in the CIGS layer with the 475^{o}C pre-selenization anneal, consistent with the much higher short circuit current and device efficiency (Table 1).

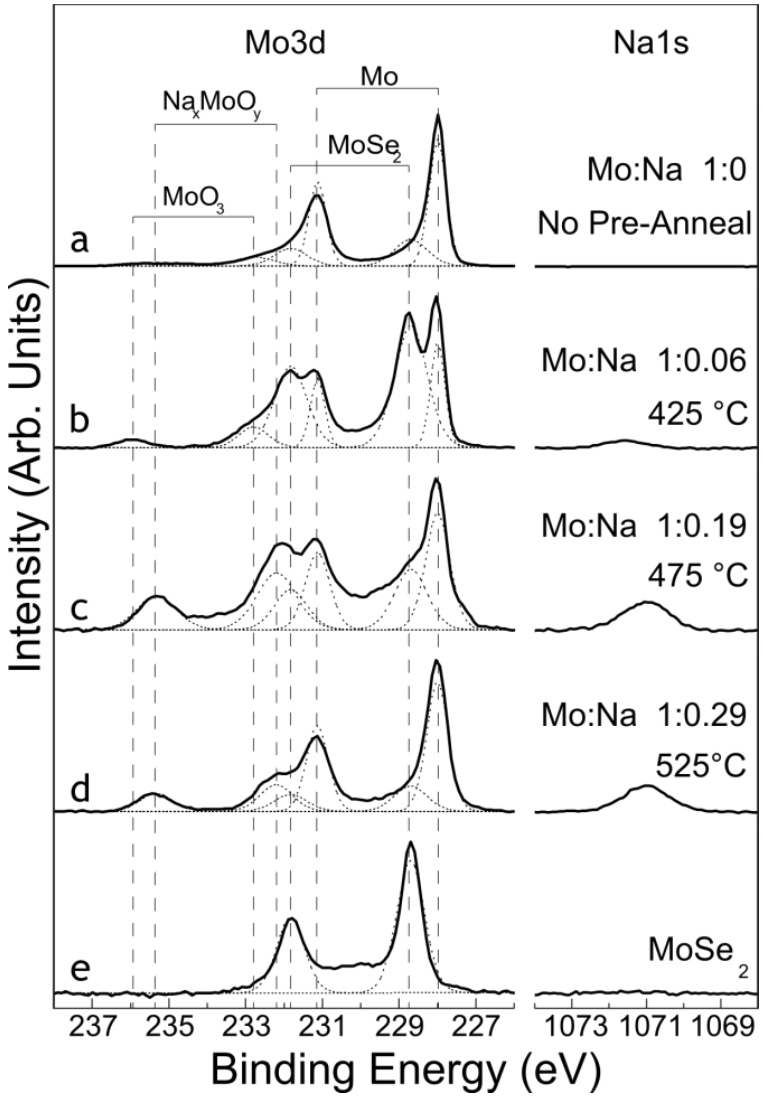

Figure 3.3 XPS data: Mo 3d and Na 1s regions measured from molybdenum-coated soda-lime glass (a) before and after annealing under Ar for 1 hr at (b) 425°C, (c) 475°C, (d) 525°C, and (e) selenized at 525°C. The Mo 3d region was fit by adding separate peak contributions from Mo^0, $MoSe_2$, MoO_3, and Na_xMoO_y for both $3d_{5/2}$ and $3d_{3/2}$ spin. Na 1s signal was normalized to the maximum intensity of the corresponding Mo 3d signal. The total integrated Mo 3d peak was used to normalize the Mo:Na response from sample to sample. $MoSe_2$ formation occurs from residual Se in the tube furnace. Additionally, some MoO_3 and Na_xMoO_y was detected due to oxidation of the Mo back contact.

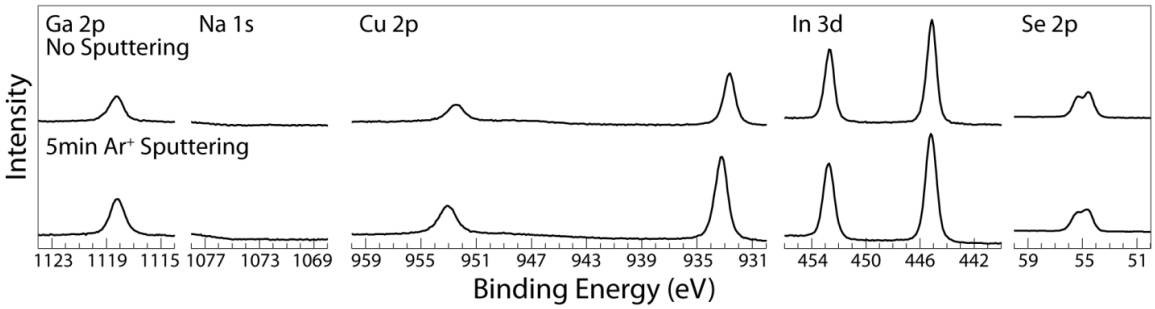

Figure 3.4 XPS of CIGS nanocrystal film on Mo substrate after pre-selenization anneal at 525°C for 1 hour. Spectra were collected before (top) and after (bottom) Ar^+ sputtering for 5 min.

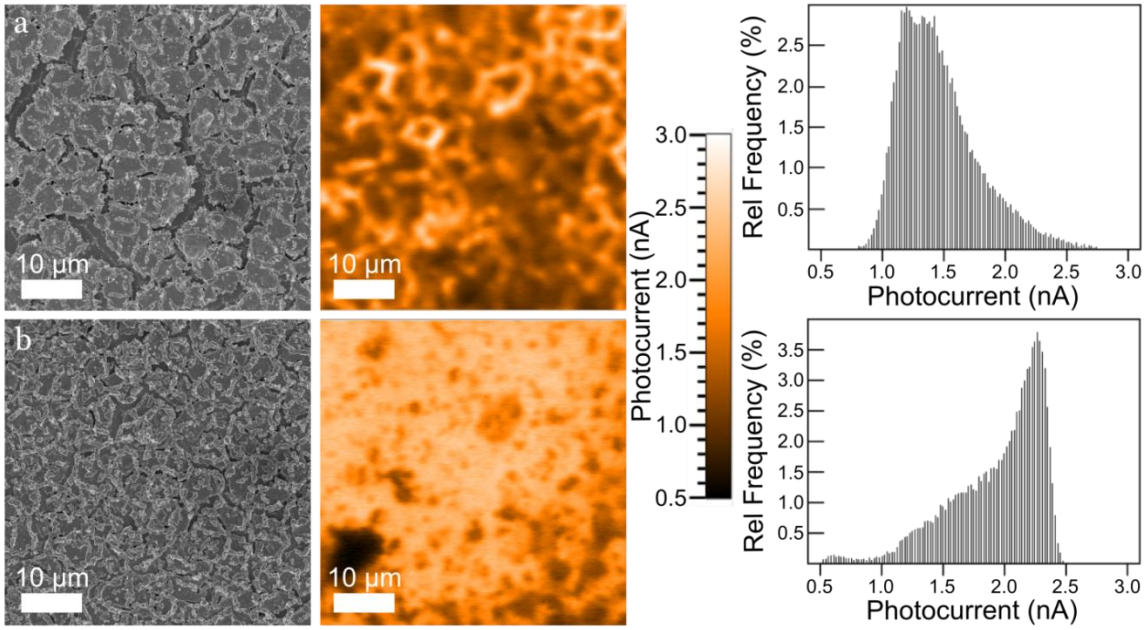

Figure 3.5 SEM image (left), LBIC map (middle), and photocurrent histogram (right) of PV devices made with selenized CIGS nanocrystals with a pre-selenization anneal under Ar for 1 hr at (a) 475°C and (b) 525°C. The CIGS layer with pre-selenization anneal at 525°C shows higher photocurrent.

The absence of sodium diffusion into the nanocrystal film during the pre-selenization anneal results in enhanced sintering of the nanocrystals only near the Mo back contact. Figure 3.6 shows SEM images of cross-sectioned selenized CIGS layers of varying thickness. The relatively thin CIGS nanocrystal layer (400 nm) does sinter uniformly throughout the entire film. However, the thicker 1.6 μm film sinters near the Mo substrate and towards the top of the film exposed to Se. There is a relatively thick inner region of nanocrystals that remain unsintered. Se does not seem to be able to penetrate deep into the nanocrystal film to promote sintering effectively, although the nanocrystals near the substrate where the Na concentration would be highest appear to sinter under these conditions. This is important because the 400 nm films are too thin to absorb a significant portion of the incident light. The highest efficiency devices made by co-evaporation have CIGS layers around 2 μm thick.[2] Strategies for uniform sintering of thicker CIGS nanocrystal layers are needed.

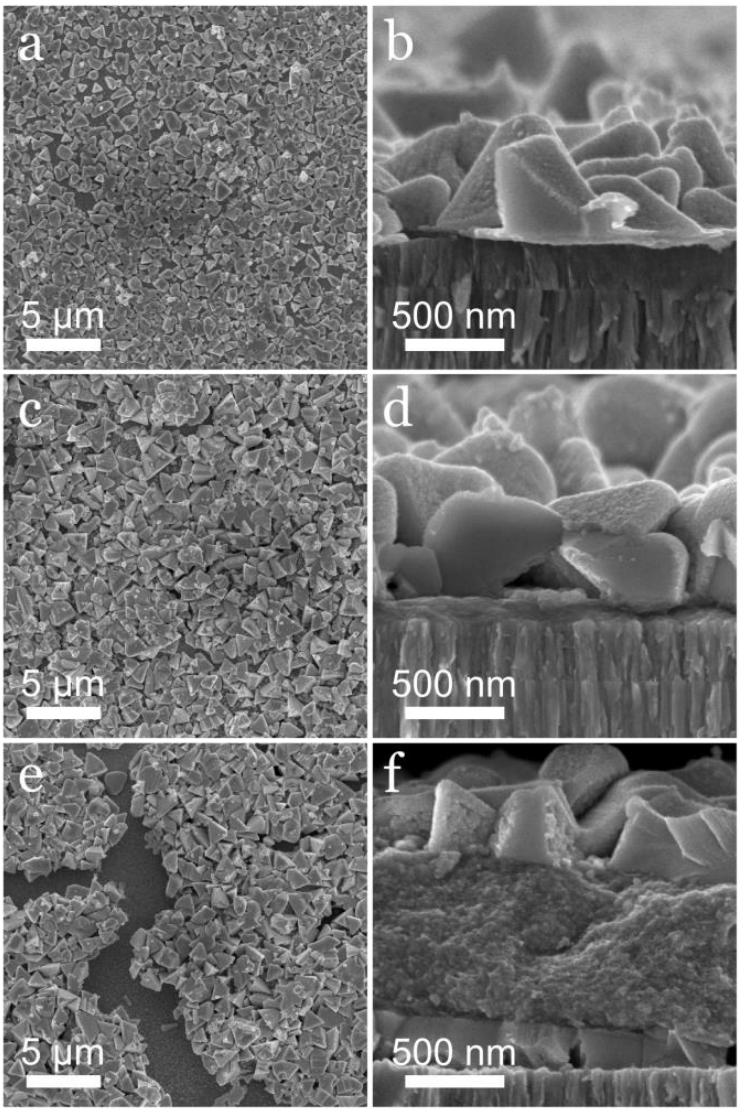

Figure 3.6 Top-view and cross-section SEM images of CIGS nanocrystal films selenized on Mo-coated soda lime glass substrates with different thickness: (a,b) 0.4 µm, (c,d) 0.8 µm, (e,f) 1.6 µm. All films were heated under Ar for 1 hr at 525°C prior to selenization for 10 min at 500°C.

One approach to sodium infusion into the CIGS nanocrystal film is to soak the layer in a NaCl bath as first reported by Guo, *et al*.[18] in their work to significantly improve device performance from selenized $Cu(In_xGa_{1-x})S_2$ nanocrystal films. We have found that a NaCl bath can also improve CIGS nanocrystal selenization. Figure 3.7

shows SEM and LBIC images of two CIGS nanocrystal films annealed at 475°C under Ar for 1 hr and then selenized at 500°C for 10 min. The nanocrystal device layer in Figure 3.7b was also soaked in aqueous 1 M NaCl for 10 min prior to selenization. The film with the NaCl bath treatment exhibited significantly higher photocurrent in the active device regions. The NaCl-soaked films also had some inactive regions that appear to result from residual NaCl.

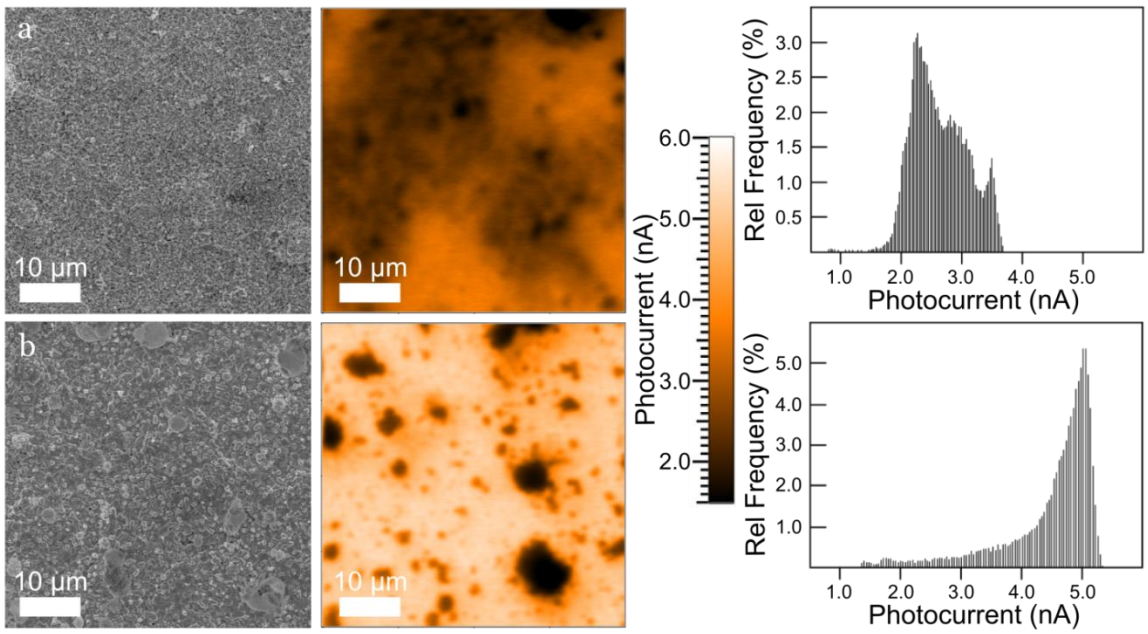

Figure 3.7 SEM image (left), LBIC map (middle), and photocurrent histogram (right) of devices (a) without and (b) with soaking for 10 min in aqueous 1 M NaCl. The nanocrystal films in (a) and (b) were annealed under Ar for 1 hr at 475°C prior to NaCl bath soaking and selenization for 10 min at 500°C.

We have found that limiting the selenization time is important for maintaining the integrity of the device. The Mo bottom contact reacts with Se to form $MoSe_2$ and some conversion of Mo to $MoSe_2$ is important to improve electrical contact with the CIGS film, but excess $MoSe_2$ formation leads to delamination of the CIGS layer. Mo

selenization occurs at temperatures as low as 350°C.[36] Figure 3.8 shows SEM images of cross-sectioned CIGS layers on Mo-coated glass substrates selenized for 10 min at 500°C with a 525°C pre-selenization anneal under Ar with two different heating rates. The extent of $MoSe_2$ formation is limited by minimizing the time in the 350-500°C temperature range—the thickness of the $MoSe_2$ layer was decreased by a factor of two when the heating ramp rate was increased from 20°C/min (Fig 3.8a) to 50°C/min (Fig 3.8b). Increasing the ramp rate further to 80°C/min, however, (Fig 3.8C) did not change the $MoSe_2$ thickness, consistent with the fact that the time spent in the 350-500°C temperature range (12 min vs. 13 min) was not significantly different.

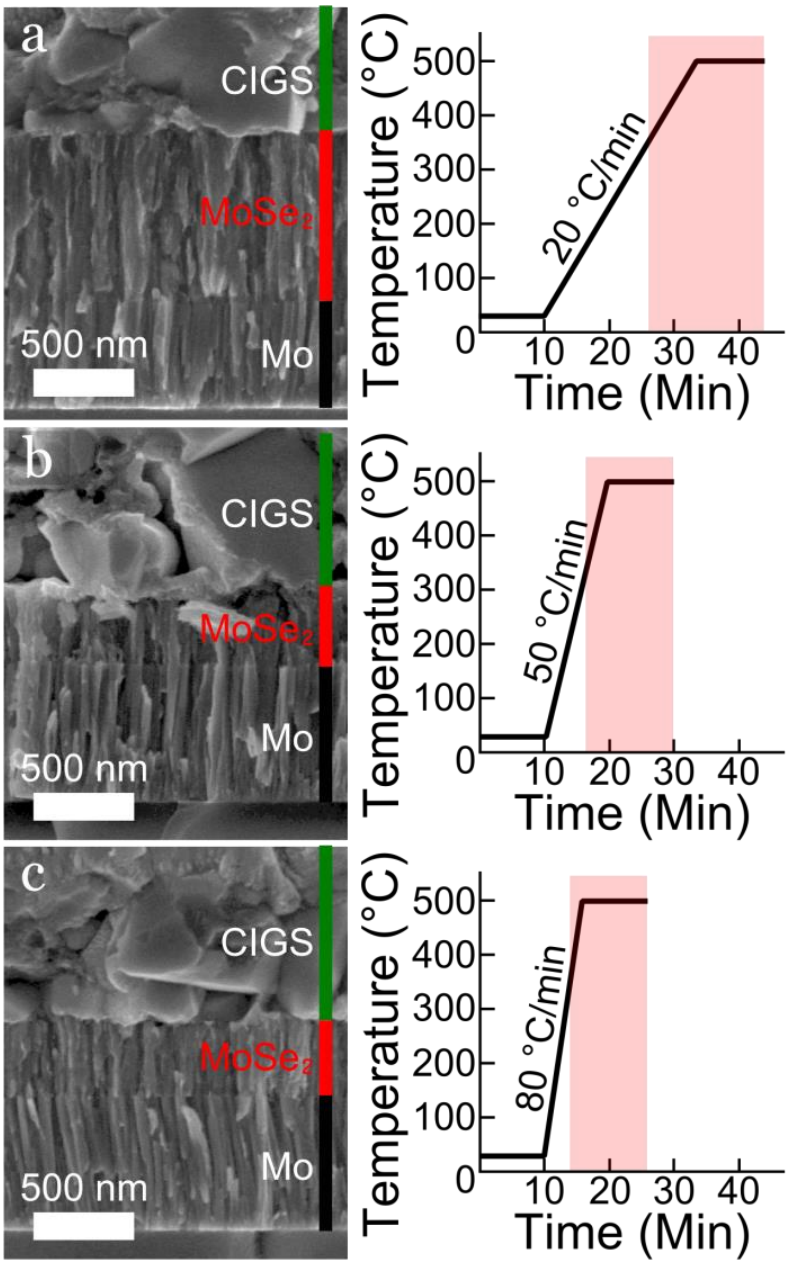

Figure 3.8 SEM images of cross-sectioned CIGS nanocrystal films on Mo-coated soda lime glass substrates after selenization at 500 °C for 10 min with temperature ramping of (a) 20 °C/min, (b) 50°C/min, and (c) 80°C/min. The temperature profile is shown on the right of each image. The temperature range between 350°C and 500°C is highlighted in pink.

As shown in Figure 3.6, CIGS nanocrystal films greater than about 800 nm thick do not completely sinter through the entire film. Unsintered portions in the film lead to poor device performance. For complete light absorption and the highest possible device efficiency, thicker selenized CIGS layers are needed. A further problem with devices made with only a single nanocrystal deposition and selenization step is that the selenized layer does not uniformly cover the substrate due to the formation of voids created during the crystallization of the nanocrystal film. An additional step of nanocrystal deposition can fill the voids in the film and build thicker layers, but the total selenization time must be limited because the film delaminates if too much $MoSe_2$ forms at the back contact. The use of 525^{o}C pre-selenization anneal, NaCl bath soak, and fast ramp rate to the selenization temperature allows the selenization time to be limited to 10 min and PVs can then be made with selenized CIGS nanocrystal films of up to 2 μm thick by repeating the deposition, pre-selenization anneal, and selenization process (as shown in Figure 3.9).

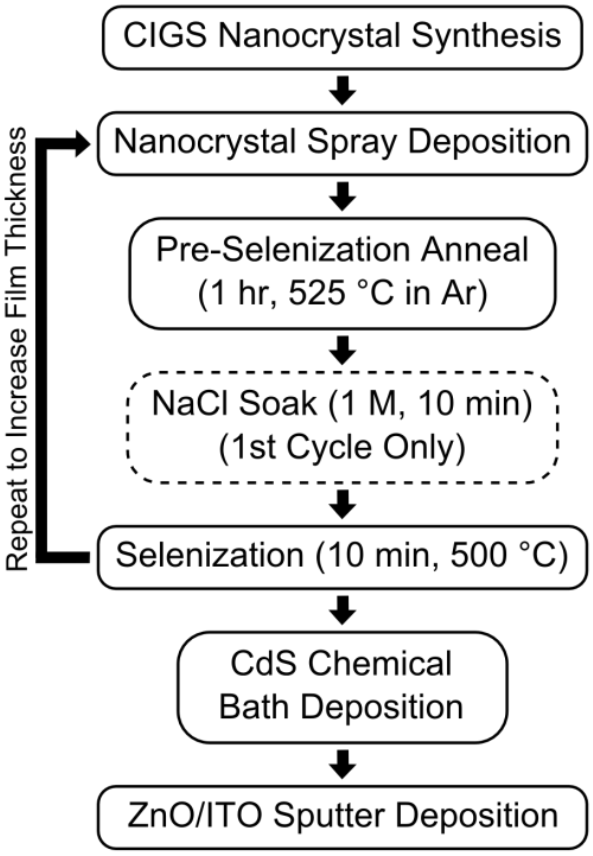

Figure 3.9 Process steps used to fabricate CIGS PVs with 2 μm CIGS absorber layers.

Figure 3.10 compares SEM images of selenized CIGS nanocrystal layers made with one, two or three cycles of nanocrystal deposition and selenization. The spatial coverage of the substrate becomes more uniform with multiple cycles of deposition and selenization. The average sintered grain size also increases with more deposition/selenization steps. Figure 3.11 shows device characteristics and SEM images of one of the best devices made using multiple deposition/sintering cycles. This device was made with 3 deposition/selenization cycles and had a sintered CIGS film thickness of about 2 μm with a PCE of 7.1%. Table 2 summarizes the performance of devices made

with one, two, or three repetitions of the deposition, pre-selenization anneal, selenization. A steady rise in PCE is observed as the film thickness was increased, mostly due to higher V_{oc} and FF; however, a small rise in J_{sc} is also seen. In Figure 3.10d, the maximum EQE rose when the device was made with two deposition/selenization cycles instead of one. The device EQE primarily increased at longer wavelengths when three cycles were used instead of two, indicating more light absorption from the thicker film but probably slightly decreased IQE. A decrease in the number of grain boundaries (Figure 3.11b) and improved film uniformity are expected to improve device performance further.

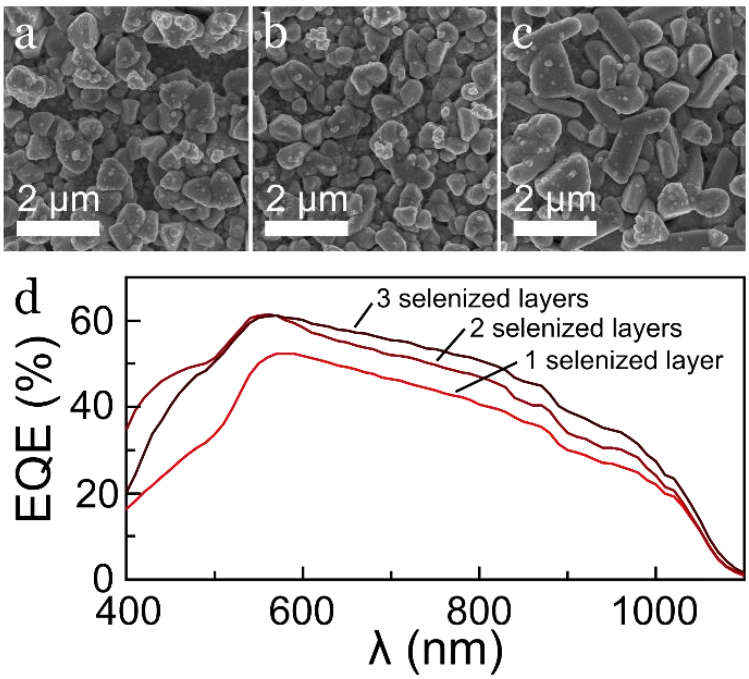

Figure 3.10 SEM images of selenized CIGS nanocrystal layers made with (a) one, (b)two or (c) three cycles of CIGS nanocrystal deposition, 525°C pre-selenization anneal in Ar for 1 hr, and a 10 minute selenization at 500°C. (d) EQE for devices made with the indicated number of deposition/selenization steps.

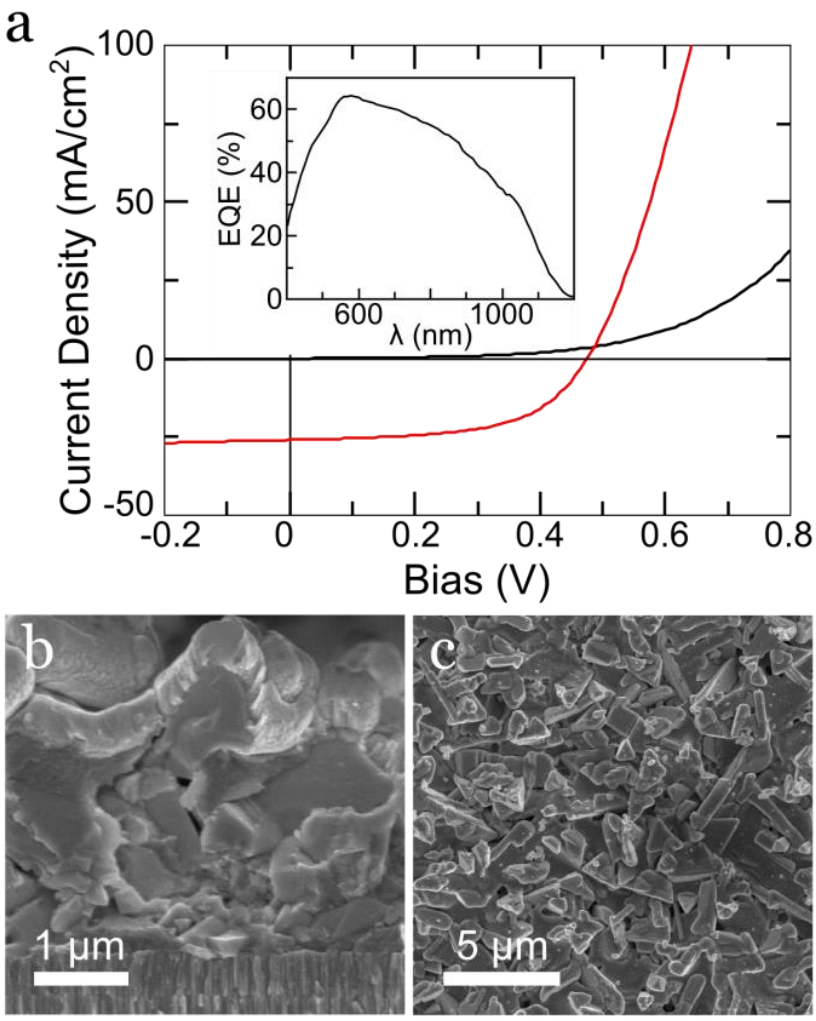

Figure 3.11 (a) PV device response for a selenized CIGS nanocrystal device with 7.1% power conversion efficiency under AM1.5 illumination (100 mW/cm^2). The device was made using three sequential nanocrystal deposition/selenization steps. The EQE is shown in the inset. (b) SEM image of a device cross-section showing that the sintered CIGS layer is more than 2 μm thick. (c) SEM of the CIGS layer from the top, showing relatively large sintered CIGS crystal grains.

Table 3.2 Performance of PV devices made using various cycles of CIGS nanocrystal deposition, 525°C pre-selenization anneal under Ar for 1 hr, and 10 min selenization at 500°C with a 10 min soak in aqueous 1 M NaCl after the first preselenization anneal. The "optimized" device was made by depositing thicker nanocrystal layers (~1 μm) during each cycle.

Number of Deposition/Selenization Cycles	V_{oc} (V)	J_{sc} (mA/cm^2)	FF	PCE (%)
1	0.43	20.5	0.37	3.26
2	0.47	21.8	0.42	4.32
3	0.51	22.1	0.49	5.01
3 (Optimized)	0.48	25.9	0.58	7.1

3.4 CONCLUSIONS

PV devices were fabricated with selenized $Cu(In_xGa_{1-x})Se_2$ nanocrystal films to achieve power conversion efficiency of up to 7.1%. These devices were made by three cycles of spray-deposition of CIGS nanocrystals followed by selenization. Multiple nanocrystal/selenization steps were enabled by the use of a high temperature pre-selenization anneal under inert atmosphere for 1 hr to remove capping ligands and drive sodium from the glass substrate to the Mo/nanocrystal interface prior to selenization at 500°C. This pre-selenization anneal made nanocrystal sintering during selenization occur much more rapidly than without it and a relatively short 10 min selenization time was needed to sinter the nanocrystals compared to a typical selenization time of 1 hr. The use of a NaCl bath soak of the nanocrystal films was also found to help improve sintering uniformity in thicker nanocrystal layers.

3.5 ACKNOWLEDGEMENTS

Financial support of this work was provided by the Robert A. Welch Foundation (F-1464) and the National Science Foundation Industry/University Cooperative Research Center on Next Generation Photovoltaics (IIP-1134849). IM acknowledges support by the "Nanotechnology Platform" of the Ministry of Education, Culture, Sports, Science and Technology(MEXT), Japan. CJS acknowledges support from the National Science Foundation Graduate Research Fellowship under Grant No. DGE-1110007. TDB acknowledges support from the Department of Defense (DoD) through the National Defense Science & Engineering Graduate Fellowship (NDSEG) Program. HK performed this research as part of a student exchange agreement between The University of Texas at Austin and the Ecole Centrale de Lille, France.

3.6 REFERENCES

(1) Jackson, P.; Hariskos, D.; Lotter, E.; Paetel, S.; Wuerz, R.; Menner, R.; Wischmann, W.; Powalla, M. New World Record Efficiency for Cu(In,Ga)Se2 Thin-Film Solar Cells beyond 20%. *Progress in Photovoltaics: Research and Applications* **2011**, *19*, 894–897.

(2) Repins, I.; Contreras, M. A.; Egaas, B.; DeHart, C.; Scharf, J.; Perkins, C. L.; To, B.; Noufi, R. 19·9%-Efficient ZnO/CdS/CuInGaSe2 Solar Cell with 81·2% Fill Factor. *Progress in Photovoltaics: Research and Applications* **2008**, *16*, 235–239.

(3) Kessler, J.; Wennerberg, J.; Bodegård, M.; Stolt, L. Highly Efficient Cu(In,Ga)Se2 Mini-Modules. *Solar Energy Materials and Solar Cells* **2003**, *75*, 35–46.

(4) Wallin, E.; Malm, U.; Jarmar, T.; Edoff, Olle Lundberg, M.; Stolt, L. World-Record Cu(In,Ga)Se2-Based Thin-Film Sub-Module with 17.4% Efficiency. *Progress in Photovoltaics: Research and Applications* **2012**, *20*, 851–854.

(5) Goushi, Y.; Hakuma, H.; Tabuchi, K.; Kijima, S.; Kushiya, K. Fabrication of Pentanary Cu(InGa)(SeS)2 Absorbers by Selenization and Sulfurization. *Solar Energy Materials and Solar Cells* **2009**, *93*, 1318–1320.

(6) Voorwinden, G.; Kniese, R.; Powalla, M. In-Line Cu(In,Ga)Se2 Co-Evaporation Processes with Graded Band Gaps on Large Substrates. *Thin Solid Films* **2003**, *431–432*, 538–542.

(7) Powalla, M.; Voorwinden, G.; Hariskos, D.; Jackson, P.; Kniese, R. Highly Efficient CIS Solar Cells and Modules Made by the Co-Evaporation Process. *Thin Solid Films* **2009**, *517*, 2111–2114.

(8) Zweibel, K. Issues in Thin Film PV Manufacturing Cost Reduction. *Solar Energy Materials and Solar Cells* **1999**, *59*, 1–18.

(9) Liehr, M. Challenges for Vacuum Systems Manufacturers in the PV Industry. In *Workshop Proceedings of the 3rd International Workshop. Thin Films in the Photovoltaic Industry*; Ispra, Italy, 2007.

(10) Wilkommen, U.; Diemer, M. Thin Film Photovoltaic Production Technology. In *Workshop Proceedings of the 3rd International Workshop. Thin Films in the Photovoltaic Industry*; Ispra, Italy, 2007.

(11) Bauer, G. H.; Gütay, L.; Kniese, R. Structural Properties and Quality of the Photoexcited State in Cu(In1−xGax)Se2 Solar Cell Absorbers with Lateral Submicron Resolution. *Thin Solid Films* **2005**, *480–481*, 259–263.

(12) Karg, F. High Efficiency CIGS Solar Modules. *Energy Procedia* **2012**, *15*, 275–282.

(13) Panthani, M. G.; Akhavan, V.; Goodfellow, B.; Schmidtke, J. P.; Dunn, L.; Dodabalapur, A.; Barbara, P. F.; Korgel, B. A. Synthesis of CuInS2, CuInSe2, and Cu(InxGa1-x)Se2 (CIGS) Nanocrystal "Inks" for Printable Photovoltaics. *Journal of the American Chemical Society* **2008**, *130*, 16770–16777.

(14) Akhavan, V. A.; Panthani, M. G.; Goodfellow, B. W.; Reid, D. K.; Korgel, B. A. Thickness-Limited Performance of CuInSe2 Nanocrystal Photovoltaic Devices. *Opt. Express* **2010**, *18*, A411–A420.

(15) Akhavan, V. A.; Goodfellow, B. W.; Panthani, M. G.; Reid, D. K.; Hellebusch, D. J.; Adachi, T.; Korgel, B. A. Spray-Deposited CuInSe2 Nanocrystal Photovoltaics. *Energy Environ. Sci.* **2010**, *3*, 1600.

(16) Stolle, C. J.; Panthani, M. G.; Harvey, T. B.; Akhavan, V. A.; Korgel, B. A. Comparison of the Photovoltaic Response of Oleylamine and Inorganic Ligand-Capped CuInSe2 Nanocrystals. *ACS Appl. Mater. Interfaces* **2012**, *4*, 2757–2761.

(17) Guo, Q.; Ford, G. M.; Hillhouse, H. W.; Agrawal, R. Sulfide Nanocrystal Inks for Dense Cu(In1−xGax)(S1−ySey)2 Absorber Films and Their Photovoltaic Performance. *Nano Letters* **2009**, *9*, 3060–3065.

(18) Guo, Q.; Ford, G. M.; Agrawal, R.; Hillhouse, H. W. Ink Formulation and Low-Temperature Incorporation of Sodium to Yield 12% Efficient Cu(In,Ga)(S,Se)2

Solar Cells from Sulfide Nanocrystal Inks. *Progress in Photovoltaics: Research and Applications* **2013**, *21*, 64–71.

(19) Stolle, C. J.; Harvey, T. B.; Korgel, B. A. Nanocrystal Photovoltaics: A Review of Recent Progress. *Current Opinion in Chemical Engineering* **2013**, *2*, 160–167.

(20) Eberspacher, C.; Fredric, C.; Pauls and Jack Serra, K. Thin-Film CIS Alloy PV Materials Fabricated Using Non-Vacuum, Particles-Based Techniques. *Thin Solid Films* **2001**, *387*, 18–22.

(21) Kapur, V. K.; Bansal, A.; Le, P.; Asensio, O. I. Non-Vacuum Processing of CuIn1−xGaxSe2 Solar Cells on Rigid and Flexible Substrates Using Nanoparticle Precursor Inks. *Thin Solid Films* **2003**, *431–432*, 53–57.

(22) Kaelin, M.; Rudmann, D.; Kurdesau, F.; Zogg, H.; Meyer, T.; Tiwari, A. N. Low-Cost CIGS Solar Cells by Paste Coating and Selenization. *Thin Solid Films* **2005**, *480–481*, 486–490.

(23) Akhavan, V. A.; Harvey, T. B.; Stolle, C. J.; Ostrowski, D. P.; Glaz, M. S.; Goodfellow, B. W.; Panthani, M. G.; Reid, D. K.; Vanden Bout, D. A.; Korgel, B. A. Influence of Composition on the Performance of Sintered Cu(In,Ga)Se2 Nanocrystal Thin-Film Photovoltaic Devices. *ChemSusChem* **2013**, *6*, 481–486.

(24) Jeong, S.; Lee, B.-S.; Ahn, S.; Yoon, K.; Seo, Y.-H.; Choi, Y.; Ryu, B.-H. An 8.2% Efficient Solution-Processed CuInSe2 Solar Cell Based on Multiphase CuInSe2 Nanoparticles. *Energy Environ. Sci.* **2012**, *5*, 7539–7542.

(25) Cho, A.; Ahn, S.; Yun, J. H.; Gwak, J.; Song, H.; Yoon, K. A Hybrid Ink of Binary Copper Sulfide Nanoparticles and Indium Precursor Solution for a Dense CuInSe2 Absorber Thin Film and Its Photovoltaic Performance. *J. Mater. Chem.* **2012**, *22*, 17893–17899.

(26) Todorov, T. K.; Gunawan, O.; Gokmen, T.; Mitzi, D. B. Solution-Processed Cu(In,Ga)(S,Se)2 Absorber Yielding a 15.2% Efficient Solar Cell. *Progress in Photovoltaics: Research and Applications* **2013**, *21*, 82–87.

(27) Mitzi, D. B.; Yuan, M.; Liu, W.; Kellock, A. J.; Chey, S. J.; Deline, V.; Schrott, A. G. A High-Efficiency Solution-Deposited Thin-Film Photovoltaic Device. *Advanced Materials* **2008**, *20*, 3657–3662.

(28) Liu, W.; Mitzi, D. B.; Yuan, M.; Kellock, A. J.; Chey, S. J.; Gunawan, O. 12% Efficiency CuIn(Se,S)2 Photovoltaic Device Prepared Using a Hydrazine Solution Process†. *Chem. Mater.* **2010**, *22*, 1010–1014.

(29) Lee, E.; Park, S. J.; Cho, J. W.; Gwak, J.; Oh, M.-K.; Min, B. K. Nearly Carbon-Free Printable CIGS Thin Films for Solar Cell Applications. *Solar Energy Materials and Solar Cells* **2011**, *95*, 2928–2932.

(30) Kind, C.; Feldmann, C.; Quintilla, A.; Ahlswede, E. Citrate-Capped Cu11In9 Nanoparticles and Its Use for Thin-Film Manufacturing of CIS Solar Cells. *Chem. Mater.* **2011**, *23*, 5269–5274.

(31) Wang, G.; Wang, S.; Cui, Y.; Pan, D. A Novel and Versatile Strategy to Prepare Metal–Organic Molecular Precursor Solutions and Its Application in Cu(In,Ga)(S,Se)2 Solar Cells. *Chem. Mater.* **2012**, *24*, 3993–3997.

(32) Cai, Y.; Ho, J. C. W.; Batabyal, S. K.; Liu, W.; Sun, Y.; Mhaisalkar, S. G.; Wong, L. H. Nanoparticle-Induced Grain Growth of Carbon-Free Solution-Processed CuIn(S,Se)2 Solar Cell with 6% Efficiency. *ACS Appl. Mater. Interfaces* **2013**, *5*, 1533–1537.

(33) Probst, V.; Karg, F.; Rimmasch, J.; Riedl, W.; Stetter, W.; Harms, H.; Eibl, O. Advanced Stacked Elemental Layer Process for Cu(InGa)Se2 Thin Film Photovoltaic Devices. *MRS Proceedings* **1996**, *426*, null – null.

(34) Rau, U.; Schock, H. W. Electronic Properties of Cu(In,Ga)Se2 Heterojunction Solar Cells–recent Achievements, Current Understanding, and Future Challenges. *Appl Phys A* **1999**, *69*, 131–147.

(35) Ostrowski, D. P.; Glaz, M. S.; Goodfellow, B. W.; Akhavan, V. A.; Panthani, M. G.; Korgel, B. A.; Vanden Bout, D. A. Mapping Spatial Heterogeneity in Cu(In1−xGax)Se2 Nanocrystal-Based Photovoltaics with Scanning Photocurrent and Fluorescence Microscopy. *Small* **2010**, *6*, 2832–2836.

(36) Koo, J.; Jeon, S.; Oh, M.; Cho, H.; Son, C.; Kim, W. K. Optimization of Se Layer Thickness in Mo/CuGa/In/Se Precursor for the Formation of Cu(InGa)Se2 by Rapid Thermal Annealing. *Thin Solid Films*.

Chapter 4: Photovoltaics from Automated, Ultra-Sonic Spray-Deposited $Cu(In,Ga)Se_2$ Nanocrystal Films

4.1 Introduction

Direct conversion of sunlight to electricity using photovoltaics (PVs) has the potential to be a source of energy that is both cost effective and clean. The promise of solar power is predicated on the ability to manufacture solar cells in a manner that enables solar energy generation at a lower cost than fossil fuel derived power sources. Silicon based solar cells are close to achieving this metric in some geographical locations;[1,2] however, lower fabrication cost is needed for this to become universally true.

One possible route to lower cost photovoltaics is to reduce the reliance of the PV manufacturing process on vacuum processing through solution processing of the absorber layer. Photovoltaics fabricated from solution processes have demonstrated large improvements in power conversion efficiency (PCE).[3] The highest efficiency inorganic solution processed devices have used thin films fabricated using Copper Indium Gallium Selenide (CIGS).[4,5] In general, a solution with either all or a partial combination of Cu, In, Ga, Se precursors is deposited on a Mo substrate, followed by an annealing treatment, generally under a Se atmosphere (known as selenization). Many precursor solutions have been explored, including molecular precursors dissolved in hydrazine,[4] and organic solvents,[6–8] nanocrystals of $CuInGaS_2$,[9,10] $CuInGaSe_2$,[11,12] Cu_9In_{11},[13] and molecular/nanocrystal mixtures.[14,15] Spin coating,[4,8,15] blade coating,[6,7,9,13] printing,[10] and spray coating[11,14] are used to deposit the films and, in many cases, a layer-by-layer deposition approach is used.[4,9–11,14,15] Some of these deposition methods are not amenable to scale up (primarily spin coating), and the use of a layer-by-layer approach increases fabrication complexity. A simple, single layer, scalable method is still needed.

Additionally, as scale increases, the manufacturing yield (the percentage of usable product compared to fabricated product) and efficiency of commercial CIGS photovoltaics has suffered.[16] This is primarily due to the increase of point defects and compositional gradients[17] in the films. Spray deposition of nanocrystals can potentially improve the spatial composition uniformity of the final film by using a uniform composition nanocrystal. $Cu(In,Ga)Se_2$ nanocrystals in particular offer the clearest path to homogenous composition by allowing the composition to be tuned completely before large scale deposition,[18] and have not required toxic chemical treatments to control composition before (dissolution of S and Se in hydrazine)[4] or after (KCN etching)[9,13] selenization.

Here we demonstrate a scalable, single layer, spray deposition of CIGS nanocrystal ink using a fully automated ultrasonic spray nozzle. Utilizing this technology leads to finer control in the fabrication process, but increases manufacturing sensitivity to relatively small changes in processing. In particular, we find that the formulation of the nanocrystal ink is highly influential in the fabrication process. Small changes in organic content from the nanocrystal capping ligand lead to large differences in film morphology that influence the final film performance. We also explore different selenization conditions to completely convert nanocrystals to large CIGS grains. Higher selenization temperatures are favored in thicker films, but were harmful for thinner devices. Optimization of the nanocrystal preparation, deposition morphology and thickness, and selenization temperature leads to devices with efficiencies as high as 6.6% with a single deposition layer of CIGS nanocrystals.

4.2 Experimental Details

4.2.1 Materials

Elemental selenium powder (99.99%), copper(I) chloride (99.99+%), and cadmium(II) sulfate (99.999%) were purchased from Aldrich Chemical Co.; Ethanol (absolute), toluene (99.99%), and ammonium hydroxide (18 M; ACS certified) from Fisher Scientific; and thiourea (>99.0%), sodium dodecanoate (99-100%) and sodium oleate (≥99%) from Sigma-Aldrich. gallium(III) chloride (99.999%) and indium(III) chloride (99.999%) were received from 5N plus; Oleylamine (>70%) was received from TCI America and degassed overnight at 110 °C under vacuum. Other chemicals were used as received.

4.2.2 Nanocrystal Synthesis

Previously published procedures were used to synthesize CIGS nanocrystals.[11,18] A targeted composition of $CuIn_{0.65}Ga_{0.35}Se_2$ was obtained by combining 40 mL of degassed oleylamine (OLA), 4 mmol of CuCl, 2.6 mmol of $InCl_3$, 1.4 mmol of $GaCl_3$ and 8 mmol of Se in a three-neck flask in a N_2-filled glovebox. The reaction flask was sealed, removed from the glovebox, attached to a standard Schlenk line, and degassed for 30 minutes at 110 °C. After blanketing the mixture with nitrogen, the temperature was increased to 240 °C for 30 minutes. The heating mantel was then removed and the reaction was cooled to room temperature.

After cooling, the particles were washed via centrifugation at 4000 rpm for 2 min using ethanol and toluene as anti-solvent and solvent, respectively. The reaction product was precipitated using between 1.4-2.0 mL of ethanol/mg of reaction product. The precipitate was redispersed in 10 mL of toluene and centrifuged. 10 mL of ethanol is

added to the supernatant and the mixture is then spun again. Finally, toluene was added to the final precipitate to reach a final concentration between 5-15 mg/mL.

4.2.3 PV Device Fabrication

Soda-lime glass (Delta Technology) was cleaned by sonication in an acetone/isopropanol mixture, then in deionized (DI) water and dried with nitrogen. One micron Mo substrates were prepared by rf sputtering from a Mo target (Lesker, 99.95%) in two steps. A 400 nm adhesive layer is deposited at 5 mtorr followed by a highly conductive layer at 1.5 mtorr.

CIGS nanocrystal inks were spray-deposited on Mo-coated glass using a Sono-Tek ExactaCoat ultrasonic automated spray system. Typical spray depositions used an ink with a 10 mg/mL nanocrystal concentration, a liquid flow rate of 0.275 ml/min, and an air pressure of 2.6 psi. The substrate was heated on a hot-plate during the spraying process at 100 °C. The nozzle was rastered at a distance of 11.5 cm from the sample to deposit over a rectangular area using a standard pattern with 3 mm raster spacing and a raster speed of 14 mm/s.

The nanocrsystal thin films were then annealed under Ar at 525 °C for 1 h to remove organic ligands in a Thermolyne 79500 tube furnace, and then soaked in 1M NaCl solution for 10 minutes. Films were then sintered by annealing under Se environment (selenization). In a nitrogen-filled glovebox, the substrates were placed in a hollow graphite cylinder above a quartz boat of elemental selenium. The cylinder was capped firmly, placed in the tube furnace, and heated at 80 °C/min to 500°C for 10 minutes.

A 50 nm layer of CdS was deposited by chemical bath deposition (CBD).[19] A 300 mL crystallization dish is filled with 160 mL of DI water and heated to 80 °C, and 25 mL

Cadmium Sulfate (15mM), 12.5 mL thiourea (1.5 M), and 32 mL of ammonium hydroxide (28% by weight) are added. The devices are then submerged for 15 minutes, removed from the bath, rinsed with DI water and dried with nitrogen. To complete the device, 50 nm of ZnO (99.9%, Lesker) and 600 nm indium tin oxide (ITO, 99.99%, Lesker) were sputter-deposited at 2 mtorr through physical shadow masks to create an active area of 10 mm^2. Front contact lateral conductivity was improved by adding silver paint grids. The completed devices were baked for 2 h at 225 °C in an ambient atmosphere to improve performance.

4.2.4 Materials and Device Charactrization

A Keithley 2400 source meter was used to collect current-potential (IV) characteristics. Device characteristics were collected in the dark and under AM1.5G light from a Newport 91160 solar simulator tuned to 100 mW/cm^2 using a NIST calibrated Si photodiode (Hamamatsu, S1787-08). External quantum efficiency (EQE) measurements were taken as previously described.[11] Scanning electron microscope (SEM) images were collected using a Zeiss microscope operating at 5 kV. SEM images of films before selenization were taken using films deposited on Si.

4.3 Results and Discussion

CIGS nanocrystal inks are synthesized with a $Cu_{0.78}In_{0.63}Ga_{0.25}Se_2$ composition, similar to our past reports.[11,12] The inks are then deposited using a fully automatic Sono-Tek ExactaCoat ultrasonic spray deposition system with a 3-axis robotic arm rather than a handheld pressure spray gun. A wide parameter space was tested to determine the influence of ink concentration, air pressure, liquid flow rate, raster line spacing, raster speed, and nozzle height on the film morphology. Within a moderate range around the optimized spray parameters, the effect of changing these spray parameters can be broadly

grouped into two sets: 1) little or no change in film morphology is observed and 2) moderate change is observed in film morphology.

Changes in air pressure, raster line spacing, or raster speed lead to little or no change in the film morphology. The driving spray force for ultrasonic spray deposition stems from the liquid flow rate, but the liquid droplets are delivered using a low pressure air shaper. Spatial SEM are shown in Figure 4.1a-c for films deposited with 1.6 psi, 2.0 psi, and 2.4 psi showing minimal to no changes in film morphology. This result was typical when changing parameters in this group.

Moderate changes were observed in the film morphology when the liquid delivery rate of nanocrystal ink to the substrate surface was modified. Changes in direct liquid flow rate, ink concentration, and nozzle height change the liquid delivery rate and had similar effect on film morphology. Low liquid flow rate leads to some thickness patching laterally across the film. This is shown in Figure 4.1 when the ink concentration is increased from 5 mg/mL (Fig 4.1d) to 10 mg/mL (Fig 4.1e), leading to a moderately more uniform film. As the liquid delivery rate is increased further, web-like thick regions development around slightly thinner areas. This is shown in Fig 4.1f when the ink concentration is increased to 15 mg/mL.

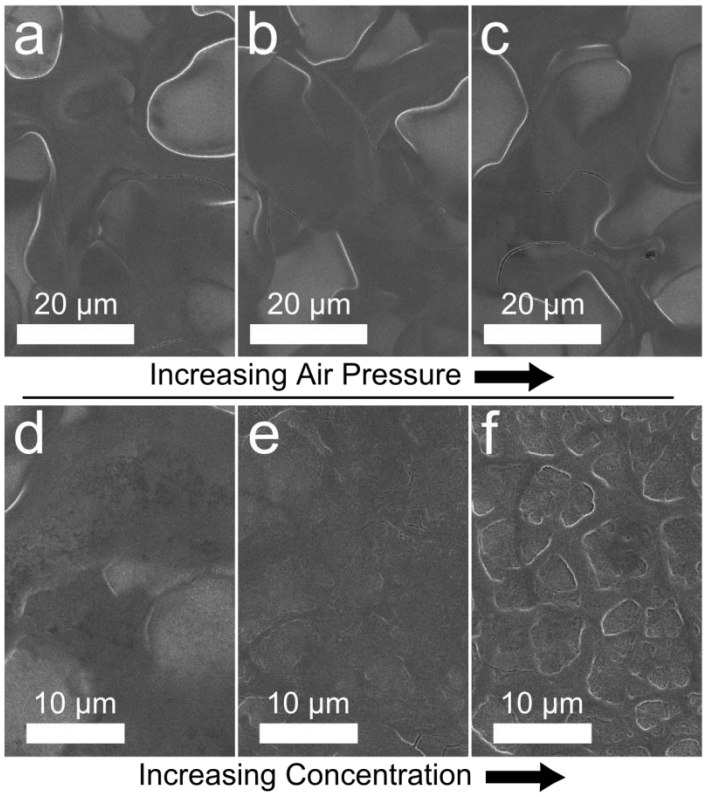

Figure 4.1 Spatial SEM of films after ultrasonic spray deposition with varying (a-c) air pressure and (d-f) ink concentration. Little are no change in film morphology is observed with an air pressure of a) 1.6 psi, b) 2.0 psi, and c) 2.6 psi. Moderate film morphology changes are observed when increasing the ink concentration from d)5 mg/mL to e)10 mg/mL and f)15 mg/mL with similar film thicknesses.

While changes in the direct spray deposition parameters did not lead to large changes in film morphology, the ink formulation itself has a significant effect on the film and devices. The primary factor influencing the film morphology is the organic content of the nanocrystal ink. Oleylamine (OLA) is used as a solvent during the nanocrystal synthesis and it remains attached to the nanocrystal surface as the capping ligand. As it was previously reported,[12] residual OLA in the ink lead to the formation of a carbon layer which reduced the device efficiency. However, OLA content also plays an important role during the spray step of the device fabrication.

An anti-solvent/solvent wash procedure is widely used in nanocrystal synthesis.[20,21] Figure 4.2a shows a schematic of a typical nanocrystal wash procedure. The reaction product is first precipitated from the reaction mixture using an anti-solvent. The precipitate is then redispersed in the solvent, followed by centrifugation to precipitate and remove the poorly capped particles from the solution. Organics are further removed from the mixture in a final washing step by precipitating the nanocrystals again with the anti-solvent. The final nanocrystal ink is prepared by redispersing the nanocrystals in a small amount of solvent. While the anti-solvent primarily removes unattached organics from the mixture, some ligand is removed from the nanocrystal surface. Toluene and ethanol are used in our wash procedure as solvent and anti-solvent, respectively.

After ultrasonic spray deposition (Fig 4.2b), two film morphologies are observed depending on the amount of anti-solvent added to precipitate the reaction mixture. When nanocrystals were precipitated with more than 1.8 mL of anti-solvent per mg of reaction product, the film was highly cracked (Fig 4.2c), leading to a visibly matte film. When less anti-solvent was used, the resulting film is a very smooth and visibly reflective film (Fig 4.2d). The amount of toluene and ethanol added during the separation and wash steps are held constant. Changing the amount of toluene and ethanol during the latter steps when the precipitation step is held constant does not lead to changes in film morphology. As will be discussed further, the amount of cracking has a direct influence on the selenization and device performance.

Thermogravimetric analysis (TGA) was used to determine the amount of organic content in the ink when different amounts of anti-solvent are added during the precipitation step (Figure 4.3). Nanocrystal inks formulated by precipitating with 1.8 mL or more of anti-solvent/mg of reaction product had 12% organic content. The organic

content increased as smaller amounts of ethanol were used, with an organic content percentage of 14% and 18% when 20% less and 40% less anti-solvent is used, respectively. The TGA response of the specific OLA used during the nanocrystal synthesis is shown in the inset of Figure 4.3. The weight loss from the nanocrystals corresponds directly with the onset of OLA evaporation. Due to the relatively small changes in added ethanol, the sensitivity of the spray deposition to anti-solvent used in the precipitation step makes control of the washing procedure highly important.

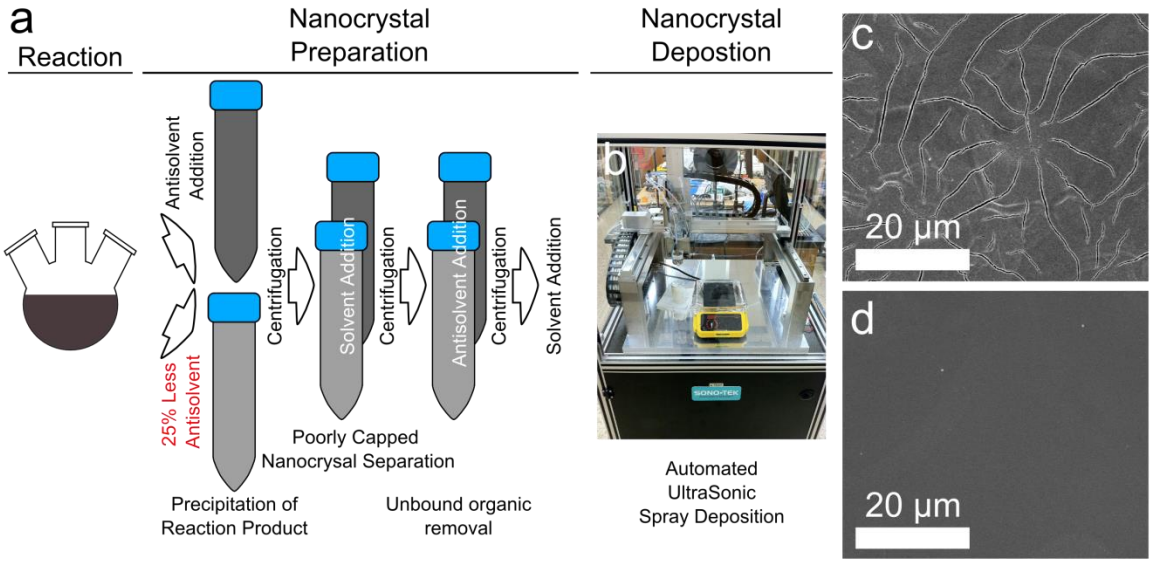

Figure 4.2 a) Schematic of the nanocrystal wash procedure. The reaction product is precipitated using an anti-solvent. The precipitate is redispersed in toluene and poorly capped particels are then precipitated via centrifugation. A final wash step is conducted to remove unbound organics by adding anti-solvent and precipitating the nanocrystals. The final ink is prepared by then redispersing the nanocrystals in a solvent. b) Picture of the Sono-Tek ExactaCoat system used for ultrasonic spray deposition of the nanocrystals. SEM of films precipitated with a c)typical amount of anti-solvent and d)25% less anti-solvent. The same solvent and anti-solvent additions were used for all other washing steps.

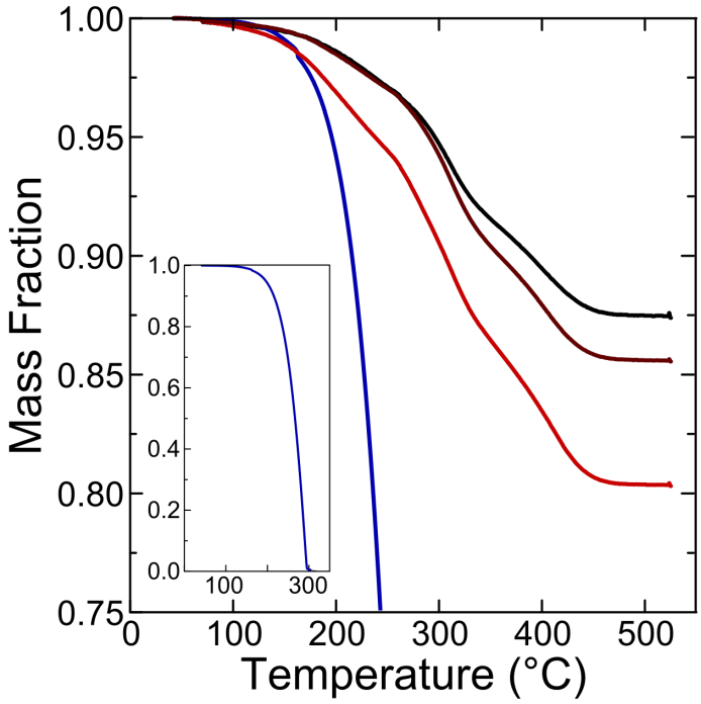

Figure 4.3 TGA of nanocrystals precipitated with typical (black line), 20% more (brown line), and 40% more (red line) anti-solvent. TGA of the pure OLA (blue line, full curve inset) is shown to verify that the change of mass fraction can be attributed to OLA.

Adding additional OLA to the final nanocrystal ink was tested as an alternative approach to minimize the film sensitivity to the precipitation step. Films were precipitated with excess ethanol (> 2 mL/mg reaction product), washed and then diluted to 10 mg/mL. Small quantities of OLA were then added to increase the organic content of the final ink formulation. Spray deposited films exhibited significant cracking when no OLA was added to the ink (Fig. 4.4a). A small addition (0.27% by volume) of OLA decreased cracking, but large cracks are still present throughout the film (Fig 4.4b).

Further OLA addition (0.54%) lead to crack-free films, but large organic deposits form across the surface of the film. It is likely that added OLA did not readily attached to the nanocrystal surface, even after multiple hours of sonication, leading to organic agglomerations. After deposition, the films are annealed in Ar at 525°C for 1 hour to remove organics before selenization.[11] In both of the films with OLA addition, the film integrity was destroyed during the pre-selenization anneal with large holes forming across the surface due to organic residue. Due to the organic agglomerations, addition of OLA to nanocrystal ink after completion of the nanocrystal wash was not able to produce usable, crack-free films.

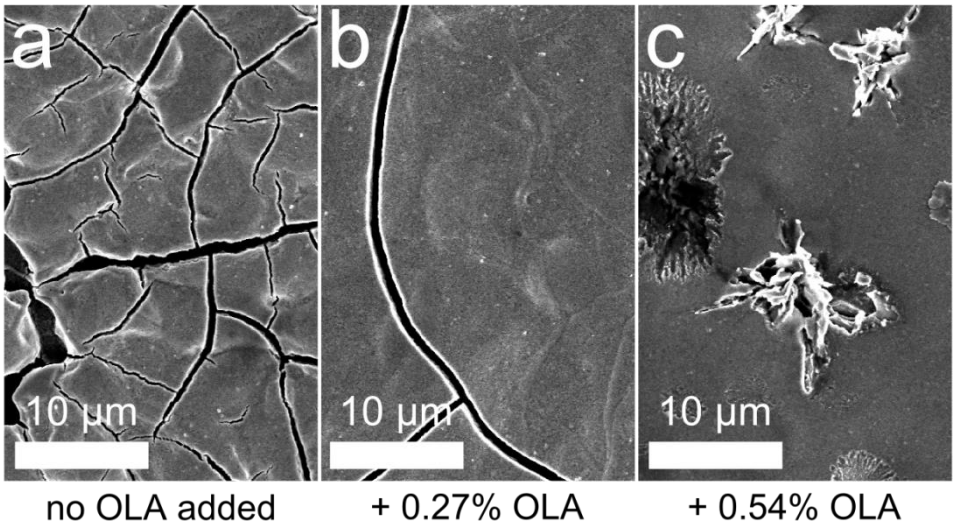

Figure 4.4 Spatial SEM of nanocrystal films with a) no added OLA, b)0.27 volume% added OLA, and c)0.54 volume% added OLA. Increased OLA leads to fewer cracks, but the surface of the film becomes decorated with organic agglomerations.

The presence of cracking in the nanocrystal film directly influences the film morphology after selenization and leads to large changes in device performance. Figure 4.5 shows spatial and cross sectional SEM for reflective and matte films before and after

selenization. The reflective films are highly uniform (Fig 4.5b) without cracking across the entire lateral surface (Fig 4.5a). In contrast, the matte films have a similar thickness with less uniformity (Fig 4.5d) and significant cracking is observed across the entire film (Fig 4.5c). The films are then annealed for 1 hour in Ar at 525°C, followed by a 10 minute selenization treatment at 500°C. The reflective films exhibit uniform grain growth across the entire film (Fig 4.5e); however, this growth does not penetrate deeply into the nanocrystal film. The matte film is highly heterogeneous after selenization. Large islands of small crystals are spread across the surface of the film (Fig 4.5g). The cross sectional SEM shows that the film has large grains that have grown under the small grained islands.

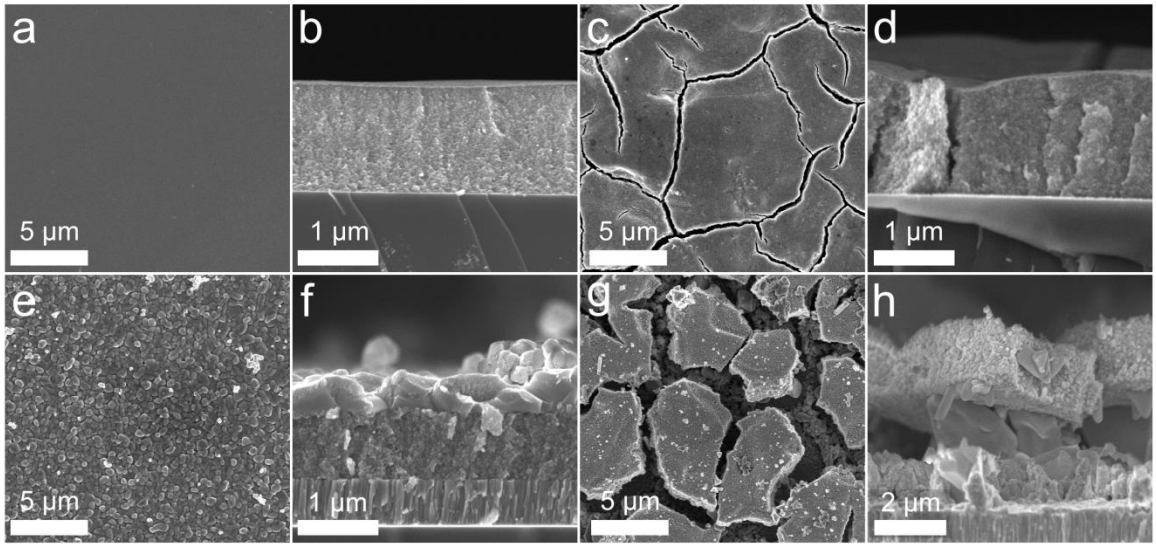

Figure 4.5 Spatial (a,c,e,g) and cross sectional (b,d,f,h) SEM images of films before (a-d) and after (e-h) selenization. The reflective film (a,b,e,f) is highly uniform after selenization, while matte films (c,d,g,h) become more heterogeneous.

The device performance is highly dependent on the post-selenization morphology. Devices made from matte films exhibited little or no photoresponse. The power

conversion efficiency (PCE) for devices made from reflective films depended on selenization temperature and initial nanocrystal film thickness. Figure 4.6 shows cross sectional SEM of 1.2 μm and 0.9 μm nanocrystal films after a 10 minute selenization at 500°C and 550°C. In films of both thicknesses, grain growth is localized to the top of the nanocrystal film (Fig 4.6a,b). The grain growth penetration depth can be increased by increasing the selenization temperature. Films of both thicknesses show complete vertical selenization at 550°C (Fig 4.6c,d). The average PCE for four devices made with films selenized at 500°C, 525°C, and 550°C of both thicknesses are shown in Figure 4.6e. Opposite PCE trends are observed as the thicker films increase PCE with temperature and the PCE decreases in the thinner films. In the thinner films, selenization of the entire vertical film is most likely completed quickly and the additional Se partial pressure at higher temperatures may over selenize the films. High and low error bars in Figure 4.6e show the PCE of the best and worst performing device of each set. The PCE variation for the thinner devices is much smaller at all temperatures.

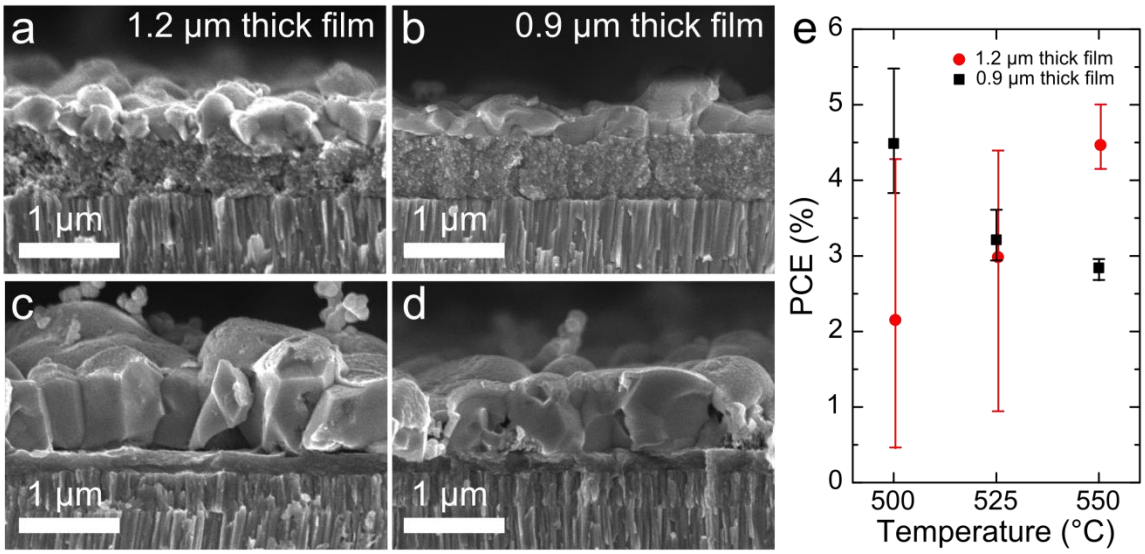

Figure 4.6 Cross section SEM of (a,c) 1.2 µm and (b,d) 0.9 µm thick nanocrystal films after selenization for 10 minutes at (a,b) 500°C and (c,b) 550°C. In nanocrystal films of both thicknesses, increased temperature leads to large grain growth throughout the vertical thickness of the film. e) Average PCE of four devices fabricated from 1.2 µm (red circles) and 0.9 µm (black squares) nanocrystal films selenized at 500°C, 525°C, and 550 °C for ten minutes. Error bars represent the highest and lowest PCE of the four devices for each experimental condition.

Increased efficiency was achieved by further optimization of the film preparation and thickness. The device with the best performance had a PCE=6.6%, V_{oc}=.43 V, J_{sc}=26.3 cm^2, and FF=0.59. The IV response and EQE measurements are shown in Figure 4.7c, and the calculated J_{sc} from the EQE data is 26.1 mA/cm^2, a very good match to the measured J_{sc}. Cross sectional SEM of nanocrystal films before (Fig 4.7a) and after (Fig 4.7b) selenization show a thickness reduction from ~1000 nm to ~350 nm. This thickness reduction continues to be one of the primary challenges to achieving high efficiencies in selenized Cu(In,Ga)Se_2 nanocrystal films. In contrast to a volume expansion reported when selenizing Cu(In,Ga)S_2 nanocrystals,[22] the volume reduction often leads to pinholes in completely selenized Cu(In,Ga)Se_2 film, lowering FF and V_{oc}. However, as continued

improvement in the processing of the films has eliminated the need to use a layer-by-layer approach, continued improvement in the processing has increase device efficiency.

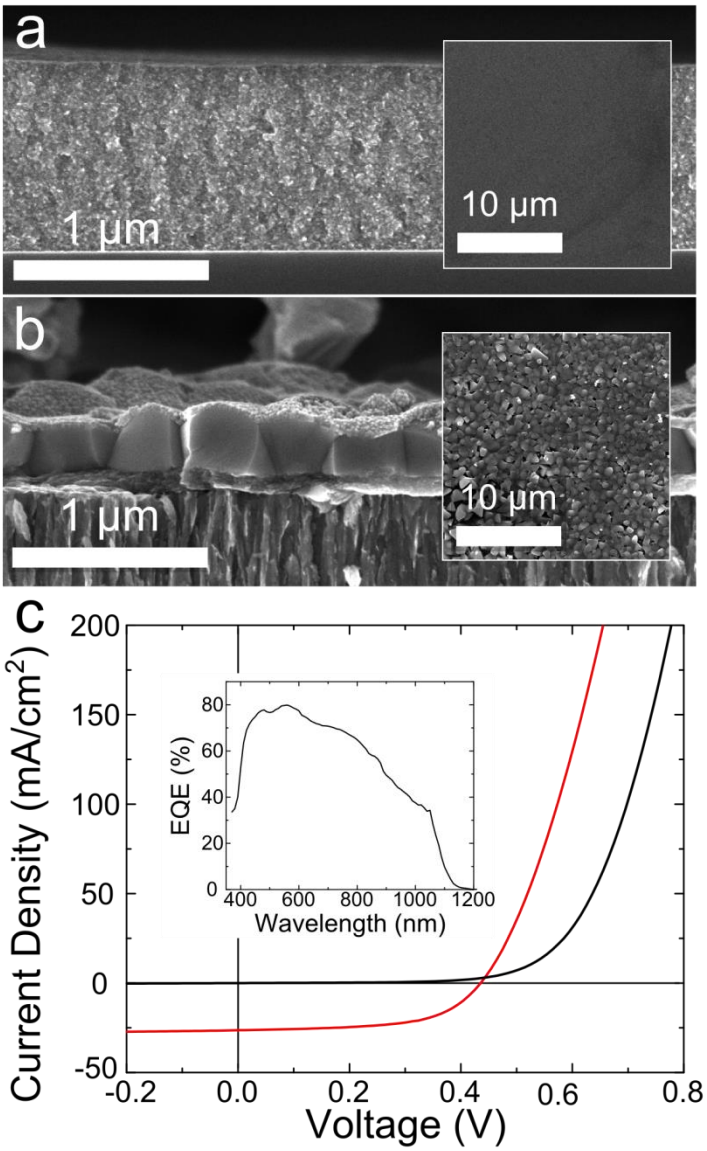

Figure 4.7 Cross sectional SEM (spatial SEM inset) of nanocrystal film a) before and b) after 10 min. 550°C selenization (images taken after CdS deposition) used to fabricate highest PCE device from ultrasonic spray deposited films. c) current-voltage response of the device showing device with PCE=6.6%, J_{sc}=26.3 mA/cm2, V_{oc}=.43 V, and FF=0.59. EQE response shown in inset.

4.4 CONCLUSIONS

Solution processed photovoltaics require a deposition method that is fully scalable to a roll-to-roll fabrication line. In this work, we have used fully automated ultrasonic spray deposition to fabricated $Cu(In,Ga)Se_2$ nanocrystal films that were then selenized and used to manufacture photovoltaics. It was found that the deposited nanocrystal film morphology was highly dependent on the ink formulation. In particular, the amount of anti-solvent used to precipitate the reaction products lead to large changes in ink organic content. Spray deposition of inks with low amounts of organic content lead to highly cracked, matte films that exhibited poor device performance after selenization. Increasing the organic content of the ink eliminated cracking and improved device performance. Optimization of the film thickness and selenization temperature lead to full conversion of the nanocrystals to large CIGS grains and higher efficiencies.

4.5 ACKNOWLEDGEMENTS

We acknowledge funding of this research by the National Science Foundation Industry/University Cooperative Research Center for Next Generation Photovoltaics (grant no. IIP-1134849) and the Robert A. Welch Foundation (grant no. F-1464). CJS and DRP also acknowledge support for this work by the National Science Foundation Graduate Research Fellowship under Grant No. DGE-1110007. FPB is grateful to Universidad Nacional de Córdoba for the exchange scholarship.

4.6 REFERENCES

(1) Bazilian, M.; Onyeji, I.; Liebreich, M.; MacGill, I.; Chase, J.; Shah, J.; Gielen, D.; Arent, D.; Landfear, D.; Zhengrong, S. Re-Considering the Economics of Photovoltaic Power. *Renew. Energy* **2013**, *53*, 329–338.

(2) Reichelstein, S.; Yorston, M. The Prospects for Cost Competitive Solar PV Power. *Energy Policy* **2013**, *55*, 117–127.

(3) Graetzel, M.; Janssen, R. A. J.; Mitzi, D. B.; Sargent, E. H. Materials Interface Engineering for Solution-Processed Photovoltaics. *Nature* **2012**, *488*, 304–312.

(4) Todorov, T. K.; Gunawan, O.; Gokmen, T.; Mitzi, D. B. Solution-Processed Cu(In,Ga)(S,Se)2 Absorber Yielding a 15.2% Efficient Solar Cell. *Prog. Photovolt. Res. Appl.* **2013**, *21*, 82–87.

(5) Hages, C. J.; Carter, N. J.; Moore, J.; McLeod, S. M.; Miskin, C. K.; Joglekar, C.; Lundstrom, M. S.; Agrawal, R. Device Comparison of Champion Nanocrystal-Ink Based CZTSSe and CIGSSe Solar Cells: Capacitance Spectroscopy. In *Photovoltaic Specialists Conference (PVSC), 2013 IEEE 39th*; 2013; pp. 1966–1971.

(6) Uhl, A. R.; Fella, C.; Chirilă, A.; Kaelin, M. R.; Karvonen, L.; Weidenkaff, A.; Borca, C. N.; Grolimund, D.; Romanyuk, Y. E.; Tiwari, A. N. Non-Vacuum Deposition of Cu(In,Ga)Se2 Absorber Layers from Binder Free, Alcohol Solutions. *Prog. Photovolt. Res. Appl.* **2012**, *20*, 526–533.

(7) Park, M.; Ahn, S.; Yun, J. H.; Gwak, J.; Cho, A.; Ahn, S.; Shin, K.; Nam, D.; Cheong, H.; Yoon, K. Characteristics of Cu(In,Ga)Se2 (CIGS) Thin Films Deposited by a Direct Solution Coating Process. *J. Alloys Compd.* **2012**, *513*, 68–74.

(8) Xie, Y.; Chen, H.; Li, A.; Zhu, X.; Zhang, L.; Qin, M.; Wang, Y.; Liu, Y.; Huang, F. A Facile Molecular Precursor-Based Cu(In,Ga)(S,Se)2 Solar Cell with 8.6% Efficiency. *J. Mater. Chem. A* **2014**, *2*, 13237–13240.

(9) Guo, Q.; Ford, G. M.; Agrawal, R.; Hillhouse, H. W. Ink Formulation and Low-Temperature Incorporation of Sodium to Yield 12% Efficient Cu(In,Ga)(S,Se)2 Solar Cells from Sulfide Nanocrystal Inks. *Prog. Photovolt. Res. Appl.* **2013**, *21*, 64–71.

(10) Park, S.-W.; Kim, D.-I.; Lee, T.-S.; Lee, K.; Yoon, Y.; Cho, Y. H.; Kim, J. H.; Ahn, K. M.; Lee, K. J.; Jeon, C.-W. Solid-State Selenization of Printed Cu(In,Ga)S2 Nanocrystal Layer and Its Impact on Solar Cell Performance. *Sol. Energy Mater. Sol. Cells* **2014**, *125*, 66–71.

(11) Harvey, T. B.; Mori, I.; Stolle, C. J.; Bogart, T. D.; Ostrowski, D. P.; Glaz, M. S.; Du, J.; Pernik, D. R.; Akhavan, V. A.; Kesrouani, H.; *et al.* Copper Indium Gallium Selenide (CIGS) Photovoltaic Devices Made Using Multistep Selenization of Nanocrystal Films. *ACS Appl. Mater. Interfaces* **2013**, *5*, 9134–9140.

(12) Akhavan, V. A.; Harvey, T. B.; Stolle, C. J.; Ostrowski, D. P.; Glaz, M. S.; Goodfellow, B. W.; Panthani, M. G.; Reid, D. K.; Vanden Bout, D. A.; Korgel, B. A. Influence of Composition on the Performance of Sintered Cu(In,Ga)Se2 Nanocrystal Thin-Film Photovoltaic Devices. *ChemSusChem* **2013**, *6*, 481–486.

(13) Kind, C.; Feldmann, C.; Quintilla, A.; Ahlswede, E. Citrate-Capped Cu11In9 Nanoparticles and Its Use for Thin-Film Manufacturing of CIS Solar Cells. *Chem Mater* **2011**, *23*, 5269–5274.

(14) Cai, Y.; Ho, J. C. W.; Batabyal, S. K.; Liu, W.; Sun, Y.; Mhaisalkar, S. G.; Wong, L. H. Nanoparticle-Induced Grain Growth of Carbon-Free Solution-Processed CuIn(S,Se)2 Solar Cell with 6% Efficiency. *ACS Appl. Mater. Interfaces* **2013**, *5*, 1533–1537.

(15) Cho, A.; Ahn, S.; Yun, J. H.; Gwak, J.; Song, H.; Yoon, K. A Hybrid Ink of Binary Copper Sulfide Nanoparticles and Indium Precursor Solution for a Dense CuInSe2 Absorber Thin Film and Its Photovoltaic Performance. *J. Mater. Chem.* **2012**, *22*, 17893–17899.

(16) Stevens, G. Thin Film CIGS Report Card - Progress in CIGS Achieving Scale. In *2012 38th IEEE Photovoltaic Specialists Conference (PVSC)*; 2012; pp. 002487–002489.

(17) Dhere, N. G. Scale-up Issues of CIGS Thin Film PV Modules. *Sol. Energy Mater. Sol. Cells* **2011**, *95*, 277–280.

(18) Panthani, M. G.; Akhavan, V.; Goodfellow, B.; Schmidtke, J. P.; Dunn, L.; Dodabalapur, A.; Barbara, P. F.; Korgel, B. A. Synthesis of CuInS2, CuInSe2, and Cu(InxGa1-x)Se2 (CIGS) Nanocrystal "Inks" for Printable Photovoltaics. *J. Am. Chem. Soc.* **2008**, *130*, 16770–16777.

(19) Hashimoto, Y.; Kohara, N.; Negami, T.; Nishitani, N.; Wada, T. Chemical Bath Deposition of Cds Buffer Layer for GIGS Solar Cells. *Sol. Energy Mater. Sol. Cells* **1998**, *50*, 71–77.

(20) Kowalczyk, B.; Lagzi, I.; Grzybowski, B. A. Nanoseparations: Strategies for Size And/or Shape-Selective Purification of Nanoparticles. *Curr. Opin. Colloid Interface Sci.* **2011**, *16*, 135–148.

(21) Murray, C. B.; Norris, D. J.; Bawendi, M. G. Synthesis and Characterization of Nearly Monodisperse CdE (E = Sulfur, Selenium, Tellurium) Semiconductor Nanocrystallites. *J. Am. Chem. Soc.* **1993**, *115*, 8706–8715.

(22) Guo, Q.; Ford, G. M.; Hillhouse, H. W.; Agrawal, R. Sulfide Nanocrystal Inks for Dense Cu(In1−xGax)(S1−ySey)2 Absorber Films and Their Photovoltaic Performance. *Nano Lett.* **2009**, *9*, 3060–3065.

Chapter 5: Photonic Curing of $CuInSe_2$ Nanocrystal Films for Photovoltaic Devices

5.1 Introduction

$Cu(In,Ga)Se_2$ (CIGS) is a promising semiconductor material for thin film photovoltaic (PV) devices, but has not made a commercial impact due to high fabrication cost compared to Si solar cells.[1,2] The fabrication cost is primarily driven by the need to process the films in vacuum conditions and at high temperature in a toxic selenium atmosphere, also known as selenization.[3] Selenization is used during CIGS film deposition during co-evaporation,[4] or as a subsequent step after physical vapor deposition (PVD) of Cu, In, and Ga metal layers.[5] To eliminate the high cost processing, $Cu(In,Ga)Se_2$ films have been fabricated using nanocrystal inks spray deposited in ambient conditions, but PV device efficiency has been limited (~3%).[6] Selenization of the nanocrystal films increases efficiency,[7] however reintroduces the high temperature selenization process. A rapid, non-toxic, roll-to-roll compatible process is needed to reduce CIGS processing cost and complexity. The use of microsecond length pulses of light, known as photonic curing, to sinter nanocrystal films at ambient pressure in a non-selenium environment is a promising route to low cost CIGS photovoltaics.

Photonic curing, also known as photonic sintering or intense pulsed light (IPL) annealing, uses short pulses of light to heat and sinter particulate films. For the treatment to be effective, the material must be a good light absorber in the wavelength range of the light source. The technique has been used primarily to sinter metal nanoparticles, with both Ag[8–10] and Cu[8,11,12] nanoparticle inks demonstrating increased conductivity after treatment. Nanoparticle semiconductor films have also been treated, primarily CIGS. Sintering of CIGS nanoparticles,[13] CuInGa and Se nanoparticle mixtures,[14] and, recently,

CIGS nanocrystals[15] has been carried out using photonic curing. While sintered films were reported in each of these cases, no working photovoltaics were demonstrated.

We recently reported $CuInSe_2$ nanocrystal PVs exhibiting multiple exciton generation (MEG) after being treated with photonic curing.[16] These devices were treated with mild energy pulses that did not sinter the nanocrystals, but reduced interparticle spacing allowing MEG extraction. In this work, the morphology of the nanocrystal layer and device characteristics after photonic curing with a wide range of pulse energies are investigated. Similar device performance is found using multiple back contact materials at mild pulse conditions. As the pulse energy increases, the nanocrystals begin to sinter into continuous films, and we find the pulsed film morphology is highly dependent on the back contact material. Nanocrystals on Mo back contacts exhibited dewetting and agglomeration, and the use of $MoSe_2$-coated Mo reduced this dewetting. Au back contacts also reduced dewetting, but the back contact was destroyed as pulse energy increased. At lower pulse energy, devices treated with photonic curing exhibit increased power conversion efficiency (PCE) compared to nontreated films. While efficiency decreases as pulse energy increases, working devices of sintered $CuInSe_2$ nanocrystal films are demonstrated on MoSe2-coated Mo.

5.2 Experimental Methods

5.2.1 Chemicals

Copper (I) chloride (CuCl, 99.99%), elemental selenium (Se, 99.99%), diphenylphosphine (DPP, 98%) were purchased from Aldrich; oleylamine (>40%) from TCI America; indium (III) chloride ($InCl_3$, 99.99%) from Strem Chemical; toluene and ethanol from Fisher Scientific. Oleylamine (OLA) was degassed at 110°C overnight. CuCl, $InCl_3$, DPP and OLA were stored in an N_2 filled glovebox.

5.2.2 Nanocrystal Synthesis

$CuInSe_2$ nanocrystals were synthesized using reported methods.[17,16] In a N2 filled glove box, 0.198 g CuCl, 0.442 g $InCl_3$, and 20 mL degassed OLA are combined in a three neck flask, removed from the glovebox and attached to a standard Schlenk line. Concurrently, 4 mmol of Se and DPP are mixed and diluted in 2 mL of OLA to form a DPP:Se solution. The 3 neck flask is degassed by heating to 100°C while pulling vaccum for 30 min. The flask is then filled with N_2 and the temperature is raised to 180^{o}C where the DPP:Se solution is injected. The reaction mixture is then heated to 240 ^{o}C for 30 min, after which the heating mantle is removed and the reaction is allowed to cool to room temperature.

Purification of the nanocrystals is conducted by centrifugation using toluene/ethanol as solvent and antisolvent. The nanocrystals are precipitated by centrifuging at 4000 rpm for 2 min after adding 20 ml of ethanol, then redispersed in 5 ml of toluene and centrifuged to separate the poorly-capped particles. The nanocrystals are precipitated again by adding 5 ml of ethanol and centrifuging. The final solution is prepared by redispersing the nanocrystals in 5 mL of toluene.

5.2.3 Nanocrystal Film Preparation

Bare glass substrates (Delta Technologies) were sonicated in 1:1 IPA/acetone for 10 minutes followed by sonication in DI water for 10 minutes. A two step rf-sputtering process was used to deposit Mo (99.95% Lesker). 400 nm of Mo was sputtered at 5 mtorr as an adhesive layer followed by 600 nm at 1.5 mtorr of highly conductive Mo. Au substrates were fabricated by thermally depositing 5 nm of Cr followed by 60 nm of Au (Kurt J. Lesker Co). $MoSe_2$ coated Mo was prepared by converting the top 50 nm of a Mo substrate to $MoSe_2$ by annealing in an Se-rich atmosphere at 450°C for 10 minutes as previously described.[7]

$CuInSe_2$ nanocrystal films with thickness between 0.5-1 □m were deposited by spray-coating from toluene dispersions (~50 mg/mL).

5.2.4 Photonic Curing

Photonic curing was performed with a Novacentrix PulseForge 3300 using pulse energies ranging from 1 J/cm^2 to 7 J/cm^2, controlled by varying the pulse voltage with a 300 μs pulse length. The reported energy inputs were measured with a bolometer (Novacentrix BX-100). For photonic curing, substrates were loaded into a stainless steel chamber with 2" thickness and 7" diameter and a 6" diameter circular quartz window. The chamber was purged with nitrogen for one minute and sealed, then positioned under the center of the xenon lamps and pulsed. A single light pulse with duration of 300 μs was used. After photonic curing, the chamber was opened in a fume hood.

5.2.5 Materials Characterization

A Rigaku R-Axis diffractometer was used to collect X-ray diffraction (XRD) data. A 10° glancing angle was used between graphite monochromatized Cu Kα (λ = 1.5418 Å) radiation operated at 40 kV and 40 mA was and the samples, which were rotated at 1° per second. Spectra were collected on an image-plate detector and two-dimensional diffraction patterns were radially integrated after background subtraction using 2DP V. 1.0 Data Processing Software (Rigaku). High resolution XRD over a short wavelength ranges was collected at 0.01 2 θ increments on a Bruker-Nonius D8 powder diffractometer equipped and 1.54 Å radiation (Cu Kα).

Scanning electron microscopy (SEM) was conducted using an In-lens detector and a 5 keV accelerating voltage on a Zeiss Supra VP SEM. A Quanta 650 FEG SEM equipped with a Bruker XFlash EDS Detector 5010 was used to collect Energy-dispersive

X-ray spectroscopy (EDS), and maps were generated at 20 kV accelerating voltage and a working distance of 10 mm with a spot size of 5.

5.2.6 PV Device Fabrication

A CdS layer (50 nm thick) was deposited on cured $CuInSe_2$ nanocrystal films by chemical bath deposition (CBD). DI water (160 mL) was heated to 70 °C and 15 mM $Cd(SO_4)_2$ (25 mL), 1.5 M thiourea (12.5 mL), and 28 wt% ammonia hydroxide (32 mL) were added. The films were then immersed for 15 minutes. ZnO (50 nm) and ITO (600 nm) was then deposited by rf-sputter coating at 2 mtorr. Physical shadow masks were used during window layer deposition, providing an active device area of 0.08 cm^2.

Current-Voltage characteristics were measured using a Keithley 2400 general purpose source meter. The devices were illumination using a Xenon lamp solar simulator (Newport) equipped with an AM1.5G optical filter and calibrated to 100 mW/cm^2 light intensity with a NIST-calibrated Si photodiode (Hamamatsu, S1787-08).

5.3 Results and Discussion

Photonic curing was carried out by exposing a $CuInSe_2$ nanocrystal film to a single 300 μs pulse of high-intensity light from a Xe lamp. Short pulse duration was utilized to limit total energy input and achieve the relatively low-energy, non-equilibrium, heating conditions needed to ensure the integrity of the back contact while exceeding the power threshold required to sinter the films.[18] The nanocrystal film heats to its peak temperature in approximately the same amount of time as the pulse length (300 μs). The peak temperature and cooling rate is determined by the amount of light absorbed and the rate of heat transfer to the metal contact, underlying substrate, and surrounding N_2 environment. Thus, the thickness of the nanocrystal film and the type of metal contact and substrate chosen greatly impact the heating profile of the film during photonic curing.

Figure 5.1 shows SEM of 600 nm thick $CuInSe_2$ nanocrystal films deposited on Mo back contacts before and after photonic curing with a 300 μs pulse at increasing energy inputs. A 1.0 J/cm^2 pulse (Fig 5.1b) leaves the majority of the film relatively unchanged from the untreated nanocrystal film (Fig 5.1a); however, some regions of sintered $CuInSe_2$ are observed. Increasing the pulse intensity to 1.3 J/cm^2 (Fig 5.1c) continues conversion of the nanocrystal film to isolated sintered $CuInSe_2$ regions. As observed in Figure 5.1d and 5.1e, further increases of pulse energy lead to almost complete dewetting and agglomeration of the film into sintered $CuInSe_2$ melt balls, leaving the Mo back contact almost completely exposed.

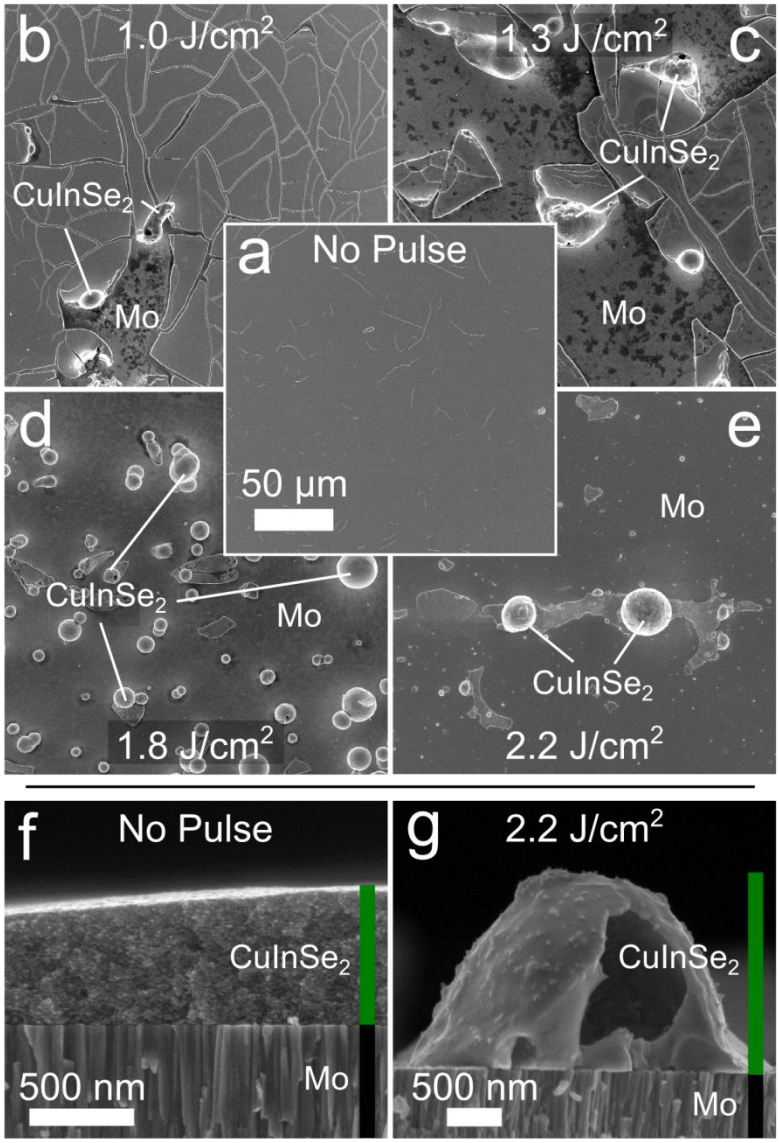

Figure 5.1 SEM images of $CuInSe_2$ nanocrystal films on Mo-coated soda lime glass a) before and after photonic curing with a 300 µs pulse with b) 1.0 J/cm^2, c) 1.3 J/cm^2, d) 1.8 J/cm^2, and e) 2.2 J/cm^2 energy. Cross sectional SEM images f) before and g) after a 2.2 J/cm^2 pulse are also shown.

Figure 5.2 shows XRD data for the films corresponding to the SEM in Figure 5.1. No new diffraction peaks appear after photonic curing and all peaks correspond to $CuInSe_2$ and Mo (reference patterns at bottom of graph). The primary change is the

narrowing of the (112) diffraction peak for $CuInSe_2$ at $2\Theta=26.65^{o}$, indicating that sintering and crystal growth occur. Slight (112) peak narrowing is observed after a 1.0 J/cm^2 pulse, which most likely corresponds to the formation of melted $CuInSe_2$ in some regions of the film. The peak continues to narrow with higher intensity photonic curing treatment. Peak narrowing reaches the machine broadening limit with a 1.8 J/cm^2 pulse.

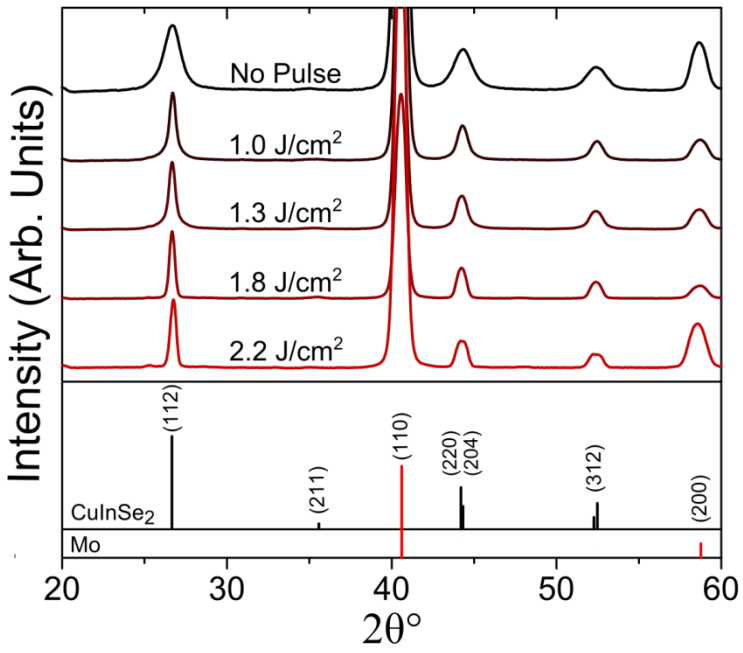

Figure 5.2 XRD of CIS deposited on Mo. XRD is shown for $CuInSe_2$ nanocrystals on Mo-coated soda-lime glass (solid lines) before and after photonic curing. Reference patterns are for chalcopyrite $CuInSe_2$ (PDF # 97-006-8928) and Mo (PDF# 97-064-3959).

Melt ball formation is significantly reduced in photonically cured $CuInSe_2$ nanocrystal films deposited on $MoSe_2$-coated Mo back contacts. $MoSe_2$-coated Mo back contacts were chosen based on the traditional CIGS photovoltaic structure. A small layer of $MoSe_2$ between the $CuInSe_2$ and Mo is formed during the selenization process, and

optimization of this layer is important for high efficiency sintered nanocrystal devices.[7] In contrast to a selenization process, no $MoSe_2$ is formed during the photonic curing process due to the rapid nature of the treatment. To add a $MoSe_2$ layer, a 50 nm layer of $MoSe_2$ on the Mo back contact was created prior to depositing the $CuInSe_2$ nanocrystals. Figure 5.3 shows SEM and Figure 5.4 shows XRD from pulsed one micron nanocrystal films on $MoSe_2$-coated Mo back contacts at different pulse energies. A 2 J/cm^2 pulse has little effect on the nanocrystal film (Fig 5.3b) and there is minimal peak narrowing of the (112) peak. Some small areas of sintered $CuInSe_2$ are formed with 2.2 J/cm^2 (Fig 5.3c) and 2.5 J/cm^2 (Fig 5.3d) pulses, but the majority of the film continues to be small grained although the (112) peak narrows in XRD. At pulse energies of 3 J/cm^2 and 3.5 J/cm^2, significant sintering is observed and the (112) peak reaches the narrowing limit due to instrument broadening. A marked change in sintering threshold between nanocrystal films on Mo and $MoSe_2$-coated Mo is observed in both the SEM and XRD. A 2.2 J/cm^2 pulse on Mo leads to strong melt ball formation and fully narrowed XRD peak, where on $MoSe_2$-coated Mo very little sintering or peak narrowing is observed. There is still coalescence of nanocrystals that leads to some exposed back contact; however, the majority of the film is covered with absorber layer unlike films treated on Mo.

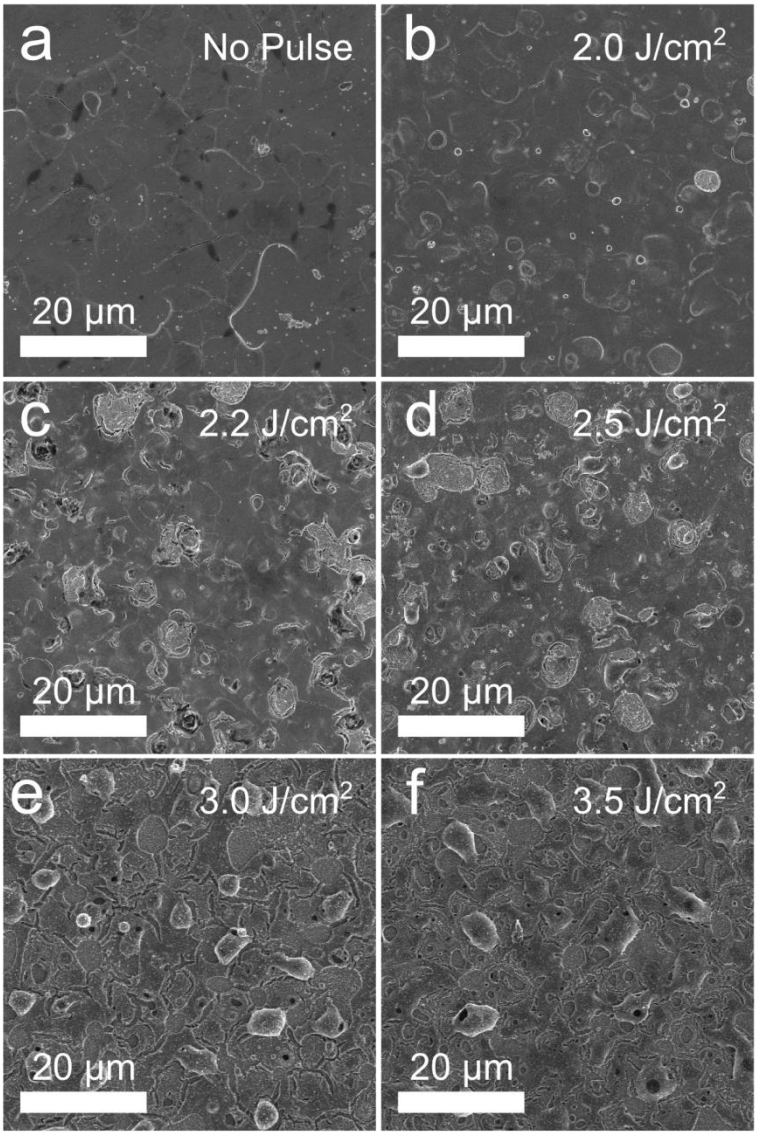

Figure 5.3 SEM images of $CuInSe_2$ nanocrystals films a) before and after b) 2 J/cm^2, c) 2.2 J/cm^2, d) 2.5 J/cm^2, e) 3 J/cm^2 and f) 3.5 J/cm^2 on $MoSe_2$-coated Mo back contacts. Minimal change is observed with lower energy pulses from the as-deposited nanocrystal film. With increasing pulse energy, more sintering is observed. Some localized $CuInSe_2$ sintering is observed; however, the formation of large melt balls is significantly reduced compared to the treatment of nanocrystal films on Mo back contacts.

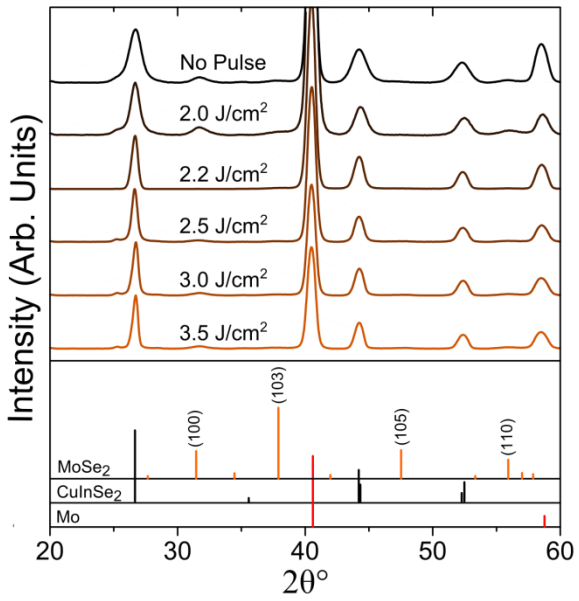

Figure 5.4 XRD data of nanocrystal films before and after 2, 2.2, 2.5, 3 and 3.5 J/cm^2 pulses on $MoSe_2$/Mo bilayer back contacts (from top to bottom). Indexed XRD references for chalcopyrite $CuInSe_2$, Mo, and $MoSe_2$ (pdf# 97-004-9800) are also shown. As is typical of $MoSe_2$ synthesized via selenization of Mo, the (103) peak intensity is significantly reduced due to the preferential orientation of the $MoSe_2$ to the underlying Mo.[19,20]

The increased grain size at higher energy pulses can also be observed in cross sectional SEM shown in Figure 5.5. Some necking of the nanoparticles can be observed after a 3 J/cm^2 pulse (Fig 5.5d); however the grain size in the majority of the film is still small. With a larger 3.5 J/cm^2 pulse, large grains are seen through the entire film (Fig 5.5f).

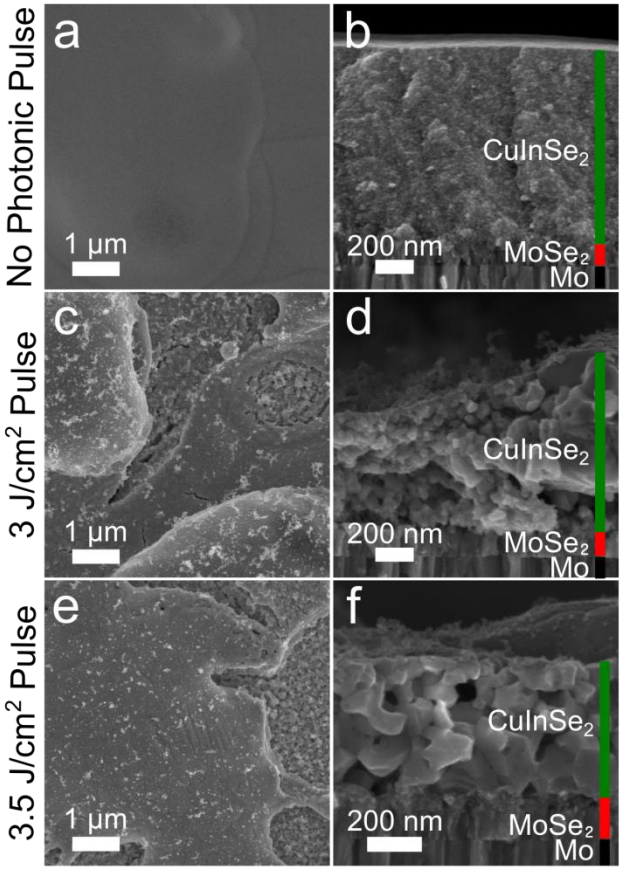

Figure 5.5 Higher magnification SEM images of $CuInSe_2$ on $MoSe_2$. (a) Spatial and (b) cross sectional SEM of films with no photonic treatment. (c) Spatial SEM of film after 3 J/cm^2 treatment showing some agglomeration of sintered CIS layer as well as areas of local sintering seen in more detail in (d)cross sectional SEM image. (e) SEM of film after 3.5 J/cm^2 pulse showing increased sintering leading to large grain CIS seen in (F)cross sectional SEM image.

The change in photonically treated film morphology from Mo to $MoSe_2$-coated glass may have several explanations. Ghosh et al.[21] show that the difference in thermal expansion between Mo and $CuInSe_2$ can lead to poor adhesion during the high temperature treatments used in $Cu(In,Ga)Se_2$ co-evaporation deposition. This thermal expansion mismatch is exacerbated due to large thermal gradients in the film due to the

brevity of the pulse, allowing the nanocrystal film to reach high temperatures while the underlying substrate remains at a lower temperature.[18] Both the thermal expansion difference and the temperature mismatch likely destabilize the $CuInSe_2$ film, leading to dewetting and agglomeration. Partial conversion of Mo to $MoSe_2$ during the standard high temperature selenization process increases adhesion between $CuInSe_2$ and Mo.[22] The increased adhesion between $MoSe_2$ and $CuInSe_2$ may prevent much of the dewetting after film destabilization during pulse treatment. Changes in surface roughness, film wetting, and potential interfacial reactions between the back contact and $CuInSe_2$ layer may also contribute to the differences in observed film morphology on Mo and $MoSe_2$.

We have recently reported in depth about low energy photonic curing treatments on Au back contacts.[16] Here we focus on higher pulse intensities that lead to necking and sintering of the nanocrystals. Figure 5.6 shows XRD and SEM images of the nanocrystal films after photonic curing at 3 and 3.5 J/cm^2. At both energy inputs, the (112) diffraction peaks are significantly narrowed after curing (Fig 5.6a). Cross sectional SEM images of films cured at 3 J/cm^2 show nanocrystal necking (Figure 5.6b) with no loss in integrity of the the 40 nm Au back contact. Similar to nanocrystal films on $MoSe_2$-coated Mo, a higher pulse energy of 3.5 J/cm^2 pulse was required to fully sinter the $CuInSe_2$ nanocrystal layer, but these conditions destroyed the Au back contact (Fig 5.6d). Figure 5.6e-g shows an EDS map of the nanocrystal film after 3.5 J/cm^2 curing with agglomerates of Au scattered throughout the $CuInSe_2$ film.

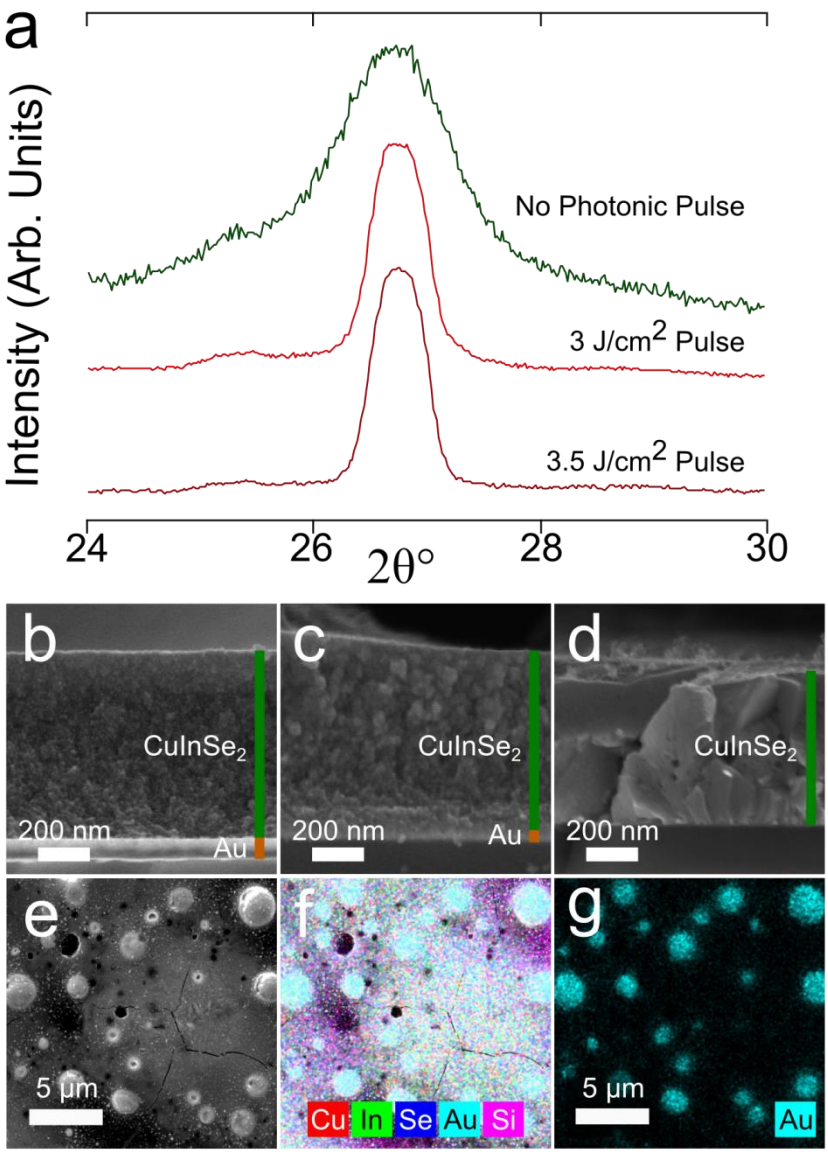

Figure 5.6 (a) XRD of CIS (112) peak before and after photonic curing with 3 and 3.5 J/cm^2 pulses of nanocrystal films deposited on Au back contacts. Cross sectional SEM images (b)before, (c) after 3 J/cm2 and (d) 3.5 J/cm^2 treatment. (e) Spatial SEM and (f-g) Spatial EDS maps of film after 3.5 J/cm^2 pulse. (f) Composite EDS response for Cu (red), In (green), Se (dark blue), Au (light blue) and Si(violet). (g) Au EDS response showing Au agglomeration scattered across the substrate.

Table 5.1 Device Characteristics of Pulsed Films deposited on $MoSe_2$-coated Mo and Au back contacts.

Energy Input (J/cm^2)	Back Contact	Voc (V)	Jsc (mA/cm^2)	FF	PCE (%)
No Pulse	$MoSe_2$/Mo	0.37	3.19	0.46	0.55
2.2	$MoSe_2$/Mo	0.30	10.6	0.34	1.05
2.5	$MoSe_2$/Mo	0.16	1.78	0.29	0.08
3	$MoSe_2$/Mo	0.20	2.85	0.28	0.16
3.5	$MoSe_2$/Mo	0.11	3.96	0.26	0.11
No Pulse	Au	0.41	5.65	0.49	1.19
2.2	Au	0.21	18.25	0.32	1.25
2.5	Au	0.21	12.87	0.31	0.85
3	Au	0.05	4.82	0.24	0.06
3.5	Au	-	-	-	-

Table 1 summarizes the performance of devices made with nanocrystal films before and after photonic curing. Photovoltaic devices fabricated using the pulsed $CuInSe_2$ nanocrystals on Mo-coated soda-lime glass as the absorber layer exhibited ohmic IV response without any measureable photocurrent due to the exposed Mo back contact. Use of the $MoSe_2$-coated Mo back contact reduced the amount of exposed back contact, and working devices were fabricated at all pulse conditions. In addition to reducing exposed back contact, the $MoSe_2$ layer is also important for device performance as it eliminates the Schottky barrier between CIGS and the Mo back contact in PV devices.[18] Au also is a better back contact than Mo for spray-deposited $CuInSe_2$ nanocrystal films since it has a higher work function than Mo, making it more suitable to form contact with the p-type $CuInSe_2$ layer.[6] Figure 5.7 shows the current/voltage

characteristics of the devices shown in table 1. Power conversion efficiency (PCE) of devices on $MoSe_2$-coated Mo and Au back contacts improve after a 2.2 J/cm_2 pulse, with both exhibiting decreases in V_{oc} and FF and increases in J_{sc}. While untreated devices on Au have higher efficiencies compared to those on $MoSe_2$/Mo, the improvement after pulsing is larger for devices on $MoSe_2$-coated Mo. As pulse intensity increases, the PCE decreases; however the device still exhibit PCE even after sintering thresholds have been reached. Films treated with 3.5 J/cm^2 pulses on Au did not have any measureable device current due to Au back contact destruction.

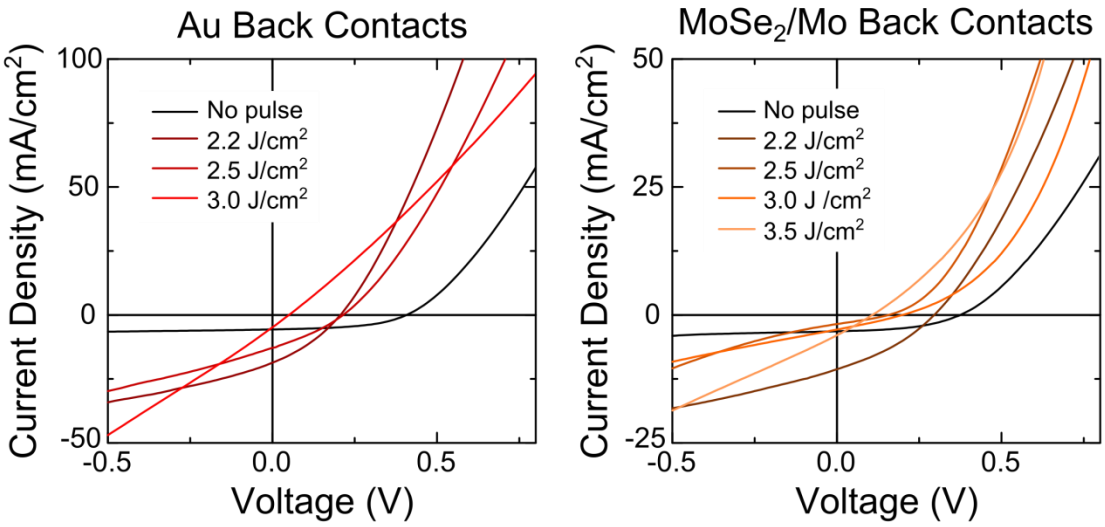

Figure 5.7 Current/Voltage characteristics of photonic cured nanocrystal films on Au (left) and $MoSe_2$-coated Mo (right) back contacts.

In comparison with untreated nanocrystal films, J_{sc} values are slightly lower for both $MoSe_2$/Mo and Au for a 3 J/cm^2 pulse. J_{sc} improves on $MoSe_2$/Mo from 3.2 to 4.0 mA/cm^2 when a nanocrystal film is pulsed with 3.5 J/cm^2. Additionally, due to exposed back contact, active $CuInSe_2$ area is smaller in the photonically cured films than as-deposited nanocrystal films. Figure 5.8 shows EDS maps from the 3 J/cm^2 pulse of films

on $MoSe_2$/Mo back contacts. Sintered absorber layer is shown in the green In EDS Maps (Fig 5.8b), while dark areas in the In maps and bright areas in the Mo EDS maps (Fig 5.8d) have no sintered $CuInSe_2$ absorber layer and would not contribute to the short circuit current. Correcting J_{sc} values for the reduced active area of the device in pulsed films would increase short circuit current values, highlighting the potential of this technique for increased device performance with improved sintered layers. Additional improvement is expected as back contact exposure from film dewetting is improved.

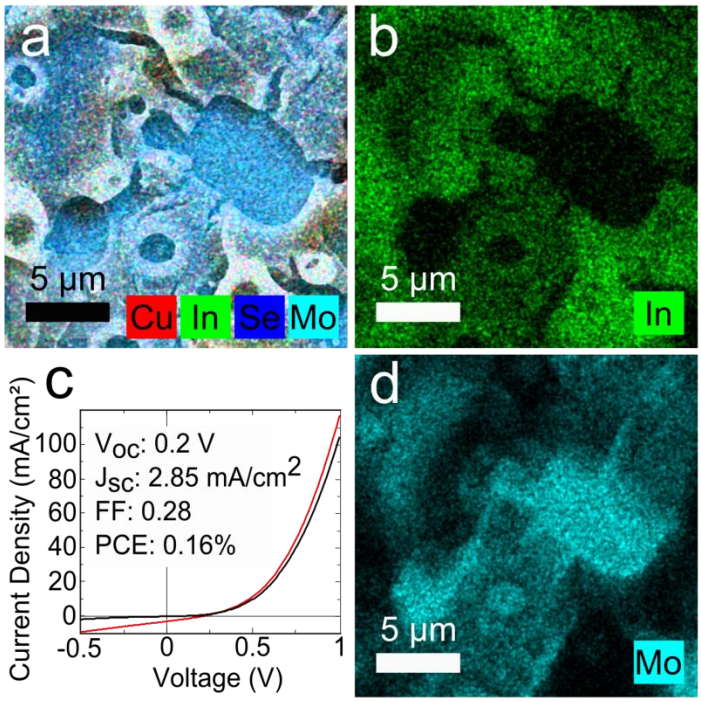

Figure 5.8 EDS maps and IV curves of sintered CIS film on $MoSe_2$/Mo back contacts with pulse energies of 3 J/cm^2. a) Cu (red), In (green), Se (dark blue), and Mo (light blue) composite response, b) green In EDS response showing absorber layer location, and d) light blue Mo EDS response showing exposed back contact. d) IV response for device after 3 J/cm^2 pulse.

5.4 CONCLUSIONS

Photonic curing is used to treat $CuInSe_2$ nanocrystal films on Mo, $MoSe_2$-coated Mo, and Au back contacts. During pulsing, large thermal gradients are generated, allowing the nanocrystal film to reach high temperatures while the underlying back contact remains at a lower temperature. Films on Mo back contacts dewett and agglomerated into large sintered $CuInSe_2$ melt balls, exposing the back contact and making the films unsuitable for photovoltaics. Nanocrystal dewetting is reduced by using a $MoSe_2$-coated Mo or Au back contact, and working devices are fabricated. Increase power conversion efficiency is demonstrated at low pulse intensities. As pulse intensity increases, PCE decreases, but working photovoltaics are manufactured with sintered $CuInSe_2$ nanocrystal films.

5.5 ACKNOWLEDGEMENTS

We acknowledge funding of this research by the National Science Foundation Industry/University Cooperative Research Center for Next Generation Photovoltaics (grant no. IIP-1134849) and the Robert A. Welch Foundation (grant no. F-1464). CJS and DRP also acknowledgesupport for this work by the National Science Foundation Graduate Research Fellowship under Grant No. DGE-1110007. We also thank Stan Farnsworth, Kurt Schroder, and Ian Rawson for insightful discussions about the photonic curing process.

5.6 REFERENCES

(1) Fraunhofer ISE. Fraunhofer Institiute For Solar Energy Systems ISE: Photovoltaics Report, 2014.

(2) Stevens, G. Thin Film CIGS Report Card - Progress in CIGS Achieving Scale. In *2012 38th IEEE Photovoltaic Specialists Conference (PVSC)*; 2012; pp. 002487–002489.

(3) Jackson, P.; Hariskos, D.; Lotter, E.; Paetel, S.; Wuerz, R.; Menner, R.; Wischmann, W.; Powalla, M. New World Record Efficiency for Cu(In,Ga)Se2

Thin-Film Solar Cells beyond 20%. *Prog. Photovolt. Res. Appl.* **2011**, *19*, 894–897.

(4) Repins, I.; Contreras, M. A.; Egaas, B.; DeHart, C.; Scharf, J.; Perkins, C. L.; To, B.; Noufi, R. 19·9%-Efficient ZnO/CdS/CuInGaSe2 Solar Cell with 81·2% Fill Factor. *Prog. Photovolt. Res. Appl.* **2008**, *16*, 235–239.

(5) Goushi, Y.; Hakuma, H.; Tabuchi, K.; Kijima, S.; Kushiya, K. Fabrication of Pentanary Cu(InGa)(SeS)2 Absorbers by Selenization and Sulfurization. *Sol. Energy Mater. Sol. Cells* **2009**, *93*, 1318–1320.

(6) Akhavan, V. A.; Panthani, M. G.; Goodfellow, B. W.; Reid, D. K.; Korgel, B. A. Thickness-Limited Performance of CuInSe2 Nanocrystal Photovoltaic Devices. *Opt. Express* **2010**, *18*, A411–A420.

(7) Harvey, T. B.; Mori, I.; Stolle, C. J.; Bogart, T. D.; Ostrowski, D. P.; Glaz, M. S.; Du, J.; Pernik, D. R.; Akhavan, V. A.; Kesrouani, H.; *et al.* Copper Indium Gallium Selenide (CIGS) Photovoltaic Devices Made Using Multistep Selenization of Nanocrystal Films. *ACS Appl. Mater. Interfaces* **2013**.

(8) Schroder, K. A.; McCool, S. C.; Furlan, W. F. Broadcast Photonic Curing of Metallic Nanoparticle Films. In; Boston, 2006.

(9) Jang, S.; Lee, D. J.; Lee, D.; Oh, J. H. Electrical Sintering Characteristics of Inkjet-Printed Conductive Ag Lines on a Paper Substrate. *Thin Solid Films* **2013**, *546*, 157–161.

(10) Lee, D. J.; Park, S. H.; Jang, S.; Kim, H. S.; Oh, J. H.; Song, Y. W. Pulsed Light Sintering Characteristics of Inkjet-Printed Nanosilver Films on a Polymer Substrate. *J. Micromechanics Microengineering* **2011**, *21*, 125023.

(11) Ryu, J.; Kim, H.-S.; Hahn, H. T. Reactive Sintering of Copper Nanoparticles Using Intense Pulsed Light for Printed Electronics. *J. Electron. Mater.* **2011**, *40*, 42–50.

(12) Joo, S.-J.; Hwang, H.-J.; Kim, H.-S. Highly Conductive Copper Nano/microparticles Ink via Flash Light Sintering for Printed Electronics. *Nanotechnology* **2014**, *25*, 265601.

(13) Dhage, S. R.; Thomas Hahn, H. Rapid Treatment of CIGS Particles by Intense Pulsed Light. *J. Phys. Chem. Solids* **2010**, *71*, 1480–1483.

(14) Dhage, S. R.; Kim, H.-S.; Hahn, H. T. Cu(In,Ga)Se2 Thin Film Preparation from a Cu(In,Ga) Metallic Alloy and Se Nanoparticles by an Intense Pulsed Light Technique. *J. Electron. Mater.* **2011**, *40*, 122–126.

(15) Singh, M.; Jiu, J.; Sugahara, T.; Suganuma, K. Photonic Sintering of Thin Film Prepared by Dodecylamine Capped CuInxGa1 -xSe2 Nanoparticles for Printed Photovoltaics. *Thin Solid Films*.

(16) Stolle, C. J.; Harvey, T. B.; Pernik, D. R.; Hibbert, J. I.; Du, J.; Rhee, D. J.; Akhavan, V. A.; Schaller, R. D.; Korgel, B. A. Multiexciton Solar Cells of CuInSe2 Nanocrystals. *J. Phys. Chem. Lett.* **2014**, *5*, 304–309.

(17) Panthani, M. G.; Stolle, C. J.; Reid, D. K.; Rhee, D. J.; Harvey, T. B.; Akhavan, V. A.; Yu, Y.; Korgel, B. A. CuInSe2 Quantum Dot Solar Cells with High Open-Circuit Voltage. *J. Phys. Chem. Lett.* **2013**, *4*, 2030–2034.

(18) Guillot, M. J.; McCool, S. C.; Schroder, K. A. Simulating the Thermal Response of Thin Films During Photonic Curing. **2012**, 19–27.

(19) Zhu, X.; Zhou, Z.; Wang, Y.; Zhang, L.; Li, A.; Huang, F. Determining Factor of MoSe2 Formation in Cu(In,Ga)Se2 Solar Cells. *Sol. Energy Mater. Sol. Cells* **2012**, *101*, 57–61.

(20) Abou-Ras, D.; Kostorz, G.; Bremaud, D.; Kälin, M.; Kurdesau, F. V.; Tiwari, A. N.; Döbeli, M. Formation and Characterisation of MoSe2 for Cu(In,Ga)Se2 Based Solar Cells. *Thin Solid Films* **2005**, *480–481*, 433–438.

(21) Ghosh, B.; Chakraborty, D. P.; Carter, M. J. A Novel Back-Contacting Technology for Thin Films. *Semicond. Sci. Technol.* **1996**, *11*, 1358.

(22) Kohara, N.; Nishiwaki, S.; Hashimoto, Y.; Negami, T.; Wada, T. Electrical Properties of the Cu(In,Ga)Se2/ MoSe2/Mo Structure. *Sol. Energy Mater. Sol. Cells* **2001**, *67*, 209–215.

Chapter 6: Multiexciton Solar Cells of $CuInSe_2$ Nanocrystals[3]

6.1 Introduction

A maximum of 34% of the energy available in sunlight can be converted to electricity by a single junction solar cell, known as the Shockley-Queisser limit.[1] The semiconductor in the device does not absorb photons with energy less than its band gap energy and photon energy greater than the band gap is lost as heat due to the rapid relaxation of the photoexcited electron and hole to their band minima before they can be extracted as electrical current. One way to surpass the Shockley-Queisser limit is to use quantum dots that convert high-energy photons into *multiple* electron-hole pairs that can be extracted as photocurrent by the device.[2,3] Colloidal nanocrystals provide a convenient source of quantum dots in which multiexciton generation (MEG) has been observed optically from a host of materials, including PbS, PbSe, PbTe, CdSe, InAs, and Si.[4–8] Extraction of more than one electron per absorbed photon as electrical current in devices has also been reported,[9–12] with a few instances of device quantum efficiencies (QE) exceeding 100%—PbS (internal QE only),[13] PbSe (external QE)[14] nanocrystal solar cells and an organic device exhibiting a related process of singlet fission.[15] Here, we report PV devices of $CuInSe_2$ nanocrystals with multiexciton generation and extraction and peak external quantum efficiencies of just over 125%.

$CuInSe_2$ is an important model semiconductor for PV devices that is closely related to $Cu(In_xGa_{1-x})Se_2$ (CIGS), which holds the record for highest device efficiency of all thin film semiconductors at just over 20%.[16] PV devices made from ink-deposited

---

[3] Portions of this chapter reproduced with permission from Stolle, C. J.; Harvey, T. B.; Pernik, D. R.; Hibbert, J. I.; Du, J.; Rhee, D. J.; Akhavan, V. A.; Schaller, R. D.; Korgel, B. A. Multiexciton Solar Cells of $CuInSe_2$ Nanocrystals. *J. Phys. Chem. Lett.* **2013**, 5, 304–309.
C. Stolle contributed to all aspects of this publication; D. Pernik, J. Hibbert, J. Du, and D. Rhee assisted with nanocrystal synthesis and device fabrication; V. Akhavan assisted with photonic curing; R. Schaller performed TAS measurements.

$CuInSe_2$ nanocrystals have reached power conversion efficiencies of 3%, limited by poor charge transport.[17–19] Ink-deposited $Cu(In_xGa_{1-x})S_2$ nanocrystals can be sintered into polycrystalline films by heating (>500°C) under selenium vapor (i.e., selenization) to achieve much higher efficiencies of just over 12%.[20,21] To try to avoid the need for high temperature selenization, an alternative nanocrystal film processing technique called photonic curing was explored here to improve charge transport in the nanocrystal film. Photonic curing was carried out using a PulseForge 3300 (NovaCentrix) tool that uses pulsed light from a flash lamp with Xenon fill gas with spectrally broad blackbody radiation that can produce very rapid heating to high temperature. Photonic curing can provide enough energy to sinter nanocrystals,[22] but in this study relatively mild pulse conditions were used to remove organic ligands and bring nanocrystals into better electrical contact without destroying their nanoscale dimensions. Nanocrystal films processed in this way were found to yield PVs with peak external quantum efficiencies (EQE) exceeding 100%, indicating the possible occurrence of multiple exciton generation (MEG) and extraction from the devices. Transient absorption spectroscopy was employed to verify that MEG does indeed occur in the nanocrystal films.

6.2 Experimental Details

6.2.1 Materials

Oleylamine (OLA) was purchased from TCI America; copper (I) chloride (CuCl; 99.99+%), gallium (III) chloride ($GaCl_3$; 99.999+%), selenium powder (Se; 99.99%), diphenylphosphine (DPP, 98%), thiourea (< 99.0%), and cadmium sulfate ($CdSO_4$; 99.999%) from Aldrich Chemical Co.; indium (III) chloride ($InCl_3$; 99.999%) from Strem Chemicals; ammonium hydroxide (18M NH_3; ACS certified), toluene (99.99%), ethanol (absolute) from Fischer Scientific. Prior to use, oleylamine was degassed overnight

under vacuum at 110°C. All other chemicals were used as received without further purification. Copper (I) chloride, indium (III) chloride, diphenylphosphine, and degassed oleylamine were stored in a N_2-filled glovebox.

6.2.2 $CuInSe_2$ nanocrystal synthesis

$CuInSe_2$ nanocrystals were synthesized according to previously reported methods.[19] Briefly, 2 mmol of CuCl, 2 mmol of $InCl_3$, and 20 mL degassed OLA were loaded into a 3-neck flask inside an N_2-filled glovebox. DPP:Se solution was made by mixing 4 mmol each of Se powder and DPP and diluting with 2mL OLA. The flask was sealed, removed from the glovebox, and attached to a Schlenk line. The reaction mixture was stirred and heated to 110°C under vacuum for a 30 minute period. It was then blanketed with nitrogen and heated to 180°C at which point the DPP:Se solution was injected. The flask was heated to 240°C and held for 30 minutes before the heating mantle was removed, allowing it to cool to room temperature. The nanocrystals were precipitated with excess ethanol and centrifuged at 4000 rpm for 2 min. The supernatant was discarded and the precipitate was redispersed in 5 mL of toluene. The dispersion was centrifuged at 4000 rpm for 1 min to precipitate poorly-capped nanocrystals. The supernatant was transferred to a centrifuge tube. Ethanol was added dropwise until the mixture became slightly turbid. After centrifugation at 4000 rpm for 1 min the supernatant was discarded, and the precipitate was dispersed in toluene. The nanocrystal dispersion was stored in a N_2-filled glovebox.

6.2.3 Film Deposition

Soda lime glass substrates (Delta Technologies) were cleaned by sonication for 10 minutes in 1:1 IPA/acetone followed by sonication in DI water for 10 minutes. 5 nm of Cr followed by 60 nm of Au (Kurt J. Lesker Co.) was then deposited by thermal

evaporation. $CuInSe_2$ nanocrystals were spray-deposited on the Au-coated substrates in approximately 500 nm thick layers from toluene dispersions (~20 mg/ml).

6.2.4 PV Device Fabrication

Photonic curing was carried out on $CuInSe_2$ nanocrystal films spray-deposited on Au-coated substrates using a PulseForge 3300 (NovaCentrix). Films were loaded into a 2 inch thick cylindrical stainless steel chamber with a 7 inch diameter and a 6 inch diameter circular quartz window on the top surface. The chamber was purged with nitrogen for one minute, sealed, positioned in the center of the xenon lamp illumination area, and then pulsed. A single 160 μs light pulse was used on each film, and the pulse voltages varied from 500 to 640 V. The energy of each pulse was 2 J/cm^2 to 3 J/cm^2 as determined by bolometer (NovaCentrix) readings at the same position and distance from the xenon lamps. 10 pulses were measured at each pulse condition and averaged to determine energy input.

Devices were completed by depositing layers of CdS, ZnO, and ITO after the photonic curing process. A CdS layer (~20 nm thick) was deposited on the nanocrystal layer by drop casting 700 μL of CdS precursor solution (1.25 mL of 15 mM $CdSO_4$, 2.2 mL of 1.5 M thiourea, and 2.8 mL of 18 M NH_4OH in water) onto the $CuInSe_2$ film heated to 95°C on a hot plate. The $CuInSe_2$ film was covered with an inverted Petri dish for two minutes while the reaction progressed. The substrate was then removed from the hot plate, rinsed with DI water, and dried under a compressed air stream. A 40 nm thick layer of ZnO followed by a 600 nm thick layer of ITO are deposited by RF-sputtering under a 2 mtorr Ar atmosphere.

6.2.5 Characterization

X-ray diffraction (XRD) was performed on a Rigaku R-Axis Spider diffractometer with an image-plate detector and using graphite monochromatized Cu Kα (λ = 1.5418 Å) radiation operated at 40 kV and 40 mA. Data were collected on nanocrystal films with and without pulse treatment on Au-coated soda-lime glass substrates. Samples were placed at a 10° glancing angle and rotated at 1° per second for 10 min. 2D diffraction patterns were radially integrated using 2DP V. 1.0 Data Processing Software (Rigaku) for 2-Dimensional detectors with subtraction of background scattering. XRD was also performed on a Bruker-Nonius D8 advance θ−2θ powder diffractometer equipped with a Bruker Sol-X Si(Li) solid state detector and 1.54 Å radiation (Cu Kα). Data were collected at 0.01 increments of 2θ at a scan rate of 6°/min. Scanning electron microscopy (SEM) was performed on a Zeiss Supra 40 VP SEM operated at 5 keV accelerating voltage through an In-lens detector. Transmission electron microscopy (TEM) was performed on an FEI Tecnai G2 Spirit BioTwin microscopy operated at 80 kV. Thermogravimetric analysis (TGA) was collected using a Mettler-Toledo DCS/TGA instrument with a temperature ramp of 20^{o}C/min under a N_2 flow. Fourier transform infrared spectroscopy (FTIR) was acquired using a Thermo Mattson Infinity Gold FTIR with a Harrick VariGART crystal. UV-Vis-NIR absorbance spectra were acquired using a Cary 500 spectrophotometer equipped with an integrating sphere to collect diffuse reflection and transmission. Transient absorption (TA) measurements were performed using an 800 nm, 35 fs pulse width, 2 kHz amplified Ti:sapphire laser. Pump pulses at 800 or 400 nm were spatially overlapped with a mechanically delayed white light probe that was produced by focusing 5% of the amplifier output into a 2-mm thick sapphire plate.

6.2.6 PV Device Testing

A Keithley 2400 general purpose source meter was used to collect current-voltage characteristics with and without exposure to a Xenon lamp solar simulator (Newport) equipped with an AM1.5G optical filter. The light source was calibrated with a NIST-calibrated Si photodiode (Hamamatsu, S1787-08). Neutral density filters with optical densities of 0.1, 0.3, 0.6, and 1.0 where used to measure PV characteristics at lower intensity light. External quantum efficiency (EQE) was measured using monochromatic light generated using a commercial monochromator (Newport Cornerstone 260 1/4M) chopped at 213 Hz and focused to a spot size of 1 mm diameter on the active region. EQE measurements were made with the device at zero bias at wavelengths ranging from 350 and 1200 nm in 10 nm increments using a lock-in-amplifier (Stanford Research Systems, model SR830) with and without a 50 mW/cm^2 white light bias. Monochromated light intensity was calibrated using calibrated photodiodes of silicon (Hamamatsu) and germanium (Judson) and white light bias intensity was measured with a thermopile (Newport 818P-020-12). Neutral density filters were used to reduce the monochromated and light bias intensity. For additional confirmation, external quantum efficiency measurements were also taken using a QEX10 Solar Cell Spectral Response Measurement System purchased commercially from PV Measurements, Inc. The system uses monochromatic light chopped at 100 Hz and is calibrated using Si and Ge diodes and shows repeatability of better than 0.6% for the 300-400 nm range and better than 0.3% for the 400-1000 nm range.

6.3 Results and Discussion

PV devices were made by spray-depositing $CuInSe_2$ nanocrystals from toluene dispersions on Au-coated soda lime glass substrates similar to Akhavan, et al.,[17] and then curing the nanocrystal films with the PulseForge tool (Figure 6.1) in a closed chamber

with a quartz window with a single 160 μs light pulse with flux ranging from 2-3 J/cm^2. The CdS buffer layer and ZnO/ITO top contacts were then added. Nanocrystal films pulsed with 2.2 J/cm^2 light reach about 600^{o}C within 1 ms, which removes oleylamine ligand but does not induce crystal grain growth. Loss of oleylamine capping ligands during photonic curing was confirmed by TGA and FTIR of the nanocrystal film. Oleylamine vaporizes from the nanocrystal film between about 150^{o}C and 400^{o}C. The TGA data in Figure 6.2 shows less mass loss in this temperature range from films that had been cured and there is systematically decreasing amount of mass loss from nanocrystal films treated with increasing pulse power. The FTIR data in Figure 6.3 shows loss of the C-H stretch absorption feature after photonic curing which is representative of the oleylamine capping ligands.

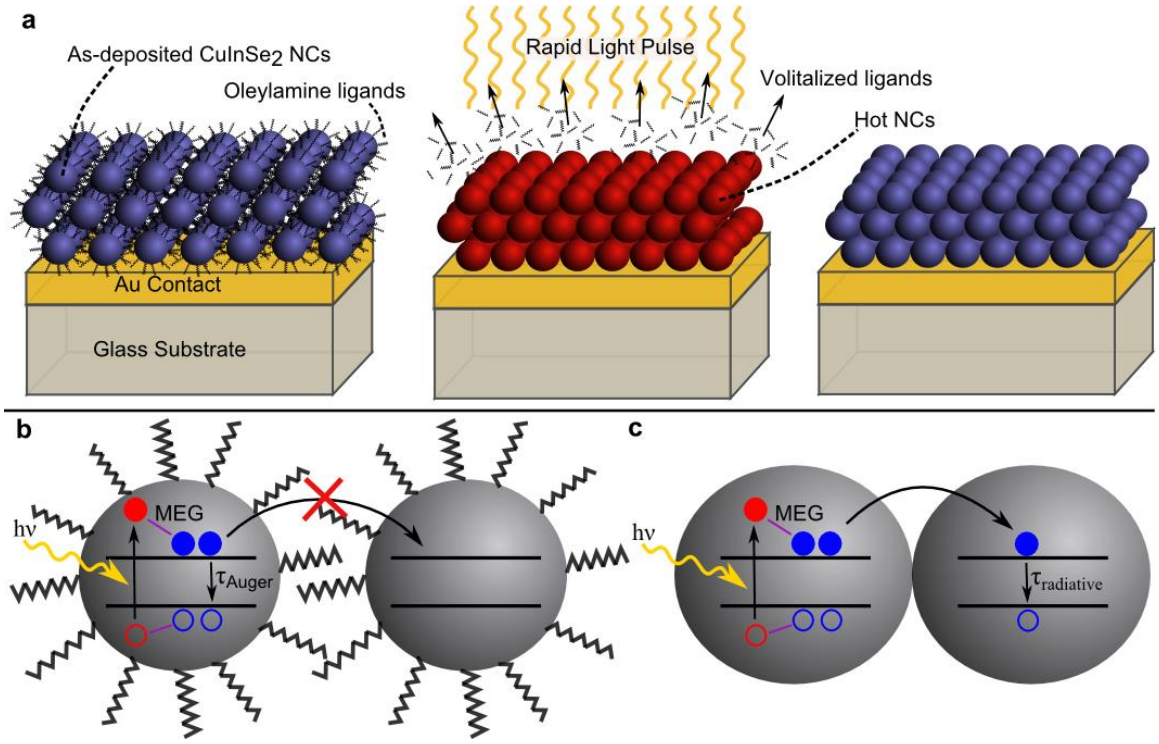

Figure 6.1 (a) Photonic curing can be used to remove oleylamine capping ligands from the $CuInSe_2$ nanocrystal film without inducing nanocrystal grain growth. (b) When the capping ligands are present, they inhibit the collection of multiexcitons from the film, leading to electron-hole recombination by Auger recombination. (c) Without the ligand barrier between nanocrystals, multiexciton transport becomes much more probable.

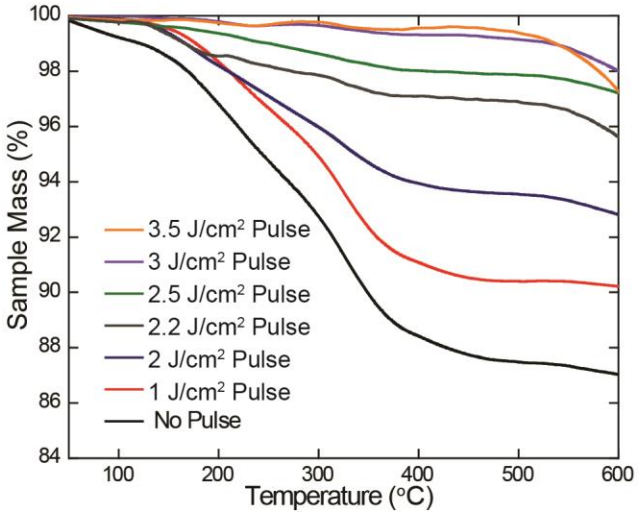

Figure 6.2 Thermogravimetric analysis (TGA) of $CuInSe_2$ nanocrystals processed by photonic curing using various pulse conditions.

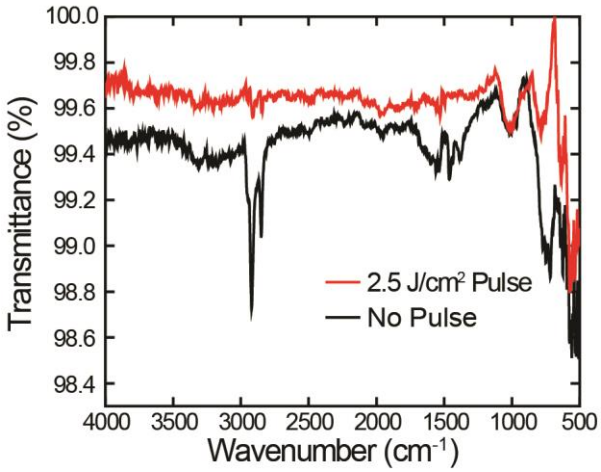

Figure 6.3. FTIR analysis of CuInSe2 nanocrystals without photonic curing (black) and treated with a 2.5 J/cm^2 pulse.

Figure 6.4 shows scanning electron microscope (SEM) images of $CuInSe_2$ nanocrystal films before and after curing with 2.2 J/cm^2 and >3 J/cm^2 exposure. The nanocrystals remain small grains after 2.2 J/cm^2 exposure, but clearly grow into larger grains after >3 J/cm^2 exposure The extent of nanocrystal sintering as a result of photonic curing was determined by examining X-ray diffraction peak widths. Figure 6.5 shows

the (112) diffraction peak for chalcopyrite $CuInSe_2$. Decreasing peak width indicates an increase in crystal domain size. Using a Scherrer analysis, the as-deposited nanocrystals are 8.3 nm in diameter, which matches well with the size measured in TEM. After curing at 2.2 J/cm^2 and 2.5 J/cm^2, the nanocrystal size is 9.2 and 23.1 nm respectively. After curing at 3 J/cm^2 and 3.5 J/cm^2, the nanocrystals have sintered and the size is too large to calculate using Scherrer analysis.

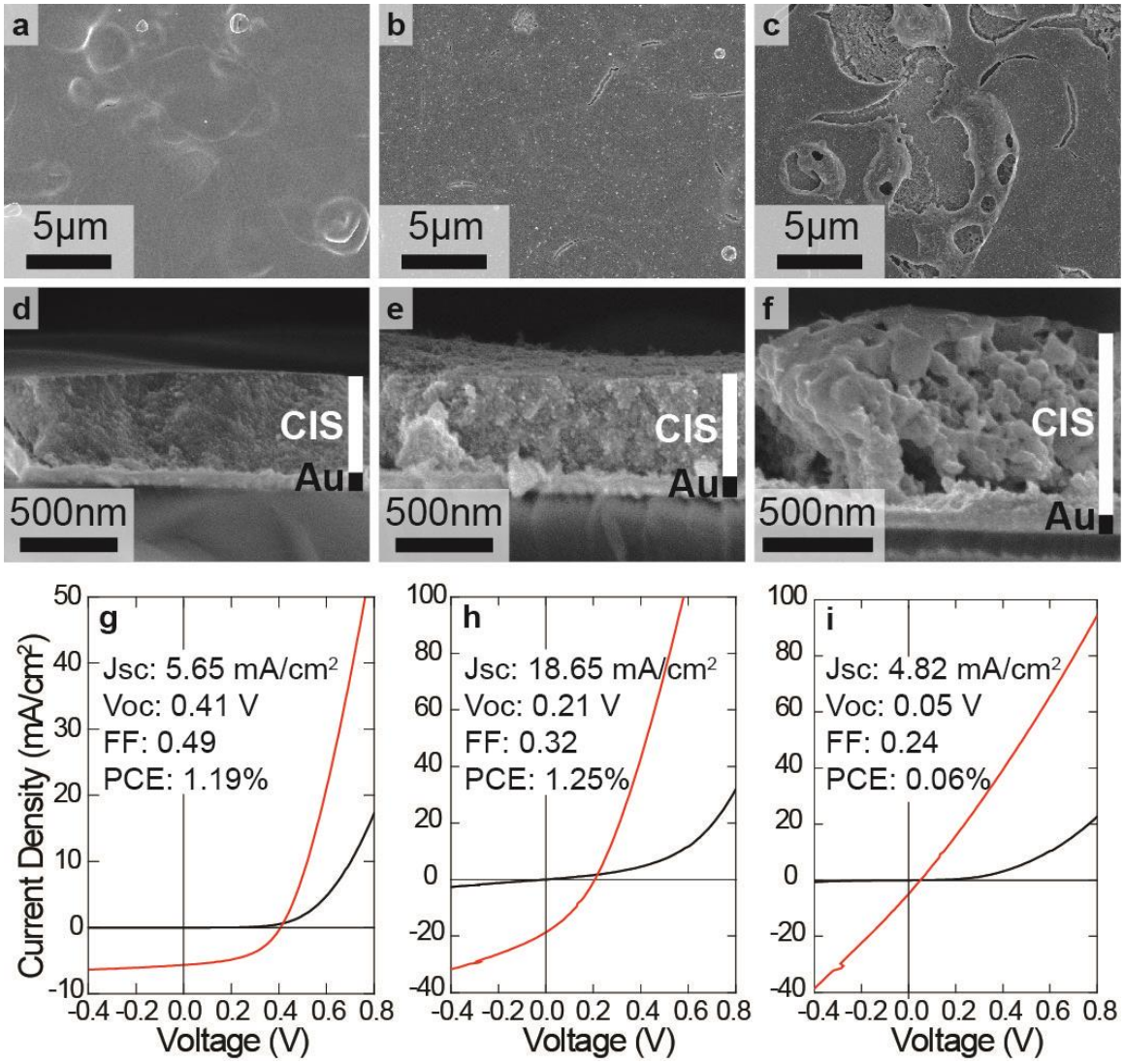

Figure 6.4 Top-down and cross-section SEM images of oleylamine-capped $CuInSe_2$ (CIS) nanocrystal film on Au-coated glass (a, d) before and after photonic curing with (b, e) 2.2 J/cm^2 and (c, f) and 3 J/cm^2 pulse fluence. (g, h, i) Corresponding current-voltage measurements (black curve is dark current; red curve is measured under AM1.5G illumination (100 mW/cm^2)) of devices made with the nanocrystal films are provided below the SEM images.

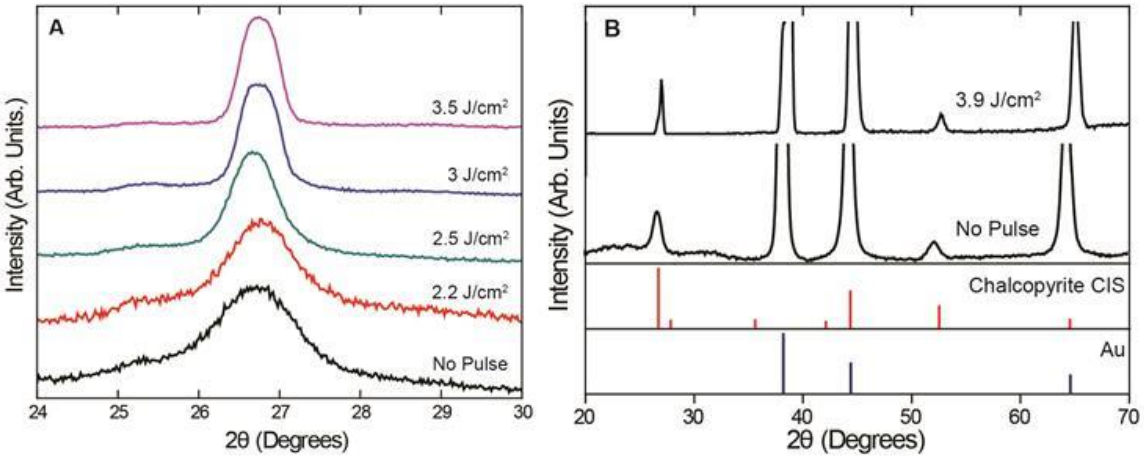

Figure 6.5 (A) X-ray diffraction (XRD) data highlighting the (112) diffraction peak of chalcopyrite $CuInSe_2$. The curves have been offset for clarity with diffraction intensity normalized to the (112) pack maxima. The crystal sizes for each pulse condition were calculated using Scherrer analysis. Prior to photonic curing, the nanocrystals are 8.3 nm in diameter, which matches well with the size measured in TEM. After curing at 2.2 J/cm^2 and 2.5 J/cm^2, the nanocrystal size is 9.2 and 23.1 nm respectively. After curing at 3 J/cm^2 and 3.5 J/cm^2, the nanocrystals have sintered and the size is too large to calculate using Scherrer analysis. (B) XRD data showing a nanocrystal film before and after curing at 3.9 J/cm^2. The red reference lines are for chalcopyrite $CuInSe_2$ (PDF #01-073-6321) and the blue lines are for Au (the back contact material) (PDF #01-075-6560).

Although the nanocrystals could be grown into large grains by photonic curing, devices made from these sintered nanocrystals performed very poorly, as shown in Figure 6.4. Exposure of 3 J/cm^2 sintered the nanocrystals, but also led to dewetting by the formation of melt balls, leaving significant back contact exposed and devices with almost no short circuit current. In contrast, devices made with nanocrystals cured using 2.2 J/cm^2 exposure gave reasonable device response with power conversion efficiency (PCE) of 1.25%, similar to the devices made with as-deposited nanocrystals (PCE=1.19%). The biggest change in device response after photonic curing is a large increase in short circuit current (Jsc) and drop in open circuit voltage (Voc), for example in Figures 6.4g the Jsc

and Voc changed from 5.65 mA/cm^2 to 18.65 mA/cm^2 and 0.41 V to 0.21 V, respectively.

EQE (also known as IPCE) measurements showed that most of the increased short circuit current in the devices made with cured nanocrystals occurred in the short wavelength (<600 nm) range. Figure 6.6a shows a comparison of EQE spectra from PVs made with as-deposited $CuInSe_2$ nanocrystals and nanocrystals that had been processed by photonic curing at 2.2 J/cm^2. The measurements in Figure 6.6a are made under a white light bias of 50 mW/cm^2. The as-deposited $CuInSe_2$ nanocrystal device has a peak EQE of about 25%, whereas the peak EQE of the cured nanocrystal device is 123%. The application of a white light bias has little effect on the as-deposited $CuInSe_2$ nanocrystal devices, but had a significant influence on the EQE spectra of the cured nanocrystal devices (See Figure 6.6b for example).

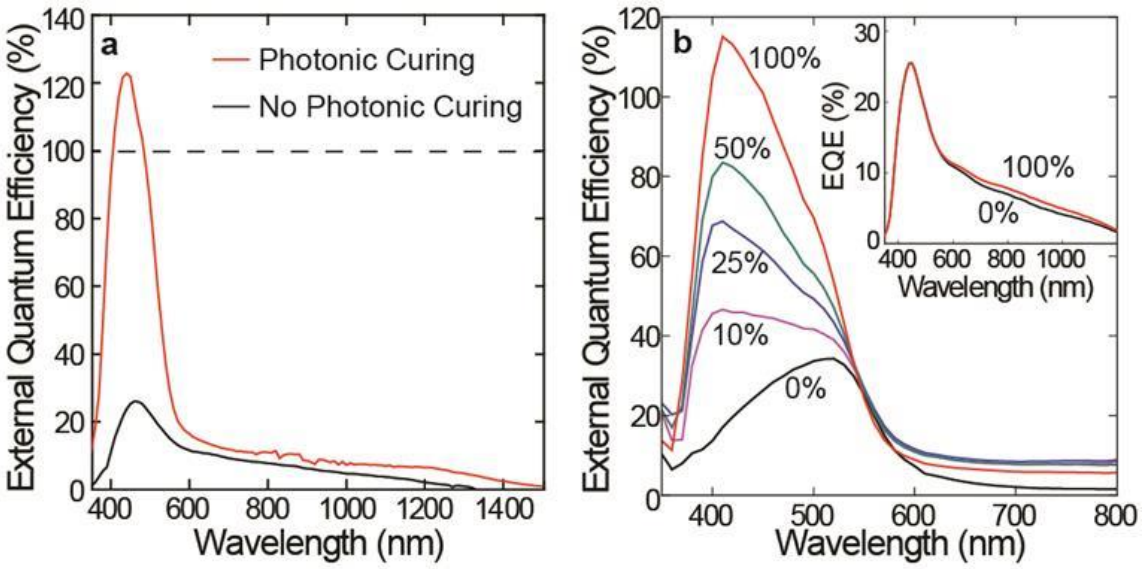

Figure 6.6 (a) EQE measurements taken under white light bias (50 mW/cm^2) for $CuInSe_2$ nanocrystal devices without photonic curing (black curve) compared to the device made with cured (2.2 J/cm^2 pulse fluence) nanocrystals (red curve). The short circuit currents determined from these data, of 4.95 mA/cm^2 and 14.29 mA/cm^2, are consistent with the short circuit currents measured under AM1.5 illumination (100 mW/cm^2). (b) EQE measured under varying white light bias intensity (100%, 50%, 25%, 10%, and 0% of a 50 mW/cm^2 bias light) with the same intensity of monochromated probe light. There is no change in EQE for the device made with as-deposited nanocrystals (inset), but the EQE decreases significantly for the cured device when the white light bias intensity was reduced to the amounts indicated.

The substantial effect of white light bias on the EQE of cured nanocrystal devices indicates that the curing process introduces traps into the nanocrystal layer that hinder charge extraction under low light conditions.[23,24] Because EQE measurements of solar cells are performed with a low-intensity monochromatic probe beam, the additional intense white light bias is required to mimic the near full sun conditions experienced by the device in the field,[25] and EQE measurements taken without white light bias can give anomalous results.[23–26] For example, traps in the CdS layer in CdTe/CdS devices usually filled under AM 1.5 illumination remain empty under low light conditions, significantly

reducing device currents and leading to artificially low EQE values if white light bias is not used.[23–26] CdTe and CIGS PV devices can also exhibit EQE variations with light bias intensity due to photoconductive CdS.[23,24,26,27] In our case, the CdS layer is the same for all devices and the EQE of the as-deposited nanocrystal device is not affected by the white light bias intensity (Figure 6.6 (b inset)). But most telling is that the EQE of the devices with peak EQE>100% was found to decrease proportionally with the *probe* light intensity (Supplementary Fig. 6.7, Table S1), additionally ruling out possible contributions from photoconductive gain or anomalous currents due to trapped carrier extraction related to the bias illumination. The EQE also did not vary with probe beam chopping frequency (Supplementary Fig. 6.8), eliminating the likelihood of measurement artifacts due to slow carrier kinetics. Lastly, the measured J_{sc} values of the $CuInSe_2$ nanocrystal devices in Figure 6.4 agree pretty well with those calculated from the EQE measurements in Figure 6.6. The measured Jsc from the as-deposited nanocrystal device was 5.65 mA/cm^2 compared to 4.95 mA/cm^2 calculated from EQE data. The cured nanocrystal device J_{sc} is 18.65 mA/cm^2 (Fig. 6.4 (h)) compared to 14.29 mA/cm^2 calculated from the EQE data. The lower calculated J_{sc} value for the cured nanocrystal device results from the fact that the white light bias intensity in our IPCE setup was limited to ~50 mW/cm^2 and since the EQE of these devices was sensitive to the bias intensity the measured EQE under white light bias was still slightly lower than under true AM1.5 illumination at 100 mW/cm^2.

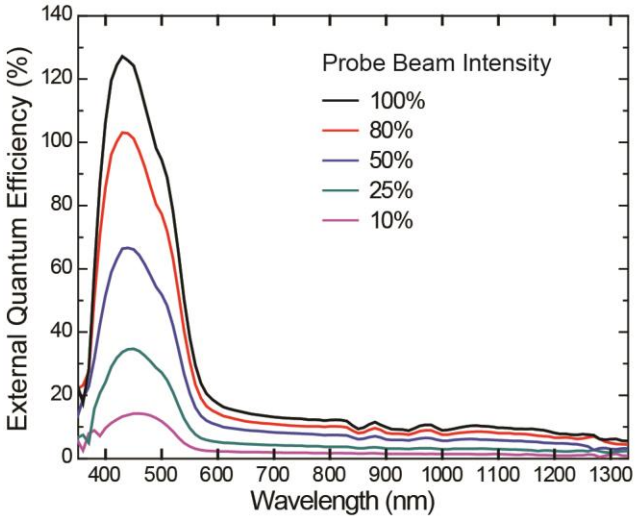

Figure 6.7 External quantum efficiency of a PV device made with $CuInSe_2$ nanocrystals cured at 2.2 J/cm^2. Neutral density filters are used to cut the monochromated probe beam to 100% (no filter, black), 80% (red), 50% (blue), 25% (green), and 10% (pink) of its original intensity. The white light bias intensity (~50 mW/cm^2) was the same for all measurements. Table S1 summarizes the peak EQE value and calculated J_{sc}.

Table 6.1 Table showing peak EQE and calculated J_{sc} for each probe beam intensity from Figure 6.7.

Probe Beam Intensity (compared to maximum)	Peak EQE (%)	% Change in EQE	Calculated J_{sc} (mA/cm^2)	% Change in Calculated J_{sc}
100%	127		14.3	
80%	103	81%	11.4	80%
50%	66	52%	7.5	52%
25%	34	27%	3.8	27%
10%	14	11%	1.6	11%

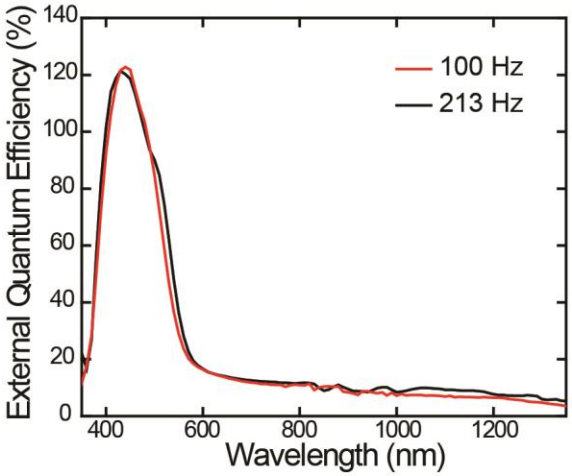

Figure 6.8 External quantum efficiency of a PV device made with $CuInSe_2$ nanocrystals cured at 2.2 J/cm^2 taken with two separate testing setups. The setup using the Newport monochrometer had a probe beam chopped at 213 Hz and the commercial setup from PV Measurements, Inc. had a probe beam chopped at 100 Hz.

To help verify that MEG occurs in the nanocrystal films that exhibit peak EQE>100%, the recombination dynamics of photoexcited excitons were determined by transient absorption (TA) spectroscopy. Additional details for the TAS measurements can be found in Stolle et. al.[28]

6.4 CONCLUSIONS

Ink-deposited $CuInSe_2$ nanocrystal PVs treated by photonic curing exhibited high short circuit currents and peak external quantum efficiencies of over 120%. TAS measurements provide substantiation that the high EQE results from the extraction of multiexcitons. It appears that photonic curing brings the nanocrystals into better electrical contact and enables multiexciton extraction. Ligand removal, however, also seems to induce a significant amount of traps in the nanocrystal film, which reduces device performance, especially under low light conditions. Passivation of these surface traps could perhaps provide a route to high efficiency devices that utilize multiexciton

generation and extraction along with reasonably efficient charge extraction for electrons and holes photoexcited closer to the band gap energy.

6.5 Acknowledgements

Financial support of this work was provided by the Robert A. Welch Foundation (F-1464) and the National Science Foundation Industry/University Cooperative Research Center on Next Generation Photovoltaics (IIP-1134849). Financial support was also provided for CJS and DRP by the National Science Foundation Graduate Research Fellowship program under Grant No. DGE-1110007. The authors also thank Sayan Saha and Sanjay Banerjee for use of their QEX10 Solar Cell Spectral Response Measurement System.

6.6 References

(1) Henry, C. H. Limiting Efficiencies of Ideal Single and Multiple Energy Gap Terrestrial Solar Cells. *J. Appl. Phys.* **1980**, *51*, 4494–4500.

(2) Hanna, M. C.; Nozik, A. J. Solar Conversion Efficiency of Photovoltaic and Photoelectrolysis Cells with Carrier Multiplication Absorbers. *J. Appl. Phys.* **2006**, *100*, 074510.

(3) Beard, M. C. Multiple Exciton Generation in Semiconductor Quantum Dots. *J. Phys. Chem. Lett.* **2011**, *2*, 1282–1288.

(4) Schaller, R. D.; Klimov, V. I. High Efficiency Carrier Multiplication in PbSe Nanocrystals: Implications for Solar Energy Conversion. *Phys. Rev. Lett.* **2004**, *92*, 186601.

(5) Beard, M. C.; Knutsen, K. P.; Yu, P.; Luther, J. M.; Song, Q.; Metzger, W. K.; Ellingson, R. J.; Nozik, A. J. Multiple Exciton Generation in Colloidal Silicon Nanocrystals. *Nano Lett.* **2007**, *7*, 2506–2512.

(6) Murphy, J. E.; Beard, M. C.; Norman, A. G.; Ahrenkiel, S. P.; Johnson, J. C.; Yu, P.; Mićić, O. I.; Ellingson, R. J.; Nozik, A. J. PbTe Colloidal Nanocrystals: Synthesis, Characterization, and Multiple Exciton Generation. *J. Am. Chem. Soc.* **2006**, *128*, 3241–3247.

(7) Lin, Z.; Franceschetti, A.; Lusk, M. T. Size Dependence of the Multiple Exciton Generation Rate in CdSe Quantum Dots. *ACS Nano* **2011**, *5*, 2503–2511.

(8) Califano, M. Direct and Inverse Auger Processes in InAs Nanocrystals: Can the Decay Signature of a Trion Be Mistaken for Carrier Multiplication? *ACS Nano* **2009**, *3*, 2706–2714.

(9) Sukhovatkin, V.; Hinds, S.; Brzozowski, L.; Sargent, E. H. Colloidal Quantum-Dot Photodetectors Exploiting Multiexciton Generation. *Science* **2009**, *324*, 1542–1544.

(10) Kim, S. J.; Kim, W. J.; Sahoo, Y.; Cartwright, A. N.; Prasad, P. N. Multiple Exciton Generation and Electrical Extraction from a PbSe Quantum Dot Photoconductor. *Appl. Phys. Lett.* **2008**, *92*, 031107.

(11) Kim, S. J.; Kim, W. J.; Cartwright, A. N.; Prasad, P. N. Carrier Multiplication in a PbSe Nanocrystal and P3HT/PCBM Tandem Cell. *Appl. Phys. Lett.* **2008**, *92*, 191107.

(12) Gabor, N. M.; Zhong, Z.; Bosnick, K.; Park, J.; McEuen, P. L. Extremely Efficient Multiple Electron-Hole Pair Generation in Carbon Nanotube Photodiodes. *Science* **2009**, *325*, 1367–1371.

(13) Sambur, J. B.; Novet, T.; Parkinson, B. A. Multiple Exciton Collection in a Sensitized Photovoltaic System. *Science* **2010**, *330*, 63–66.

(14) Semonin, O. E.; Luther, J. M.; Choi, S.; Chen, H.-Y.; Gao, J.; Nozik, A. J.; Beard, M. C. Peak External Photocurrent Quantum Efficiency Exceeding 100% via MEG in a Quantum Dot Solar Cell. *Science* **2011**, *334*, 1530–1533.

(15) Congreve, D. N.; Lee, J.; Thompson, N. J.; Hontz, E.; Yost, S. R.; Reusswig, P. D.; Bahlke, M. E.; Reineke, S.; Voorhis, T. V.; Baldo, M. A. External Quantum Efficiency Above 100% in a Singlet-Exciton-Fission–Based Organic Photovoltaic Cell. *Science* **2013**, *340*, 334–337.

(16) Jackson, P.; Hariskos, D.; Lotter, E.; Paetel, S.; Wuerz, R.; Menner, R.; Wischmann, W.; Powalla, M. New World Record Efficiency for Cu(In,Ga)Se2 Thin-Film Solar Cells beyond 20%. *Prog. Photovolt. Res. Appl.* **2011**, *19*, 894–897.

(17) Akhavan, V. A.; Panthani, M. G.; Goodfellow, B. W.; Reid, D. K.; Korgel, B. A. Thickness-Limited Performance of CuInSe2 Nanocrystal Photovoltaic Devices. *Opt. Express* **2010**, *18*, A411–A420.

(18) Stolle, C. J.; Panthani, M. G.; Harvey, T. B.; Akhavan, V. A.; Korgel, B. A. Comparison of the Photovoltaic Response of Oleylamine and Inorganic Ligand-Capped CuInSe2 Nanocrystals. *ACS Appl. Mater. Interfaces* **2012**, *4*, 2757–2761.

(19) Panthani, M. G.; Stolle, C. J.; Reid, D. K.; Rhee, D. J.; Harvey, T. B.; Akhavan, V. A.; Yu, Y.; Korgel, B. A. CuInSe2 Quantum Dot Solar Cells with High Open-Circuit Voltage. *J. Phys. Chem. Lett.* **2013**, *4*, 2030–2034.

(20) Guo, Q.; Ford, G. M.; Agrawal, R.; Hillhouse, H. W. Ink Formulation and Low-Temperature Incorporation of Sodium to Yield 12% Efficient Cu(In,Ga)(S,Se)2 Solar Cells from Sulfide Nanocrystal Inks. *Prog. Photovolt. Res. Appl.* **2013**, *21*, 64–71.

(21) Akhavan, V. A.; Harvey, T. B.; Stolle, C. J.; Ostrowski, D. P.; Glaz, M. S.; Goodfellow, B. W.; Panthani, M. G.; Reid, D. K.; Vanden Bout, D. A.; Korgel, B. A. Influence of Composition on the Performance of Sintered Cu(In,Ga)Se2 Nanocrystal Thin-Film Photovoltaic Devices. *ChemSusChem* **2013**, *6*, 481–486.

(22) Schroder, K. A. Mechanisms of Photonic Curing™: Processing High Temperature Films on Low Temperature Substrates, 2011.

(23) Hegedus, S.; Ryan, D.; Dobson, K.; McCandless, B.; Desai, D. Photoconductive CdS: How Does It Affect CdTe/CdS Solar Cell Performance? In *Symposium B – Compound Semiconductor Photovoltaics*; MRS Online Proceedings Library; 2003; Vol. 763.

(24) Gloeckler, M.; Sites, J. R. Apparent Quantum Efficiency Effects in CdTe Solar Cells. *J. Appl. Phys.* **2004**, *95*, 4438–4445.

(25) Sites, J. R.; Tavakolian, H.; Sasala, R. A. Analysis of Apparent Quantum Efficiency. *Sol. Cells* **1990**, *29*, 39–48.

(26) Hegedus, S. S. The Photoresponse of CdS/CuInSe2 Thin-Film Heterojunction Solar Cells. *IEEE Trans Electron Devices* **1984**, *31*, 629–633.

(27) Demtsu, S.; Albin, D.; Sites, J. Role of Copper in the Performance of CdS/CdTe Solar Cells. In *Conference Record of the 2006 IEEE 4th World Conference on Photovoltaic Energy Conversion*; 2006; Vol. 1, pp. 523–526.

(28) Stolle, C. J.; Harvey, T. B.; Pernik, D. R.; Hibbert, J. I.; Du, J.; Rhee, D. J.; Akhavan, V. A.; Schaller, R. D.; Korgel, B. A. Multiexciton Solar Cells of CuInSe2 Nanocrystals. *J. Phys. Chem. Lett.* **2013**, *5*, 304–309.

Chapter 7: Conclusions and Future Direction

7.1 Conclusions

Spray deposition of $Cu(In,Ga)Se_2$ (CIGS) nanocrystal inks are a promising route to low cost photovoltaics. Without any heat treatments, the CIGS nanocrystal inks have been used to fabricate 3.1% power conversion efficiency (PCE) solar cells.[1] The work presented in this dissertation shows how different sintering strategies can be used to increase the PCE.

Both selenization and photonic curing lead to a greater understanding of how to increase the efficiency of CIGS nanocrystal photovoltaics. It is my hope that the work presented here can be built on, leading to high efficiency, low cost solar cells.

7.1.1 Selenization

The primary method to sinter the CIGS nanocrystals films is annealing under a Se atmosphere, also known as selenization. Chapter 2 presented our initial work with selenization. The selenized device efficiency was found to be influenced highly by the synthesized nanocrystal composition. A Se/Carbon layer was found to decrease the PCE of the devices. As shown in Chapter 3, the Se/Carbon layer can be eliminated by annealing the nanocrystal films before the selenization treatment. This pre-selenization anneal also drives Na from the soda-lime glass substrate into the film, increasing grain growth. Efficiencies up to 7.1% were obtained by repeating the deposition, pre-selenization anneal, and selenization process. While this process leads to high efficiencies, repeated deposition and annealing increases manufacturing complexity. In Chapter 4, a single-step, scalable deposition was demonstrated by using a fully automated ultrasonic spray deposition. The ultrasonic spray deposition was highly sensitive to the nanocrystal ink organic content, and optimization of the nanocrystal synthesis wash

procedure lead to highly uniform, reflective nanocrystal films. These films were then selenized to achieve 6.6% efficient devices.

7.1.2 Photonic Curing

Although selenization leads to higher efficiencies, annealing at 500 °C or higher in a selenium atmosphere reintroduces high temperature processing to the fabrication process. An alternative sintering method that is compatible with roll-to-roll fabrication is needed. One potential technique is to sinter the nanocrystals using a rapid pulse of broadband light, also known as photonic curing. In Chapter 5, a wide range of pulse energy was used to treat nanocrystal films after spray deposition on three different back contact materials. Nanocrystal dewetting and agglomeration was observed after photonic curing of the films on a Mo, but could be reduced significantly by using Au or $MoSe_2$/Mo back contacts. Device power conversion efficiency increased at low pulse energies using both Au or MoSe2/Mo back contacts, and working devices of fully sintered nanocrystal films were demonstrated on $MoSe_2$/Mo back contacts. Chapter 6 presents our work using low energy pulses that remove the organic capping ligand and bring the nanocrystals into close electrical contact. Devices made from these films exhibited multiple exciton generation and extraction, where one high energy incident photon can lead to multiple extracted electrons.

7.2 Future Direction

7.2.1 Selenization

The need for high efficiency photovoltaics makes exploration of heated CIGS nanocrystals films such as selenization interesting for long term solar research. In order to reach the efficiencies needed for this process to be commercially viable, increased understanding of the sintering mechanism of $Cu(In,Ga)Se_2$ nanocrystals is needed. To

date, selenization of $Cu(In,Ga)S_2$ nanocrystals[2] has led to higher efficiencies than $Cu(In,Ga)Se_2$ nanocrystals. An understanding of the differing sintering pathways and of these two nanocrystal systems is important to achieving higher efficiencies in both systems. One strategy could be to use a sulfurization process to pretreat the $Cu(In,Ga)Se_2$ nanocrystals before selenization. This type of processing has led to higher efficiencies when selenizing layers of sputtered metals[3] and could be a fruitful path for nanocrystal systems. An additional selenization research area may be to increased control of the Na doping using sodium containing surfactants.

7.2.2 Low Cost Nanocrystal Devices

In the near term, however, a stronger emphasis should be placed on increasing the efficiency of the devices with no heat treatments. In the fall of 2013, a team comprised of myself, Brian Korgel, and Heath Naquin participated in the NSF Icorps program. As part of the NSF Icorps program, 114 interviews were conducted across the entire solar energy market. Due to the current cost of Si photovoltaics, there was very little interest in a selenized nanocrystal solar cell that would be used for typical utility or residential solar systems. The price of Si solar cells has decreased far enough that the price point and efficiency of the nanocrystal system would have to be improved significantly. While a bit discouraging, this feedback was very helpful.

There was enormous interest, however, in flexible solar cells made from CIGS nanocrystals. The flexible solar cell would have to be significantly less expensive than currently available commercial devices. Further interviews revealed that the production cost for flexible solar cells was ~$5-7/W. Our cost estimates indicate a low cost CIGS nanocrystal device could reach $1/W, *even at low efficiencies*. Figure 7.1 shows an early prototype demonstrating this concept.

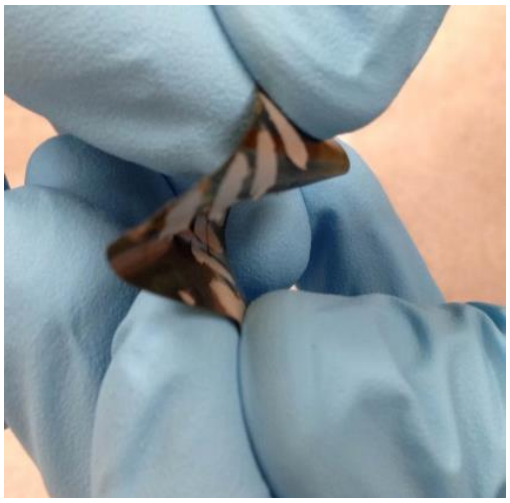

Figure 7.1 Highly flexible photovoltaic device made on PET

Recognizing the potential for low cost nanocrystal devices opens entire new areas for research. Future research in this area should focus on low cost photovoltaic architectures. One possibility would be a completely solution processed device that has no heat treatments or vacuum processing. One possible architecture is shown in Figure 7.2. The transparent contact could be comprised of a Ag nanowire/ITO nanocrystal mixture.[4,5] CIGS nanocrystals could be used as the absorber layer and a junction made using a sol-gel or nanocrystal ZnO. This type of architecture could be fully integrated with roll-to-roll fabrication processes.

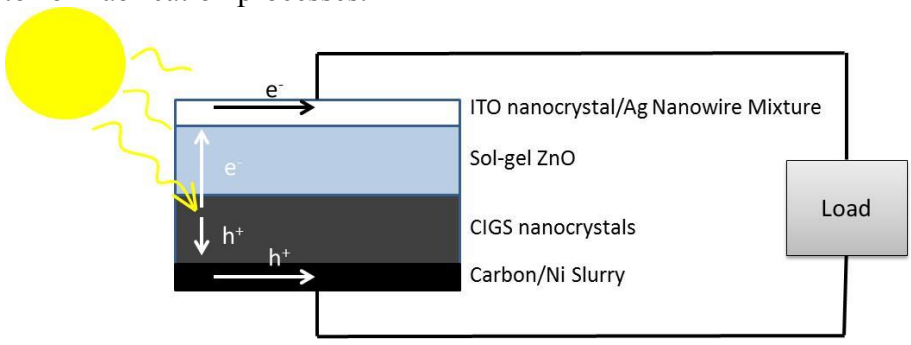

Figure 7.2 Proposed structure for a ink-deposited solar cell

7.3 REFERENCES

(1) Akhavan, V. A.; Panthani, M. G.; Goodfellow, B. W.; Reid, D. K.; Korgel, B. A. Thickness-Limited Performance of CuInSe2 Nanocrystal Photovoltaic Devices. *Opt. Express* **2010**, *18*, A411–A420.

(2) Guo, Q.; Ford, G. M.; Agrawal, R.; Hillhouse, H. W. Ink Formulation and Low-Temperature Incorporation of Sodium to Yield 12% Efficient Cu(In,Ga)(S,Se)2 Solar Cells from Sulfide Nanocrystal Inks. *Prog. Photovolt. Res. Appl.* **2013**, *21*, 64–71.

(3) Goushi, Y.; Hakuma, H.; Tabuchi, K.; Kijima, S.; Kushiya, K. Fabrication of Pentanary Cu(InGa)(SeS)2 Absorbers by Selenization and Sulfurization. *Sol. Energy Mater. Sol. Cells* **2009**, *93*, 1318–1320.

(4) Chung, C.-H.; Song, T.-B.; Bob, B.; Zhu, R.; Duan, H.-S.; Yang, Y. Silver Nanowire Composite Window Layers for Fully Solution-Deposited Thin-Film Photovoltaic Devices. *Adv. Mater.* **2012**, *24*, 5499–5504.

(5) Garcia, G.; Buonsanti, R.; Runnerstrom, E. L.; Mendelsberg, R. J.; Llordes, A.; Anders, A.; Richardson, T. J.; Milliron, D. J. Dynamically Modulating the Surface Plasmon Resonance of Doped Semiconductor Nanocrystals. *Nano Lett.* **2011**, *11*, 4415–4420.

Bibliography

Abou-Ras, D.; Kostorz, G.; Bremaud, D.; Kälin, M.; Kurdesau, F. V.; Tiwari, A. N.; Döbeli, M. Formation and Characterisation of MoSe2 for Cu(In,Ga)Se2 Based Solar Cells. *Thin Solid Films* **2005**, *480–481*, 433–438.

Akhavan, V. A.; Goodfellow, B. W.; Panthani, M. G.; Reid, D. K.; Hellebusch, D. J.; Adachi, T.; Korgel, B. A. Spray-Deposited CuInSe2 Nanocrystal Photovoltaics. *Energy Environ. Sci.* **2010**, *3*, 1600.

Akhavan, V. A.; Goodfellow, B. W.; Panthani, M. G.; Steinhagen, C.; Harvey, T. B.; Stolle, C. J.; Korgel, B. A. Colloidal CIGS and CZTS Nanocrystals: A Precursor Route to Printed Photovoltaics. *J. Solid State Chem.* **2012**, *189*, 2–12.

Akhavan, V. A.; Harvey, T. B.; Stolle, C. J.; Ostrowski, D. P.; Glaz, M. S.; Goodfellow, B. W.; Panthani, M. G.; Reid, D. K.; Vanden Bout, D. A.; Korgel, B. A. Influence of Composition on the Performance of Sintered Cu(In,Ga)Se2 Nanocrystal Thin-Film Photovoltaic Devices. *ChemSusChem* **2013**, *6*, 481–486.

Akhavan, V. A.; Panthani, M. G.; Goodfellow, B. W.; Reid, D. K.; Korgel, B. A. Thickness-Limited Performance of CuInSe2 Nanocrystal Photovoltaic Devices. *Opt. Express* **2010**, *18*, A411–A420.

Bauer, G. H.; Gütay, L.; Kniese, R. Structural Properties and Quality of the Photoexcited State in Cu(In1−xGax)Se2 Solar Cell Absorbers with Lateral Submicron Resolution. *Thin Solid Films* **2005**, *480–481*, 259–263.

Bazilian, M.; Onyeji, I.; Liebreich, M.; MacGill, I.; Chase, J.; Shah, J.; Gielen, D.; Arent, D.; Landfear, D.; Zhengrong, S. Re-Considering the Economics of Photovoltaic Power. Renew. Energy 2013, 53, 329–338.

Beard, M. C. Multiple Exciton Generation in Semiconductor Quantum Dots. *J. Phys. Chem. Lett.* **2011**, *2*, 1282–1288.

Beard, M. C.; Knutsen, K. P.; Yu, P.; Luther, J. M.; Song, Q.; Metzger, W. K.; Ellingson, R. J.; Nozik, A. J. Multiple Exciton Generation in Colloidal Silicon Nanocrystals. *Nano Lett.* **2007**, *7*, 2506–2512.

Cai, Y.; Ho, J. C. W.; Batabyal, S. K.; Liu, W.; Sun, Y.; Mhaisalkar, S. G.; Wong, L. H. Nanoparticle-Induced Grain Growth of Carbon-Free Solution-Processed CuIn(S,Se)2 Solar Cell with 6% Efficiency. *ACS Appl. Mater. Interfaces* **2013**, *5*, 1533–1537.

Califano, M. Direct and Inverse Auger Processes in InAs Nanocrystals: Can the Decay Signature of a Trion Be Mistaken for Carrier Multiplication? *ACS Nano* **2009**, *3*, 2706–2714.

Chen, G.; Seo, J.; Yang, C.; Prasad, P. N. Nanochemistry and Nanomaterials for Photovoltaics. *Chem. Soc. Rev.* **2013**.

Cho, A.; Ahn, S.; Yun, J. H.; Gwak, J.; Song, H.; Yoon, K. A Hybrid Ink of Binary Copper Sulfide Nanoparticles and Indium Precursor Solution for a Dense CuInSe2 Absorber Thin Film and Its Photovoltaic Performance. *J. Mater. Chem.* **2012**, *22*, 17893–17899.

Chung, C.-H.; Song, T.-B.; Bob, B.; Zhu, R.; Duan, H.-S.; Yang, Y. Silver Nanowire Composite Window Layers for Fully Solution-Deposited Thin-Film Photovoltaic Devices. *Adv. Mater.* **2012**, *24*, 5499–5504.

Congreve, D. N.; Lee, J.; Thompson, N. J.; Hontz, E.; Yost, S. R.; Reusswig, P. D.; Bahlke, M. E.; Reineke, S.; Voorhis, T. V.; Baldo, M. A. External Quantum Efficiency Above 100% in a Singlet-Exciton-Fission–Based Organic Photovoltaic Cell. *Science* **2013**, *340*, 334–337.

Contreras, M. A.; Tuttle, J.; Gabor, A.; Tennant, A.; Ramanathan, K.; Asher, S.; Franz, A.; Keane, J.; Wang, L.; Scofield, J.; *et al.* High Efficiency Cu(In,Ga)Se2-Based Solar Cells: Processing of Novel Absorber Structures. In *IEEE Photovoltaic Specialists Conference - 1994, 1994 IEEE First World Conference on Photovoltaic Energy Conversion, 1994., Conference Record of the Twenty Fourth*; Dec; Vol. 1, pp. 68–75 vol.1.

Demtsu, S.; Albin, D.; Sites, J. Role of Copper in the Performance of CdS/CdTe Solar Cells. In *Conference Record of the 2006 IEEE 4th World Conference on Photovoltaic Energy Conversion*; 2006; Vol. 1, pp. 523–526.

Dhage, S. R.; Kim, H.-S.; Hahn, H. T. Cu(In,Ga)Se2 Thin Film Preparation from a Cu(In,Ga) Metallic Alloy and Se Nanoparticles by an Intense Pulsed Light Technique. *J. Electron. Mater.* **2011**, *40*, 122–126.

Dhage, S. R.; Thomas Hahn, H. Rapid Treatment of CIGS Particles by Intense Pulsed Light. *J. Phys. Chem. Solids* **2010**, *71*, 1480–1483.

Dhere, N. G. Scale-up Issues of CIGS Thin Film PV Modules. *Sol. Energy Mater. Sol. Cells* **2011**, *95*, 277–280.

Eberspacher, C.; Fredric, C.; Pauls and Jack Serra, K. Thin-Film CIS Alloy PV Materials Fabricated Using Non-Vacuum, Particles-Based Techniques. *Thin Solid Films* **2001**, *387*, 18–22.

Fraunhofer ISE. Fraunhofer Institiute For Solar Energy Systems ISE: Photovoltaics Report, 2014.

Fthenakis, V. M.; Kim, H. C. Photovoltaics: Life-Cycle Analyses. *Sol. Energy* **2011**, *85*, 1609–1628.

Gabor, N. M.; Zhong, Z.; Bosnick, K.; Park, J.; McEuen, P. L. Extremely Efficient Multiple Electron-Hole Pair Generation in Carbon Nanotube Photodiodes. *Science* **2009**, *325*, 1367–1371.

Garcia, G.; Buonsanti, R.; Runnerstrom, E. L.; Mendelsberg, R. J.; Llordes, A.; Anders, A.; Richardson, T. J.; Milliron, D. J. Dynamically Modulating the Surface Plasmon Resonance of Doped Semiconductor Nanocrystals. *Nano Lett.* **2011**, *11*, 4415–4420.

Ghosh, B.; Chakraborty, D. P.; Carter, M. J. A Novel Back-Contacting Technology for Thin Films. *Semicond. Sci. Technol.* **1996**, *11*, 1358.

Gloeckler, M.; Sites, J. R. Apparent Quantum Efficiency Effects in CdTe Solar Cells. *J. Appl. Phys.* **2004**, *95*, 4438–4445.

Goushi, Y.; Hakuma, H.; Tabuchi, K.; Kijima, S.; Kushiya, K. Fabrication of Pentanary Cu(InGa)(SeS)2 Absorbers by Selenization and Sulfurization. *Sol. Energy Mater. Sol. Cells* **2009**, *93*, 1318–1320.

Graetzel, M.; Janssen, R. A. J.; Mitzi, D. B.; Sargent, E. H. Materials Interface Engineering for Solution-Processed Photovoltaics. *Nature* **2012**, *488*, 304–312.

Green, M. A.; Emery, K.; Hishikawa, Y.; Warta, W.; Dunlop, E. D. Solar Cell Efficiency Tables (version 44). *Prog. Photovolt. Res. Appl.* **2014**, *22*, 701–710.

Green, M. A.; Emery, K.; Hishikawa, Y.; Warta, W.; Dunlop, E. D. Solar Cell Efficiency Tables (version 39). *Prog. Photovolt. Res. Appl.* **2012**, *20*, 12–20.

Guillot, M. J.; McCool, S. C.; Schroder, K. A. Simulating the Thermal Response of Thin Films During Photonic Curing. **2012**, 19–27.

Guo, Q.; Ford, G. M.; Agrawal, R.; Hillhouse, H. W. Ink Formulation and Low-Temperature Incorporation of Sodium to Yield 12% Efficient Cu(In,Ga)(S,Se)2 Solar Cells from Sulfide Nanocrystal Inks. *Prog. Photovolt. Res. Appl.* **2013**, *21*, 64–71.

Guo, Q.; Ford, G. M.; Hillhouse, H. W.; Agrawal, R. Sulfide Nanocrystal Inks for Dense Cu(In1−xGax)(S1−ySey)2 Absorber Films and Their Photovoltaic Performance. *Nano Lett.* **2009**, *9*, 3060–3065.

Hages, C. J.; Carter, N. J.; Moore, J.; McLeod, S. M.; Miskin, C. K.; Joglekar, C.; Lundstrom, M. S.; Agrawal, R. Device Comparison of Champion Nanocrystal-Ink Based CZTSSe and CIGSSe Solar Cells: Capacitance Spectroscopy. In *Photovoltaic Specialists Conference (PVSC), 2013 IEEE 39th*; 2013; pp. 1966–1971.

Handbook of Photovoltaic Science and Engineering; Luque, A.; Hegedus, S., Eds.; John Wiley & Sons, Ltd, 2003.

Hanna, M. C.; Nozik, A. J. Solar Conversion Efficiency of Photovoltaic and Photoelectrolysis Cells with Carrier Multiplication Absorbers. *J. Appl. Phys.* **2006**, *100*, 074510.

Harvey, T. B.; Mori, I.; Stolle, C. J.; Bogart, T. D.; Ostrowski, D. P.; Glaz, M. S.; Du, J.; Pernik, D. R.; Akhavan, V. A.; Kesrouani, H.; *et al.* Copper Indium Gallium Selenide (CIGS) Photovoltaic Devices Made Using Multistep Selenization of Nanocrystal Films. *ACS Appl. Mater. Interfaces* **2013**, *5*, 9134–9140.

Hashimoto, Y.; Kohara, N.; Negami, T.; Nishitani, N.; Wada, T. Chemical Bath Deposition of Cds Buffer Layer for GIGS Solar Cells. *Sol. Energy Mater. Sol. Cells* **1998**, *50*, 71–77.

Hegedus, S. S. The Photoresponse of CdS/CuInSe2 Thin-Film Heterojunction Solar Cells. *IEEE Trans Electron Devices* **1984**, *31*, 629–633.

Hegedus, S.; Ryan, D.; Dobson, K.; McCandless, B.; Desai, D. Photoconductive CdS: How Does It Affect CdTe/CdS Solar Cell Performance? In *Symposium B – Compound Semiconductor Photovoltaics*; MRS Online Proceedings Library; 2003; Vol. 763.

Henry, C. H. Limiting Efficiencies of Ideal Single and Multiple Energy Gap Terrestrial Solar Cells. *J. Appl. Phys.* **1980**, *51*, 4494–4500.

Hillhouse, H. W.; Beard, M. C. Solar Cells from Colloidal Nanocrystals: Fundamentals, Materials, Devices, and Economics. *Curr. Opin. Colloid Interface Sci.* **2009**, *14*, 245–259.

Hinsch, A.; Veurman, W.; Brandt, H.; Loayza Aguirre, R.; Bialecka, K.; Flarup Jensen, K. Worldwide First Fully up-Scaled Fabrication of 60 × 100 cm2 Dye Solar Module Prototypes. *Prog. Photovolt. Res. Appl.* **2012**, *20*, 698–710.

Holdren, J. P. Science and Technology for Sustainable Well-Being. Science 2008, 319, 424–434.

Ip, A. H.; Thon, S. M.; Hoogland, S.; Voznyy, O.; Zhitomirsky, D.; Debnath, R.; Levina, L.; Rollny, L. R.; Carey, G. H.; Fischer, A.; *et al.* Hybrid Passivated Colloidal Quantum Dot Solids. *Nat. Nanotechnol.* **2012**, *7*, 577–582.

Jackson, P.; Hariskos, D.; Lotter, E.; Paetel, S.; Wuerz, R.; Menner, R.; Wischmann, W.; Powalla, M. New World Record Efficiency for Cu(In,Ga)Se2 Thin-Film Solar Cells beyond 20%. *Prog. Photovolt. Res. Appl.* **2011**, *19*, 894–897.

Jang, S.; Lee, D. J.; Lee, D.; Oh, J. H. Electrical Sintering Characteristics of Inkjet-Printed Conductive Ag Lines on a Paper Substrate. *Thin Solid Films* **2013**, *546*, 157–161.

Jeong, S.; Lee, B.-S.; Ahn, S.; Yoon, K.; Seo, Y.-H.; Choi, Y.; Ryu, B.-H. An 8.2% Efficient Solution-Processed CuInSe2 Solar Cell Based on Multiphase CuInSe2 Nanoparticles. *Energy Environ. Sci.* **2012**, *5*, 7539–7542.

Joo, S.-J.; Hwang, H.-J.; Kim, H.-S. Highly Conductive Copper Nano/microparticles Ink via Flash Light Sintering for Printed Electronics. *Nanotechnology* **2014**, *25*, 265601.

Kaelin, M.; Rudmann, D.; Kurdesau, F.; Zogg, H.; Meyer, T.; Tiwari, A. N. Low-Cost CIGS Solar Cells by Paste Coating and Selenization. *Thin Solid Films* **2005**, *480–481*, 486–490.

Kapur, V. K.; Bansal, A.; Le, P.; Asensio, O. I. Non-Vacuum Processing of CuIn1−xGaxSe2 Solar Cells on Rigid and Flexible Substrates Using Nanoparticle Precursor Inks. *Thin Solid Films* **2003**, *431–432*, 53–57.

Karg, F. High Efficiency CIGS Solar Modules. *Energy Procedia* **2012**, *15*, 275–282.

Kessler, J.; Wennerberg, J.; Bodegård, M.; Stolt, L. Highly Efficient Cu(In,Ga)Se2 Mini-Modules. *Sol. Energy Mater. Sol. Cells* **2003**, *75*, 35–46.

Kim, S. J.; Kim, W. J.; Cartwright, A. N.; Prasad, P. N. Carrier Multiplication in a PbSe Nanocrystal and P3HT/PCBM Tandem Cell. *Appl. Phys. Lett.* **2008**, *92*, 191107.

Kim, S. J.; Kim, W. J.; Sahoo, Y.; Cartwright, A. N.; Prasad, P. N. Multiple Exciton Generation and Electrical Extraction from a PbSe Quantum Dot Photoconductor. *Appl. Phys. Lett.* **2008**, *92*, 031107.

Kind, C.; Feldmann, C.; Quintilla, A.; Ahlswede, E. Citrate-Capped Cu11In9 Nanoparticles and Its Use for Thin-Film Manufacturing of CIS Solar Cells. *Chem Mater* **2011**, *23*, 5269–5274.

Kohara, N.; Nishiwaki, S.; Hashimoto, Y.; Negami, T.; Wada, T. Electrical Properties of the Cu(In,Ga)Se2/ MoSe2/Mo Structure. *Sol. Energy Mater. Sol. Cells* **2001**, *67*, 209–215.

Koo, J.; Jeon, S.; Oh, M.; Cho, H.; Son, C.; Kim, W. K. Optimization of Se Layer Thickness in Mo/CuGa/In/Se Precursor for the Formation of Cu(InGa)Se2 by Rapid Thermal Annealing. *Thin Solid Films*.

Kowalczyk, B.; Lagzi, I.; Grzybowski, B. A. Nanoseparations: Strategies for Size And/or Shape-Selective Purification of Nanoparticles. *Curr. Opin. Colloid Interface Sci.* **2011**, *16*, 135–148.

Lee, D. J.; Park, S. H.; Jang, S.; Kim, H. S.; Oh, J. H.; Song, Y. W. Pulsed Light Sintering Characteristics of Inkjet-Printed Nanosilver Films on a Polymer Substrate. *J. Micromechanics Microengineering* **2011**, *21*, 125023.

Lee, E.; Park, S. J.; Cho, J. W.; Gwak, J.; Oh, M.-K.; Min, B. K. Nearly Carbon-Free Printable CIGS Thin Films for Solar Cell Applications. *Sol. Energy Mater. Sol. Cells* **2011**, *95*, 2928–2932.

Liehr, M. Challenges for Vacuum Systems Manufacturers in the PV Industry. In *Workshop Proceedings of the 3rd International Workshop. Thin Films in the Photovoltaic Industry*; Ispra, Italy, 2007.

Lin, Z.; Franceschetti, A.; Lusk, M. T. Size Dependence of the Multiple Exciton Generation Rate in CdSe Quantum Dots. *ACS Nano* **2011**, *5*, 2503–2511.

Liu, W.; Mitzi, D. B.; Yuan, M.; Kellock, A. J.; Chey, S. J.; Gunawan, O. 12% Efficiency CuIn(Se,S)2 Photovoltaic Device Prepared Using a Hydrazine Solution Process†. *Chem. Mater.* **2010**, *22*, 1010–1014.

Mertens, K. *Photovoltaics: Fundamentals, Technology and Practice*; John Wiley & Sons Ltd, 2014.

Miles, R. W.; Hynes, K. M.; Forbes, I. Photovoltaic Solar Cells: An Overview of State-of-the-Art Cell Development and Environmental Issues. *Prog. Cryst. Growth Charact. Mater.* **2005**, *51*, 1–42.

Mitzi, D. B.; Yuan, M.; Liu, W.; Kellock, A. J.; Chey, S. J.; Deline, V.; Schrott, A. G. A High-Efficiency Solution-Deposited Thin-Film Photovoltaic Device. *Adv. Mater.* **2008**, *20*, 3657–3662.

Murphy, J. E.; Beard, M. C.; Norman, A. G.; Ahrenkiel, S. P.; Johnson, J. C.; Yu, P.; Mićić, O. I.; Ellingson, R. J.; Nozik, A. J. PbTe Colloidal Nanocrystals: Synthesis, Characterization, and Multiple Exciton Generation. *J. Am. Chem. Soc.* **2006**, *128*, 3241–3247.

Murray, C. B.; Norris, D. J.; Bawendi, M. G. Synthesis and Characterization of Nearly Monodisperse CdE (E = Sulfur, Selenium, Tellurium) Semiconductor Nanocrystallites. *J. Am. Chem. Soc.* **1993**, *115*, 8706–8715.

Niki, S.; Contreras, M.; Repins, I.; Powalla, M.; Kushiya, K.; Ishizuka, S.; Matsubara, K. CIGS Absorbers and Processes. *Prog. Photovolt. Res. Appl.* **2010**, *18*, 453–466.

NREL Best Research-Cell Efficienceis Chart http://www.nrel.gov/ncpv/images/efficiency_chart.jpg (accessed Mar 12, 2014).

Ostrowski, D. P.; Glaz, M. S.; Goodfellow, B. W.; Akhavan, V. A.; Panthani, M. G.; Korgel, B. A.; Vanden Bout, D. A. Mapping Spatial Heterogeneity in Cu(In1−xGax)Se2 Nanocrystal-Based Photovoltaics with Scanning Photocurrent and Fluorescence Microscopy. *Small* **2010**, *6*, 2832–2836.

Panthani, M. G.; Akhavan, V.; Goodfellow, B.; Schmidtke, J. P.; Dunn, L.; Dodabalapur, A.; Barbara, P. F.; Korgel, B. A. Synthesis of CuInS2, CuInSe2, and Cu(InxGa1-x)Se2 (CIGS) Nanocrystal "Inks" for Printable Photovoltaics. *J. Am. Chem. Soc.* **2008**, *130*, 16770–16777.

Panthani, M. G.; Kurley, J. M.; Crisp, R. W.; Dietz, T. C.; Ezzyat, T.; Luther, J. M.; Talapin, D. V. High Efficiency Solution Processed Sintered CdTe Nanocrystal Solar Cells: The Role of Interfaces. *Nano Lett.* **2013**, *14*, 670–675.

Panthani, M. G.; Stolle, C. J.; Reid, D. K.; Rhee, D. J.; Harvey, T. B.; Akhavan, V. A.; Yu, Y.; Korgel, B. A. CuInSe2 Quantum Dot Solar Cells with High Open-Circuit Voltage. *J. Phys. Chem. Lett.* **2013**, *4*, 2030–2034.

Park, M.; Ahn, S.; Yun, J. H.; Gwak, J.; Cho, A.; Ahn, S.; Shin, K.; Nam, D.; Cheong, H.; Yoon, K. Characteristics of Cu(In,Ga)Se2 (CIGS) Thin Films Deposited by a Direct Solution Coating Process. *J. Alloys Compd.* **2012**, *513*, 68–74.

Park, S.-W.; Kim, D.-I.; Lee, T.-S.; Lee, K.; Yoon, Y.; Cho, Y. H.; Kim, J. H.; Ahn, K. M.; Lee, K. J.; Jeon, C.-W. Solid-State Selenization of Printed Cu(In,Ga)S2 Nanocrystal Layer and Its Impact on Solar Cell Performance. *Sol. Energy Mater. Sol. Cells* **2014**, *125*, 66–71.

Peng, J.; Lu, L.; Yang, H. Review on Life Cycle Assessment of Energy Payback and Greenhouse Gas Emission of Solar Photovoltaic Systems. *Renew. Sustain. Energy Rev.* **2013**, *19*, 255–274.

Powalla, M.; Voorwinden, G.; Hariskos, D.; Jackson, P.; Kniese, R. Highly Efficient CIS Solar Cells and Modules Made by the Co-Evaporation Process. *Thin Solid Films* **2009**, *517*, 2111–2114.

Probst, V.; Karg, F.; Rimmasch, J.; Riedl, W.; Stetter, W.; Harms, H.; Eibl, O. Advanced Stacked Elemental Layer Process for Cu(InGa)Se2 Thin Film Photovoltaic Devices. *MRS Proc.* **1996**, *426*, null – null.

Rau, U.; Schock, H. W. Electronic Properties of Cu(In,Ga)Se2 Heterojunction Solar Cells–recent Achievements, Current Understanding, and Future Challenges. *Appl. Phys. A* **1999**, *69*, 131–147.

Reichelstein, S.; Yorston, M. The Prospects for Cost Competitive Solar PV Power. Energy Policy 2013, 55, 117–127.

Repins, I.; Contreras, M. A.; Egaas, B.; DeHart, C.; Scharf, J.; Perkins, C. L.; To, B.; Noufi, R. 19·9%-Efficient ZnO/CdS/CuInGaSe2 Solar Cell with 81·2% Fill Factor. *Prog. Photovolt. Res. Appl.* **2008**, *16*, 235–239.

Repins, I.; Contreras, M.; Romero, M.; Yan, Y.; Metzger, W.; Li, J.; Johnston, S.; Egaas, B.; DeHart, C.; Scharf, J.; *et al.* Characterization of 19.9%-Efficient CIGS Absorbers. In *33rd IEEE Photovoltaic Specialists Conference, 2008. PVSC '08*; 2008; pp. 1–6.

Ryu, J.; Kim, H.-S.; Hahn, H. T. Reactive Sintering of Copper Nanoparticles Using Intense Pulsed Light for Printed Electronics. *J. Electron. Mater.* **2011**, *40*, 42–50.

Sambur, J. B.; Novet, T.; Parkinson, B. A. Multiple Exciton Collection in a Sensitized Photovoltaic System. *Science* **2010**, *330*, 63–66.

Schaller, R. D.; Klimov, V. I. High Efficiency Carrier Multiplication in PbSe Nanocrystals: Implications for Solar Energy Conversion. *Phys. Rev. Lett.* **2004**, *92*, 186601.

Schroder, K. A. Mechanisms of Photonic Curing™: Processing High Temperature Films on Low Temperature Substrates, 2011.

Schroder, K. A.; McCool, S. C.; Furlan, W. F. Broadcast Photonic Curing of Metallic Nanoparticle Films. In; Boston, 2006.

Semonin, O. E.; Luther, J. M.; Choi, S.; Chen, H.-Y.; Gao, J.; Nozik, A. J.; Beard, M. C. Peak External Photocurrent Quantum Efficiency Exceeding 100% via MEG in a Quantum Dot Solar Cell. *Science* **2011**, *334*, 1530–1533.

Singh, M.; Jiu, J.; Sugahara, T.; Suganuma, K. Photonic Sintering of Thin Film Prepared by Dodecylamine Capped CuInxGa1 -xSe2 Nanoparticles for Printed Photovoltaics. *Thin Solid Films*.

Sites, J. R.; Tavakolian, H.; Sasala, R. A. Analysis of Apparent Quantum Efficiency. *Sol. Cells* **1990**, *29*, 39–48.

Snaith, H. J. Perovskites: The Emergence of a New Era for Low-Cost, High-Efficiency Solar Cells. *J. Phys. Chem. Lett.* **2013**, 3623–3630.

Søndergaard, R. R.; Hösel, M.; Krebs, F. C. Roll-to-Roll Fabrication of Large Area Functional Organic Materials. *J. Polym. Sci. Part B Polym. Phys.* **2013**, *51*, 16–34.

Stevens, G. Thin Film CIGS Report Card - Progress in CIGS Achieving Scale. In *2012 38th IEEE Photovoltaic Specialists Conference (PVSC)*; 2012; pp. 002487–002489.

Stolle, C. J.; Harvey, T. B.; Korgel, B. A. Nanocrystal Photovoltaics: A Review of Recent Progress. *Curr. Opin. Chem. Eng.* **2013**, *2*, 160–167.

Stolle, C. J.; Harvey, T. B.; Pernik, D. R.; Hibbert, J. I.; Du, J.; Rhee, D. J.; Akhavan, V. A.; Schaller, R. D.; Korgel, B. A. Multiexciton Solar Cells of CuInSe2 Nanocrystals. *J. Phys. Chem. Lett.* **2014**, *5*, 304–309.

Stolle, C. J.; Harvey, T. B.; Pernik, D. R.; Hibbert, J. I.; Du, J.; Rhee, D. J.; Akhavan, V. A.; Schaller, R. D.; Korgel, B. A. Multiexciton Solar Cells of CuInSe2 Nanocrystals. *J. Phys. Chem. Lett.* **2013**, *5*, 304–309.

Stolle, C. J.; Panthani, M. G.; Harvey, T. B.; Akhavan, V. A.; Korgel, B. A. Comparison of the Photovoltaic Response of Oleylamine and Inorganic Ligand-Capped CuInSe2 Nanocrystals. *ACS Appl. Mater. Interfaces* **2012**, *4*, 2757–2761.

Sukhovatkin, V.; Hinds, S.; Brzozowski, L.; Sargent, E. H. Colloidal Quantum-Dot Photodetectors Exploiting Multiexciton Generation. *Science* **2009**, *324*, 1542–1544.

SunShot Vision Study; DOE/GO-102012-3037; U.S. Department of Energy, 2012.

Todorov, T. K.; Gunawan, O.; Gokmen, T.; Mitzi, D. B. Solution-Processed Cu(In,Ga)(S,Se)2 Absorber Yielding a 15.2% Efficient Solar Cell. *Prog. Photovolt. Res. Appl.* **2013**, *21*, 82–87.

Uhl, A. R.; Fella, C.; Chirilă, A.; Kaelin, M. R.; Karvonen, L.; Weidenkaff, A.; Borca, C. N.; Grolimund, D.; Romanyuk, Y. E.; Tiwari, A. N. Non-Vacuum Deposition of Cu(In,Ga)Se2 Absorber Layers from Binder Free, Alcohol Solutions. *Prog. Photovolt. Res. Appl.* **2012**, *20*, 526–533.

Voorwinden, G.; Kniese, R.; Powalla, M. In-Line Cu(In,Ga)Se2 Co-Evaporation Processes with Graded Band Gaps on Large Substrates. *Thin Solid Films* **2003**, *431–432*, 538–542.

Wallin, E.; Malm, U.; Jarmar, T.; Edoff, Olle Lundberg, M.; Stolt, L. World-Record Cu(In,Ga)Se2-Based Thin-Film Sub-Module with 17.4% Efficiency. *Prog. Photovolt. Res. Appl.* **2012**, *20*, 851–854.

Wang, G.; Wang, S.; Cui, Y.; Pan, D. A Novel and Versatile Strategy to Prepare Metal–Organic Molecular Precursor Solutions and Its Application in Cu(In,Ga)(S,Se)2 Solar Cells. *Chem. Mater.* **2012**, *24*, 3993–3997.

Wilkommen, U.; Diemer, M. Thin Film Photovoltaic Production Technology. In *Workshop Proceedings of the 3rd International Workshop. Thin Films in the Photovoltaic Industry*; Ispra, Italy, 2007.

Xie, Y.; Chen, H.; Li, A.; Zhu, X.; Zhang, L.; Qin, M.; Wang, Y.; Liu, Y.; Huang, F. A Facile Molecular Precursor-Based Cu(In,Ga)(S,Se)2 Solar Cell with 8.6% Efficiency. *J. Mater. Chem. A* **2014**, *2*, 13237–13240.

Zhu, X.; Zhou, Z.; Wang, Y.; Zhang, L.; Li, A.; Huang, F. Determining Factor of MoSe2 Formation in Cu(In,Ga)Se2 Solar Cells. *Sol. Energy Mater. Sol. Cells* **2012**, *101*, 57–61.

Zweibel, K. Issues in Thin Film PV Manufacturing Cost Reduction. *Sol. Energy Mater. Sol. Cells* **1999**, *59*, 1–18.

Vita

Taylor Bryan Harvey was born in Provo, UT in 1982 and grew up in Kaysville, UT. He graduated from high school in 2000 and then attended Brigham Young University in Provo, UT, graduating with a Bachelors in chemical engineering in 2006. He then worked for 4 years in the oil and gas industry. Taylor returned to graduate school in 2010, studying nanocrystal photovoltaics under Dr. Brian Korgel at the University of Texas at Austin.

Permanent email address: tbharvey[at]gmail.com

This dissertation was typed by Taylor Bryan Harvey